VISCOUS TIME SCALE IN ACCRETING POWERED PULSARS AND ANOMALOUS X-RAY PULSARS

A THESIS SUBMITTED TO
THE GRADUATE SCHOOL OF NATURAL AND APPLIED SCIENCES
OF
MIDDLE EAST TECHNICAL UNIVERSITY

BY

BURÇİN İÇDEM

IN PARTIAL FULFILLMENT OF THE REQUIREMENTS
FOR
THE DEGREE OF MASTER OF SCIENCE
IN
PHYSICS

JUNE 2011

Approval of the thesis:

VISCOUS TIME SCALE IN ACCRETING POWERED PULSARS AND ANOMALOUS X-RAY PULSARS

submitted by **BURÇİN İÇDEM** in partial fulfillment of the requirements for the degree of **Master of Science in Physics Department, Middle East Technical University** by,

Prof. Dr. Canan Özgen
Dean, Graduate School of **Natural and Applied Sciences**

Prof. Dr. Sinan Bilikmen
Head of Department, **Physics**

Prof. Dr. Altan Baykal
Supervisor, **Physics Department, METU**

Examining Committee Members:

Prof. Dr. Mehmet Ali Alpar
Physics Dept., Sabancı University

Prof. Dr. Altan Baykal
Physics Dept., METU

Prof. Dr. Ümit Kızıloğlu
Physics Dept., METU

Prof. Dr. Halil Kırbıyık
Physics Dept., METU

Assist. Prof. Dr. S. Çağdaş İnam
Electrical and Electronics Eng. Dept., Başkent University

Date:

I hereby declare that all information in this document has been obtained and presented in accordance with academic rules and ethical conduct. I also declare that, as required by these rules and conduct, I have fully cited and referenced all material and results that are not original to this work.

Name, Last Name: BURÇİN İÇDEM

Signature :

ABSTRACT

VISCOUS TIME SCALE IN ACCRETING POWERED PULSARS AND ANOMALOUS X-RAY PULSARS

İçdem, Burçin
M.S., Department of Physics
Supervisor : Prof. Dr. Altan Baykal

June 2011, 134 pages

In this thesis we analyse X-ray data of accretion powered low mass and high mass X-ray binaries to understand the nature of their accretion mechanisms by searching for some clues of viscous time-scales of their accretion discs, if they have, in their low frequency power density spectra created from their long-term X-ray observations, or by doing pulse timing analysis with much shorter X-ray data to detect the effects of torque fluctuations caused by the accreting material on the pulsar.

The low mass and high mass X-ray binaries we analysed have breaks in their power density spectra, which are attributed to the role of viscosity in the formation of accretion discs. Although, the time-scales corresponding to these break frequencies are smaller than the predictions of the Standard theory of accretion discs, the sources give consistent results among themselves by displaying the expected correlation between their break and orbital frequencies. The correlation curve of LMXBs implies thicker appearing accretion discs than those assumed by the theory. The dichotomy of the HMXBs on this curve points out the different origins of accretion that these sources may have, and offers a way to distinguish the stellar-wind fed systems from the Roche-lobe overflow systems.

The timing and spectral analysis of Swift J1626.6-5156 reveal a correlation between the spin-up rate and the luminosity of the source implying that the pulsar is accretion-powered. This correlation together with the characteristics of the X-ray spectra enables us to estimate the magnetic field and the distance of the source.

The AXP 1E 2259+586 does not display any signs of viscous time-scale in its low frequency power density spectra, and its pulse timing analysis gives a much smaller torque noise value than that expected from accretion powered pulsars. In addition, the analysis results presented in this thesis reveal magnetar-like glitches which differ than those of radio pulsars, due to the presence of the strong magnetic field of the pulsar. These results eliminate the possibility that the AXP is an accretion-powered pulsar.

Keywords: Accretion, accretion discs, neutron stars, X-ray binaries, accretion powered pulsars

ÖZ

KÜTLE AKTARIMI YAPAN ATARCALARDA VE ANORMAL X-IŞINI ATARCALARINDA VİSKOZİTE ZAMANI

İçdem, Burçin
Yüksek Lisans, Fizik Bölümü
Tez Yöneticisi : Prof. Dr. Altan Baykal

Haziran 2011, 134 sayfa

Bu tezde, aktarım güçlü düşük ve yüksek kütleli X-ışını çift yıldız sistemlerinin kütle aktarım mekanizmalarını anlamak için yapılan X-ışını veri analizi çalışmaları, eğer kaynağın diski varsa uzun zamanlı gözlemlerden elde edilen güç yoğunluğu spektralarında viskozite zamanına ait ipuçlarını ya da çok daha kısa gözlemlerden zamanlama analizi yaparak aktarılan maddenin atarcaya uyguladığı dönme momentinin etkilerini incelemek suretiyle, sunulmaktadır.

Tezde sunulan analizlerin sonucunda düşük ve yüksek kütleli X-ışını çift yıldız sistemleri, düşük frekanslardaki güç yoğunluğu spektralarında kırılmalar göstermektedirler. Bu kırılmalar disk oluşumunda çok önemli bir payı olan viskozitenin etkilerine bağlanabilir. Ancak Standart Kütle Aktarım diski teorisine göre hesaplanan viskozite zamanları, analizler sonucunda bulunan kırılma frekanslarına karşılık gelen zamanlardan daha yüksek çıkmaktadır. Buna rağmen, kaynaklar kendi aralarında tutarlı sonuçlar vermektedir; teroride öngörülen kırılma ve orbit periyotları arasındaki linear ilişki deneysel olarak da doğrulanmaktadır. Düşük kütleli X-ışını çift yıldız sistemlerdeki bu ilişkiye ait doğru teoride varsayılandan daha kalın disklerin varlığına işaret etmektedir. Yüksek kütleli X-ışını çift yıldız sistemlerinin bu ilişki açsından iki gruba ayrılması, farklı kütle aktarım mekanizmalarına sahip olduklarının bir göstergesi olarak yorumlanabilir ve bu da yıldız rüzgarından aktarım yapan sistemlerle Roche-lobu taşkınından beslenen sistemleri ayırdedici bir yöntem olarak kullanılabilir.

Swift J1626.6-5156 isimli kaynağın zamanlama ve tayf analizleri sonucunda atarcanın dönme frekansının artış hızıyla kaynağın parlaklığı arasında bir ilişki tespit edilmiştir. Bu ilişkiden yararlanarak kaynağın aktarım güçlü bir atarca olduğu söylenebilir ve atarcanın manyetik alan büyüklüğü ile kaynağa olan uzaklık hesaplanabilir.

AXP 1E 2259+586 isimli kaynağın düşük frekanslardaki güç yoğunluğu spektrasında herhangi bir kırılma görülmemektedir. Zamanlama analizinden elde edilen dönme momenti gürültüsü de aktarım güclü bir atarca için tahmin edilenden daha düşük çıkmaktadır. Buna ek olarak tezde sunulan zamanlama analizi sonuçlarına göre, kaynak, magnetar-benzeri ”glitch”ler (dönme periyodunun cok kısa süreler içinde kısalması) göstermektedir ve bunlar radyo atarcalarındaki benzerlerinden, belli özellikleriyle ayrılmaktadır. Bunun nedeni olarak kaynağın çok güçlü manyetik alanı gösterilebilir. Tüm bu sonuçlar AXP kaynağının aktarım güclü olma olasılığını ortadan kaldırmaktadır.

Anahtar Kelimeler: Kütle aktarımı, kütle aktarım diskleri, nötron yıldızları, X-ışını çift yıldız sistemleri, aktarım güçlü atarcalar

To my Family

ACKNOWLEDGMENTS

I owe my deepest gratitude to Prof. Dr. Altan Baykal for his invaluable supervision, continuous guidance and encouragement throughout my graduate study. I also gratefully acknowledge Assist. Prof. Dr. S. Çağdaş İnam for his crucial contribution to this research. It is a pleasure to pay tribute also to Prof. Dr. Marat Gilfanov and Prof. Dr. M. Ali Alpar for the assistance they provided with their constructive comments.

I would like to thank my colleagues in METU Astrophysics group for useful discussions and moral motivation. I especially thank to Elif Beklen who gently grants me her time for coping with my plenty of questions. I am especially indebted to my parents, for the love, trust and support they provided me throughout my entire life. I thank all my friends, especially Ceyda Durmaz, Sezen Vatansever, Gülay Gülpınar, İrem Tanyeli and Berkcan Gökçe, with whom I spent spare times to relax and entertain during the stressful thesis writing period. They tolerated all my tiresome complaints and helped me to feel confident to carry on. I also appreciate the friendship and endurance of my office mates, Dilege Gülmez and Mehmet Doğan.

I acknowledge the scholarship from The Scientific and Technological Research Council of Turkey (TÜBİTAK) for students of Master of Science and support through the project 109T748.

TABLE OF CONTENTS

CHAPTERS

LIST OF TABLES

TABLES

LIST OF FIGURES

FIGURES

CHAPTER 1

INTRODUCTION

X-ray part of the electromagnetic spectrum corresponds to an energy range of 0.01-50 KeV. The ”X-ray universe” is the name given to the union of regions from which X-rays are detected. X-rays are produced when temperature of matter reaches millions of degrees. Such extreme temperatures are obtained in the vicinity of high magnetic fields, or extreme gravity, or explosive forces.

Most of the photons in the universe are produced by the collision of charged particles or sudden variations in their motion. The duty of photons is to carry away the energy released in those events at the speed of light. In fact, photons are the light, and electromagnetic radiation at the same time. Among the charged particles, electrons are the lightest and the most common; hence, they are responsible for the creation of most of the photons in the universe.

X-ray astronomy is quite a new field in the observational astrophysics. The first extra-solar X-ray detection was in 1962. The source of the X-rays were the object called Sco X-1 although it was not the real target of the team. They were searching for X-rays coming from the Moon instead. Hence, it was the chance again that triggered the X-ray astronomy. The first X-ray mission was not launched until the beginning of 1970s. *Uhuru* was followed by many others, varying with their main objectives. In 1970s, the most important satellites are *ANS, Copernicus, SAS-3, Ariel V, OSO 8* and NASA’s first High Energy Astrophysical Observatory *HEAO-1*. With these missions X-ray bursts and numerous pulsars were discovered, and the first detailed X-ray spectra was obtained. During the 1980s, the Space Shuttle Challenger accident affected the missions of NASA negatively, but the European, Japanese, and Russian

Space Agencies continued to launch successful X-ray astronomy missions. The most important launches are the European X-ray Observatory Satellite (*EXOSAT*), *Granat*, the Kvant module, *Tenma*, and *Ginga*. ”In the 1990s the ROSAT survey detected more than 100,000 X-ray objects, the ASCA mission made the first sensitive measurements of the X-ray spectra from these objects, and RXTE studied their timing properties.” (web, 2011a) In late 1990s an order of magnitude improvement in sensitivity for imaging was achieved by Chandra and XMM, ”Both individually and collectively, these satellites have provided an unprecedented view of the X-ray Universe. As the 21st century began, XMM-Newton, the Chandra X-ray Observatory, and RXTE were the work-horses of X-ray astronomy.” (web, 2011b) There are new projects that will replace their successful ancestors in the very near future.

There are several types of astrophysical objects which emit X-rays: galaxy clusters, black holes in active galactic nuclei (AGN), galactic objects such as stars, supernova remnants, and binary stars containing a white dwarf (cataclysmic variable stars and super soft X-ray sources), neutron star or black hole (X-ray binaries). There is also the X-ray background which is produced by some X-ray sources that cannot be resoled. The main physical mechanisms behind the X-ray continuum are bremsstrahlung radiation, black-body radiation, synchrotron radiation, or inverse Compton scattering of lower-energy photons by relativistic electrons, knock-on collisions of fast protons with atomic electrons, and atomic recombination, with or without additional electron transitions (Morrison, 1967).

X-ray binaries are classified as a special class of binaries which emit predominantly in X-rays. They are the most luminous galactic X-ray sources. Their luminosities are in the range $\sim 10^{36} - 10^{38}$ ergs/s. An X-ray binary consists of a compact object and a companion star orbiting about a common centre of mass. The compact object can be a white dwarf (cataclysmic variables), a neutron star or a black hole, while the companion star can be a normal star or a white dwarf. The answer to the question ”What could possibly give rise to such high X-ray luminosities in these binaries?” is basically the accretion mechanism. As the compact star accretes matter from the companion star, the gravitational potential energy of the in-falling matter is converted to kinetic energy eventually giving rise to radiation.

X-ray binaries can be divided into two main different classes, independent of the type of the compact object, according to the mass of the companion star. These are low-mass X-ray binaries (LMXB) and high-mass X-ray binaries (HMXB).

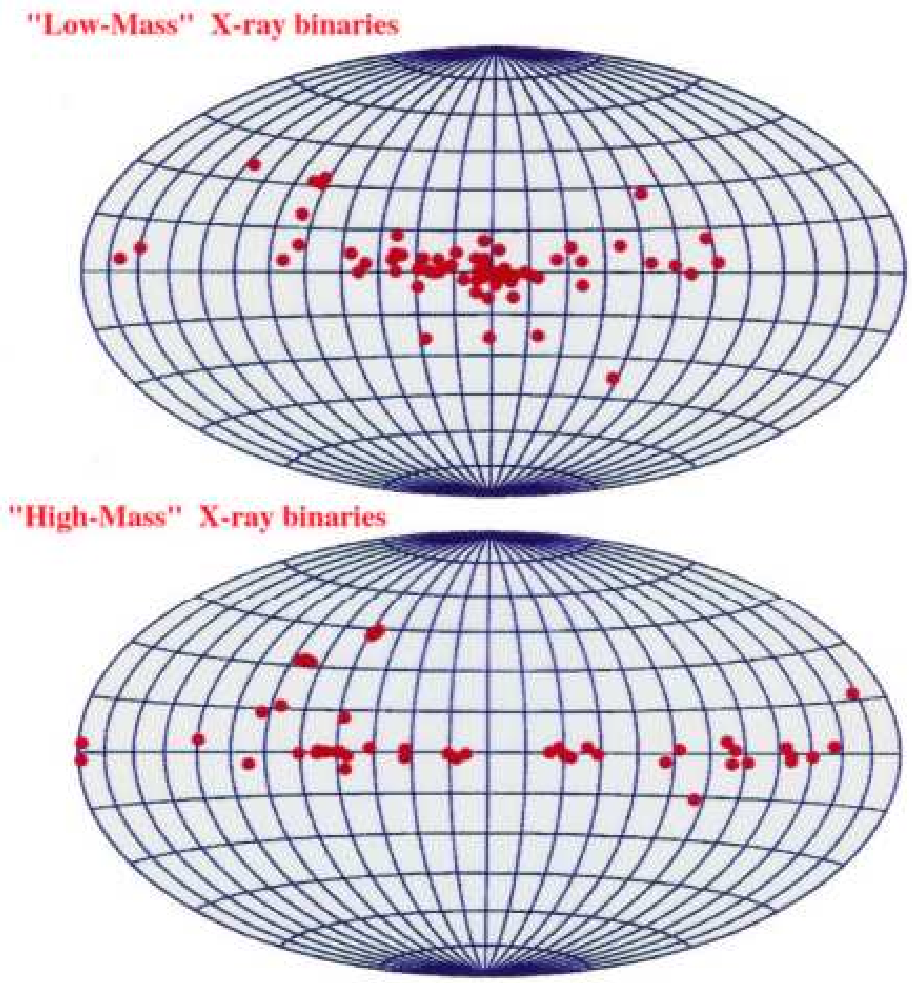

Figure 1.1: Galactic distribution of X-ray binaries

LMXBs The normal star in LMXBs is a low-mass, i.e. $M \leq 1 M_{\odot}$, star, which can only transfer matter to the compact object by Roche-lobe overflow, that can be a white dwarf, a late-type main-sequence star, an A-type star or a F-G type subgiant. F-G type companions may be the remnant of intermediate mass ($M \sim 1.5 - 4 M_{\odot}$) star which has sent most of its mass to the compact object. Hence, the optical counterparts of LMXBs are faint objects ($L_{\mathrm{opt}}/L_x < 0.1$). They have only a few characteristic emission lines in their spectra and their contribution to the optical continuum is insignificant. Continuous optical emission is generated substantially by emission from an accretion disc around the compact object, which is a result of the reprocessing of some fraction of the X-rays into optical photons. Since it is not always straightforward to determine the mass of the secondary star, LMXBs may be identified by some other properties characteristic to them:

i. type I X-ray bursts (observation of thermonuclear energy by unstable, explosive burning in bursts which is released over a very short time, of the order of seconds)

ii. a 1-10 keV soft spectrum with a characteristic temperature of 5-10 keV

iii. an orbital period which is less than about 12 h (There are LMXBs which have much longer orbital periods. This item is just to classify an unidentified object.)

The number of LMXBs discovered increases day by day with new highly sensitive detectors. Liu et al. (2007) reports a number of 187 LMXBs in their 2007 catalogue.

HMXBs High-mass X-ray binaries were detected in the 1970s for the first time, together with their optical identification. The system is composed of a compact object orbiting a massive OB class star. The compact object is either a neutron star or a black hole observed to be luminous in X-rays, main source being the accretion mechanism between the companions similar to LMXBs. HMXBs are divided into two subgroups: those with a Be star (Be/X-ray binary) and those with a supergiant star (SG/X-ray binary).

Be/X-ray systems (BeXRBs) constitute the majority of the known high-mass X-ray binaries. Compared to LMXBs, the number estimated for Galactic BeXRBs is huge, about 2000-20000 (Meurs and van den Heuvel, 1989). An important feature of these systems is their wide and highly eccentric orbits; hence, the compact object does not spend much time near the dense circumstellar disc surrounding the Be companion (Coe, 2000; Negueruela, 2007). It is also interesting that no black hole and Be star system has been found yet (Zhang et al., 2004). BeXRBs are referred as transient X-ray sources due to the emission of X-rays only when the neutron star passes through the low-velocity and high-density wind around the Be star.

SG/X-ray binaries have their compact objects orbiting their companions deep inside the highly supersonic wind of supergiant early-type star. These systems have not been understood as well as LMXBs: their source of X-rays may be originating from either strong stellar wind of the supergiant or Roche-lobe overflow accretion. A property to distinguish these two ways is the amount of X-ray luminosity they produce: 10^{35} – 10^{36} ergs.s^{-1} by stellar wind accretion and $\sim 10^{38}$ ergs.s^{-1} by Roche-lobe overflow.

There are also HMXBs detected in Magellanic Clouds. Recent catalogues of Liu et al. report 128 HMXBs in Magellanic Clouds (Liu et al., 2005) and 114 HMXBs in our galaxy (Liu et al., 2006).

Two other classes of objects which are luminous in X-rays are soft gamma repeaters (SGRs) and anomalous X-ray pulsars (AXPs). They are exotic sources exhibiting mysterious behaviours. There are only 9 SGRs (7 confirmed, 2 candidates), and 12 AXPs (9 confirmed, 3 candidates) detected so far; nevertheless, this is sufficient for them to draw great attention. Even though they are widely considered to be magnetars (isolated pulsars with very large magnetic fields, $B \geq 10^{14}$ G), several theories have been proposed to account for their birth and unusual behaviours, each of which have their supporting observational confirmations. In this thesis, we will be dealing with only one AXP; hence, it is better that we focus on general properties of AXPs.

AXPs Anomalous X-ray pulsars were discovered in the early 1980s with the detection of the object 1E 2259+586 (Fahlman and Gregory, 1981). Their X-ray luminosities are in the range of 10^{33} – 10^{36} erg.s^{-1}, which is comparable to the HMXBs. The clustering of their periods in the narrow range of 2 – 12 s is one of their characteristics. Spin rate of all of the AXPs are observed to decrease in time with relatively large rates, 10^{-10} – 10^{-12} s.s^{-1}. In spite of these high magnitudes, the observed X-ray luminosities cannot be produced solely by the rotational energy loss. Among the some suggestions for the main energy source, strong magnetic field of the pulsar (Duncan and Thompson, 1992) receives wide acceptance. AXPs have not displayed any evidence of binary companions yet. They show very small or no long term variability. Their X-ray spectrum is generally soft, but also hard X-ray emission was detected from some AXPs (den Hartog et al., 2004; Revnivtsev et al., 2004; Kuiper et al., 2004). AXPs can emit short bursts (Kaspi et al., 2000, 2003; Woods et al., 2004) similar to those of the SGRs which verifies the resemblance between these two classes of objects. There is one other theory trying to explain the mysteries of AXPs (also SGRs), which is based on accretion. This is known as the fallback disc model and proposes that the pulsar accretes matter from the debris of a supernova remnant and this time dependent accretion is the source of the power of AXPs (This theory is discussed in Section 2.5 in detail).

X-ray binaries show X-ray flux variations in a broad range of time-scales. The power density spectrum of a system often reveals a number of periodic and quasi-periodic phenomena that can be related to orbital motion of the binary system, rotation of the central star and some quasi-periodic phenomena. In addition, aperiodic variability is observed, giving rise to the broad band continuum component in the power density spectrum, extending from $\sim 10 - 100$ msec to the longest timescales accessible for monitoring instruments (Gilfanov and Arefiev, 2005). Due to the fact that the conditions for creation of X-ray radiation are only provided in the vicinity of the central object, the variations in the X-ray flux give us some idea about the events, such as the alterations in the mass accretion rate, going on there. When the periodic features in the X-ray spectra are taken into account, it is seen that low frequency X-ray variations also appear besides high frequency variations. For instance, X-ray pulsations are usually periodic with spin period and they are due to magnetically funnelled accretion onto the poles, flickering and quasi-periodic oscillations are caused by instabilities in the disc, transient accretion events may be sign of alternation between phases of high and low accretion rates due to thermal transitions in the accretion disc.

Accretion is basically the transfer of matter from one of the components to the other in a binary system. (There are also cases in which a heavenly body accretes matter from the interstellar space but that is a quite different mechanism.) It is that accretion which is responsible for the formation of a disc, which is continuously being nourished, around the accreting object. The question is why matter is not transferred directly to the object. The driving process for accretion is that the accreting matter needs to lose most of its angular momentum in order to combine with the central object, and this loss is substantially associated with viscosity. The loss or rather the transport of the excessive angular momentum is accompanied with emission of energy. Hence, if the properties of these emission is analysed by observations, we can get information about the accretion dynamics.

In this thesis, we analyse X-ray data of a sample of sources including high-mass X-ray binary systems, low-mass X-ray binary systems and an anomalous X-ray pulsar in order to understand accretion mechanism in these systems. We use the power spectral density and pulse timing analysis methods to analyse the anomalous X-ray pulsar in addition to its power density spectrum. observations of *RXTE*. Chapter 2 is a theoretical review of accretion in general and Chapter 3 is a review of physics of accretion discs. In Chapter 4, the X-ray sources selected for the analysis are introduced and their general properties are given. In Chapter 5 the analysis done for the viscous time-scale of X-ray binaries are described and their results are discussed. Chapter 6 contains the timing and X-ray spectral analysis of Swift J1626.6-5156. Chapter 7 is about the timing analysis of the AXP source 1E 2259+586. Finally, Chapter 8 is the conclusion of all of the results given in the previous chapters.

The results of high mass X-ray sources (except the work about Swift J1626.6-5156) were published before in the Astronomy & Astrophysics journal (Içdem and Baykal, 2011). The timing and spectral analysis of the source Swift J1626.6-5156 was accepted to be published in the the Monthly Notices of the Royal Astronomical Society (reference for the arXiv e-print: Icdem et al. (2011b)). The pulse timing analysis of the AXP 1E 2259+586 was also submitted to the Monthly Notices of the Royal Astronomical Society (reference for the arXiv e-print: Icdem et al. (2011a)).

CHAPTER 2

ACCRETION

An accretion disc is a structure formed by diffuse material in orbiting around a central object. The central object can be a young star, a protostar, a white dwarf, a neutron star, or a black hole. Gravitational attraction of the central causes the material in the disc to spiral inward towards the central object.

The two main reasons for many binary systems to transfer matter at some stage in their evolutionary lifetimes:

1. Roche lobe overflow: Roche lobe is the name for the inner gravitational equipotential surface surrounding both of the stars. If one of the stars in the system fills its Roche lobe, by means of increasing of its radius or shrinking of the binary orbit, mass transfer starts at the point where the gravitational pull of the companion dominates.
2. Stellar wind accretion: Some of the matter ejected out as wind by one of the stars may be captured by the other.

The first of these processes is better understood and more efficient than the latter. In addition, the Roche lobe overflow generates a more stable accretion process as the stellar winds turn into accretion discs mostly if their origin is a huge violent star, namely an O or B type star. That means the stellar wind accretion is directly affected from the chaos taking place in the donating star, so subsequently creates instabilities in the disc. These instabilities occur quite frequently making it hard for researchers to produce verifiable arguments. Most of the low mass X-ray binaries are on the safe side as they experience the Roche lobe overflow; however analysis results of high mass X-ray binary systems are hard to interpret.

2.1 Disc Formation by Roche Lobe Overflow

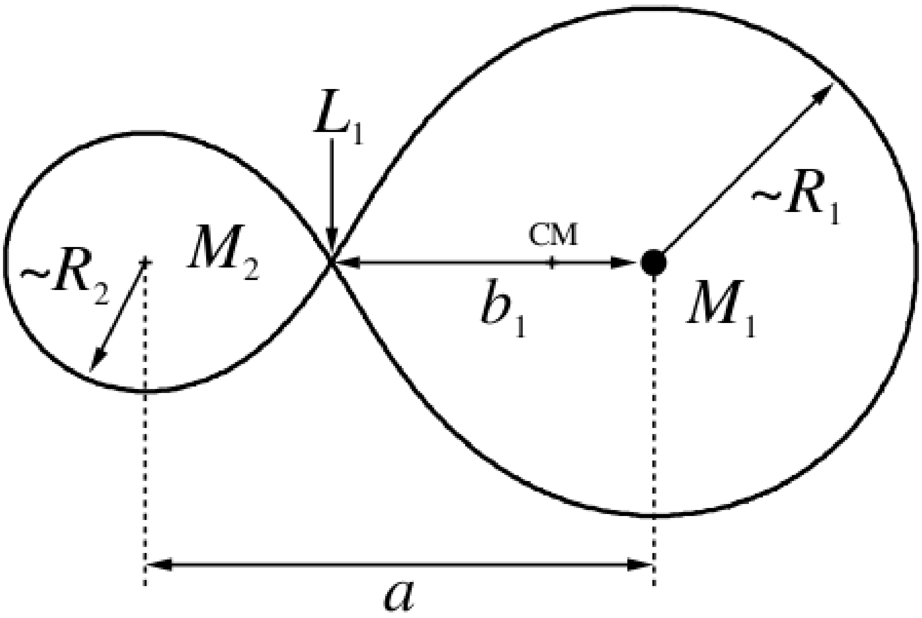

Figure 2.1: Roche-lobe geometry: ”R_1 and R_2 are defined the radii of spheres having a volume equal to the volume of the corresponding Roche lobe.” (Frank et al., 2002)

As mentioned above, the transferring material cannot directly accrete on to the compact star because of its high angular momentum due to its motion in the binary orbit. Considering the Roche lobe overflow case, the matter has to pass through the Lagrange point L_1 (the points of zero net gravitational force belonging to the system) as shown in Figure 2.1. After leaving L_1, it will tend to follow the least energy orbit corresponding to its angular momentum, which is the Kepler orbit at a radius R_{circ}, where it will have a circular velocity

$$v_\phi(R_{\mathrm{circ}}) = \left(\frac{GM_1}{R_{\mathrm{circ}}}\right)^{1/2} \tag{2.1}$$

where

$$R_{\mathrm{circ}} v_\phi(R_{\mathrm{circ}}) = b_1^2 \omega \tag{2.2}$$

Using $\omega = 2\pi/P$ and Kepler's third law $4\pi^2 a^3 = GMP^2$, we find

$$\frac{R_{\rm circ}}{a} = (1+q)\left(\frac{b_1}{a}\right)^4 \tag{2.3}$$

where $q = M_2/M_1$ is the mass ratio of the binary system. The radius $R_{\rm circ}$ is usually called the circularization radius. The distance b_1 of the L_1 point from the centre of the primary (mass M_1) is given to good accuracy by a fitted formula of (Plavec and Kratochvil, 1964):

$$\frac{b_1}{a} = 0.500 - 0.227 \log q \tag{2.4}$$

Using (4) and typical parameters, $R_{\rm circ}$ can be found to be

$$\begin{aligned} R_{\rm circ} &\approx 1.2 P_{\rm day}^{2/3} R_0 \qquad \text{for} \quad q = 0.3 \\ R_{\rm circ} &\approx 0.6 P_{\rm day}^{2/3} R_0 \qquad \text{for} \quad q \geq 0.5. \end{aligned} \tag{2.5}$$

$R_{\rm circ}$ is the minimum radius that a disc can form. The disc is initially a ring at $R_{\rm circ}$, and then due to dissipative processes, which are inevitable because of the interactions of particles in the ring, some of the disc energy is radiated. Consequently, less energetic particles cannot stay at $R_{\rm circ}$ and they propagate deeper through the central object. The tendency to have the least energy for a certain angular momentum pushes the matter into concentric circular orbits, which will eventually form the accretion disc. However, they still have the angular momentum of their initial orbit and they need to lose the excessive amount in order to hold on to their current orbit. Therefore, the angular momentum is transported outwards which causes the matter in the outer parts of the disc to spiral outwards. That is, the initial ring of matter expands both inwards and outwards to establish the disc we observe. Hence, the actual size of an accretion disc is larger than the circularization radius. The inner radius may be as small as the radius of the compact object if the magnetic effects allow. The outer radius, on the other hand, cannot be larger than the Roche lobe of the compact object. In fact, there are some other effects arising from the binary system dynamics, such as tidal effects (see Section 3.6), to limit the size of the disc.

The amount of the energy lost to radiation by the particles in the disc can be estimated as follows: The binding energy of a gas element of mass ΔM in the Kepler orbit just near the surface of the accreting object is $\frac{1}{2} G M_1 \Delta M / R_*$. Assuming its initial binding energy to be negligible, the total disc luminosity in a steady state is found to be

$$L_{\rm disc} = \frac{GM_1\dot{M}}{2R_*} = \frac{1}{2}L_{\rm acc} \tag{2.6}$$

where $\dot{M}$ is the accretion rate and $L_{\rm acc}$ is the accretion luminosity, i.e. the rate of energy release by conversion of the excess potential energy into heat. The other half of the available energy is radiated at a location very close to the compact object (see Section 2.4).

2.2 Viscous Torques

Viscosity is the quantity that describes a fluid's resistance to flow. Fluids show resistance to the objects that try to move with relative velocities through them as well as to the motion of layers with differing velocities within them. Viscosity (represented by the symbol η "eta") is the ratio of the shearing stress (F/A) to the velocity gradient ($\Delta v_x/\Delta z$ or dv_x/dz) in a fluid. We usually deal with the ratio of the viscous force to the inertial force, the latter characterized by the fluid density ρ. This ratio is represented by the kinematic viscosity (Greek letter nu, ν), defined as $\nu = \eta/\rho$ where η is the dynamic viscosity (Pa.s), ρ is the density (kg/m^3), and ν is the kinematic viscosity (m^2/s).

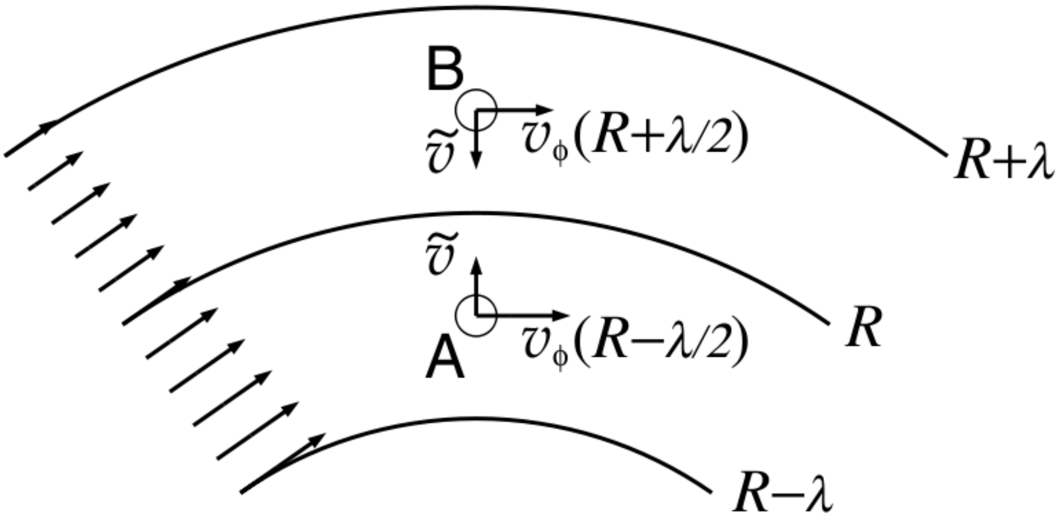

Figure 2.2: Exchange of fluid bubbles between two rings with different angular velocities. Figure is taken from Frank et al. (2002)

The concentric rings in an accretion disc have different velocities determined by their radii; hence they constitute a differential rotation. The thermal or turbulent motions of fluid particles transport angular momentum in the radial direction and this creates viscous stress which is called shear viscosity in this case. Fig. 2.2 shows the basic picture. Two blobs in neighboring rings with similar radial speeds but with different rotational velocities. They do not come across if the distance between them is larger than the mean free path of the particles, λ. Hence, the width of the rings should be considered not to be bigger than λ. Assuming the conservation of streamwise momentum, the net angular momentum transfer can be estimated. It is apparent that mass crosses the surface R =const at equal rates in both directions. As a result, the torque generated between the rings is

$$-\rho\tilde{v}H\lambda R^2\frac{d\Omega}{dr}, \tag{2.7}$$

where Ω is the angular velocity, and the force per unit area on the interface between the rings is the stress component

$$\sigma_{r\phi} \equiv -\eta R\frac{d\Omega}{dr} \sim -\rho\tilde{v}\lambda R\frac{d\Omega}{dr}. \tag{2.8}$$

The kinematic viscosity due to either hydrodynamic turbulence or molecular transport in a simple shearing motion is $\nu \sim \lambda\tilde{v}$. In the case of molecular transport, λ and $\tilde{v}$ are the mean free path and thermal speed of the molecules, respectively. The magnitude of the torque between the rings is found by integrating (2.8) over the interface and multiplying by R

$$G(R) = 2\pi R\nu\rho HR^2\frac{d\Omega}{dr}, \tag{2.9}$$

where H is the vertical scale-height of the disc. The sign of $d\Omega/dr$ determines the direction of the angular momentum transfer: for radially decreasing angular velocity, inner rings lose angular momentum to outer ones, as expected. The viscous dissipation rate, which turns into heat, per unit plane is found to be

$$D(R) = \frac{Gd\Omega/dr}{4\pi R} = \frac{1}{2}\nu\Sigma(R\frac{d\Omega}{dr})^2 \tag{2.10}$$

where $\rho H = \Sigma$ and Ω is considered to have a Keplerian form: $\Omega = \Omega_K = \left(\frac{GM}{R^3}\right)^{1/2}$ at radius R. Using this in (2.10) gives

$$D(R) = \frac{9}{8}\nu\Sigma\frac{GM}{R^3} \tag{2.11}$$

Even though viscosity is thought to be the main reason for the angular momentum transfer and dissipation, the Reynolds number says the opposite:

$$Re = \frac{inertia}{viscous} \sim \frac{v_\phi^2/R}{\lambda v_{\rm th} v_\phi / R^2} = \frac{R v_\phi}{\lambda v_{\rm th}} \tag{2.12}$$

With typical constants, the Reynolds number for the standard 'molecular' viscosity is calculated to be $> 10^{14}$, which indicates that viscosity at the molecular scale is inefficient. However, large scale turbulences generated beyond the critical Reynolds number may be much more effective. Although the chaotic mechanism of turbulence makes it difficult to be formulated, the turbulent viscosity can still be expressed as $\nu_{\rm turb} \sim \lambda_{\rm turb} v_{\rm turb}$ and some upper limits can be placed for the length-scale, $\lambda_{\rm turb}$ and turnover velocity, $v_{\rm turb}$ such as $\lambda_{\rm turb} \leq H$ and $v_{\rm turb} \leq c_s$. Shakura and Sunyaev (1973) introduced the famous α-prescription, which leads to the 'standard disc model'. According to this theory, instead of using molecular viscosity kinematic viscosity is formulated by

$$\nu = \alpha c_s H \tag{2.13}$$

where $\alpha \leq 1$ (α may vary through the disc).

Apart from the requirement that the angular momentum should be transformed outwards while mass is creeping inwards, there should be a source of energy fed back to the disc so that accretion can be maintained for long time. Two suggestions for a mechanism to provide this are pure hydrodynamic instabilities and thermally driven convection. Balbus et al. (1996) showed that in Keplerian accretion discs, local hydrodynamic turbulence is ineffective to load the required energy back into the disc, so the Reynolds stress keeps decreasing and transport process is halted at a point. Similarly, there are some problems regarding the angular momentum transport by convection. Even if the negative viscosity problem (i.e. momentum transport occurs inwards) put forward by Ryu and Goodman (1992) can be solved by using the Boltzmann equation and considering the convective eddies to behave similarly to particles or blobs (Kumar et al., 1995), the contribution of convection to the whole accretion mechanism is still ambiguous.

There is one more model that can account for the magnitude and the sign issues of the accretion correctly: Magnetohydrodynamic (MHD) turbulence (Chandrasekhar, 1960, 1961; Balbus and Hawley, 1991). There are several ways in which MHD turbulence develops. A small radial perturbation in the accretion disc may initiate a rival between magnetic tension, and the imbalance between gravity and rotation, which results in pure MHD turbulence. In fact, creation of MHD turbulence due to the presence of a small vertical magnetic field or MHD fluctuations differ from the pure MHD turbulence in that they allow fluid-field coupling (key point to feed energy back into the turbulent movements) and so they are more promising to explain the consistency of the observed angular momentum transfer.

2.3 Stellar Wind Accretion

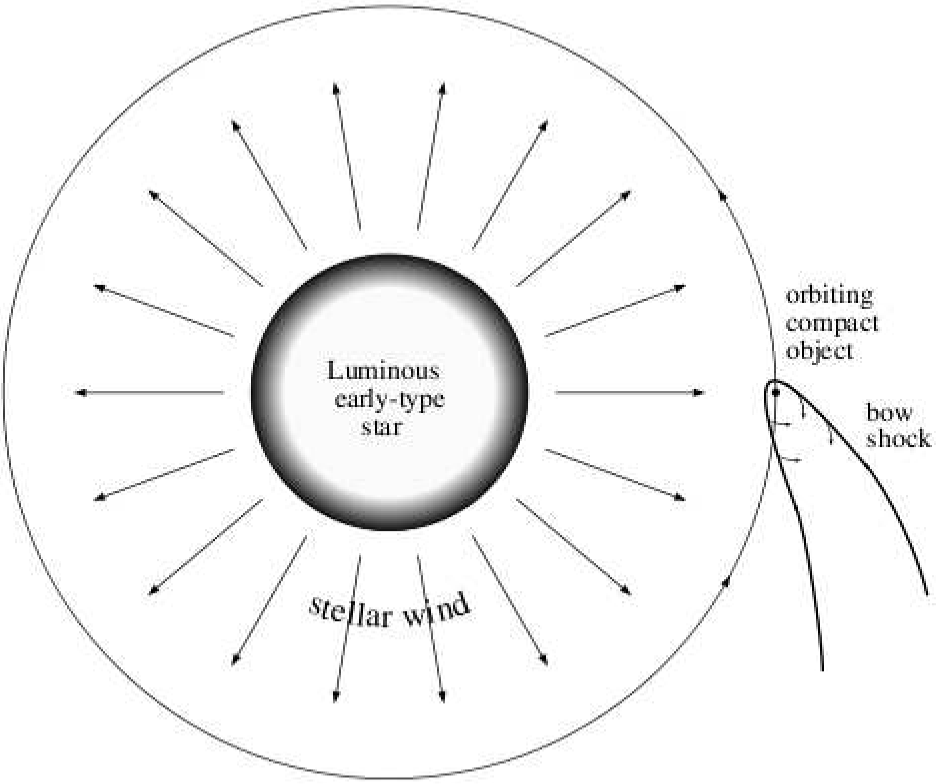

Figure 2.3: Stellar wind accretion from an early-type main sequence star, figure from Frank et al. (2002)

Stellar wind accretion is effective when an early-type (O or B type) star and a compact object (neutron star or black hole) constitute a close binary. Early type stars eject significant amount of particles by means of their stellar winds. The velocities of these particles are not less than the escape velocity of the star

$$v_w(r) \sim v_{\rm esc}(R_E) = \left(\frac{2GM_E}{R_E}\right)^{1/2} \tag{2.14}$$

Here R_E and M_E are the radius and the mass of the star,respectively, and $v_{\rm esc}$ is the escape velocity at the surface. The compact object comes across these fast particles throughout its motion in the binary. The relative velocity of the particles is $v_{\rm rel} \simeq (v_n^2 + v_w^2)^{1/2}$, where v_n is the velocity of the neutron star in the binary orbit. If the velocity of a particle is insufficient to resist to the gravitational attraction of the compact object, the particle is captured by the compact star. The region of accretion is a cylinder whose axis is along the direction of the relative wind velocity and the radius of that region is approximated to be

$$r_{\rm acc} \sim 2GM_n/v_{\rm rel}^2 \tag{2.15}$$

Although this is not a very good approximation, it gives us an idea about the efficiency of wind accretion. The fraction of the stellar wind accreted onto the neutron star is

$$\begin{aligned} \frac{\dot{M}}{-\dot{M}_w} &\simeq \frac{\pi r_{\rm acc}^2 v_w(a)}{4\pi a^2 v_w(a)} = \frac{G^2 M_n^2}{a^2 v_w^4(a)} \\ &\simeq \frac{1}{4}\left(\frac{M_n}{M_E}\right)^2 \left(\frac{R_E}{a}\right)^2 . \end{aligned} \tag{2.16}$$

where a is the binary separation. Since the mass of the early type star is far greater than the mass of the neutron star and the binary separation is naturally larger than the radius of the star, one can easily say that only a small amount of the stellar wind is accreted by the compact object. Nonetheless, this type of accretion is detectable due to the type of emission it makes: $L_{\rm acc}$ is in X-rays to a great extend besides the visible light of the bright early-type star. The main scope of our work is the accretion discs and the question is 'Under what conditions can the stellar wind accretion form a disc around the compact object?'. Similar to the Roche-lobe overflow case, we define a 'circularization radius, $R_{\rm circ}$' by the help of the specific angular momentum of the captured material

$$\frac{1}{4} r_{\rm acc}^2 \omega \sim l = (GM_n R_{\rm circ})^{1/2} \tag{2.17}$$

Using 2.15, we can find an approximate circularization radius for a disc

$$R_{\rm circ} \simeq \frac{G^3 M_n^3 \omega^2}{v_w^8}. \tag{2.18}$$

If the wind velocity is represented by a wind law: $v_w^2 = \lambda(r) v_{\rm esc}^2(R_E)$ with $\lambda(r) \sim 1$, and with the use of Kepler's law

$$\frac{R_{\rm circ}}{a} = \frac{M_n^3(M_n + M_E)}{16\lambda^4(a)M_E^4}\left(\frac{R_E}{a}\right)^4 \tag{2.19}$$

The most significant factor in this equation is the wind law, $\lambda(r)$, since the ratio, $R_{\rm circ}/a$, is determined by the fourth power of the reciprocal of λ which depends on the physical properties of the binary system. Thus, if a disc is to form in a stellar wind accretion, there is no certain estimate for the size of it although it is expected to be larger than $R_{\rm circ}$ owing to the angular momentum transfer (See Section 2.1).

2.4 Boundary Layer

Boundary layer is the region where the accreted matter loses its excessive angular momentum before falling into the compact object because the Keplerian angular velocity is greater than the surface angular velocity of the compact object, $\Omega_* < \Omega_K(R_*)$. The boundary layer extends to a radius $R_* + b$ from the surface. Generally, b is assumed to be much smaller than R_*, and using this argument the luminosity radiated from the boundary layer can be estimated. This is not just the energy difference between a Kepler orbit at R_* and a particle with angular velocity Ω_* at the same radius, the torque that spins up the star by acting on the surface should also be taken into account. The starting point is the conservation of angular momentum while matter is flowing through an annulus lying between R and $R + \Delta R$, which has total mass $2\pi R\Delta R\Sigma$ and total angular momentum $2\pi R\Delta R\Sigma R^2\Omega$. Then, the rate of change of these quantities

$$\begin{aligned} \frac{\partial}{\partial t}(2\pi R\Delta R\Sigma) &= v_R(R.t)2\pi R\Sigma(R.t) - v_R(R + \Delta R, t) \\ &\quad \times 2\pi(R + \Delta R)\Sigma(R + \Delta R, t) \\ &\cong -2\pi\Delta R\frac{\partial}{\partial R}(R\Sigma v_R) \end{aligned} \tag{2.20}$$

$$\begin{aligned}\frac{\partial}{\partial t}(2\pi R\Delta R\Sigma R^2\Omega) &= v_R(R.t)2\pi R\Sigma(R.t)R^2\Omega(R)\\ &\quad -v_R(R+\Delta R,t)2\pi(R+\Delta R)\Sigma(R+\Delta R,t)\\ &\quad \times(R+\Delta R)^2\Omega(R+\Delta R)+\frac{\partial G}{\partial R}\Delta R\\ &\cong -2\pi\Delta R\frac{\partial}{\partial R}(R\Sigma v_R R^2\Omega)+\frac{\partial G}{\partial R}\Delta R \qquad (2.21)\end{aligned}$$

In the limit $\Delta R \rightarrow 0$, these two equations turn into

$$R\frac{\partial\Sigma}{t\partial t}+\frac{\partial}{\partial R}(R\Sigma v_R)=0 \qquad (2.22)$$

$$R\frac{\partial}{\partial t}(\Sigma R^2\Omega)+\frac{\partial}{\partial R}(R\Sigma v_R R^2\Omega)=\frac{1}{2\pi}\frac{\partial G}{\partial R}. \qquad (2.23)$$

Assuming $\partial/\partial t = 0$ and using (2.9) we get

$$-\nu\Sigma\Omega' = \Sigma(-v_R)\Omega + C/(2\pi R^3), \qquad (2.24)$$

where C is a constant of the integral. For boundary layer problem C can be found using the outer limit of the boundary layer $R = R_* + b$ where $\Omega' = 0$

$$C = \left[-2\pi R^3\Sigma(-v_R)\Omega\right]_{R=R_*+b} \simeq -\dot{M}R_*^2\Omega_K(R_*) \qquad (2.25)$$

where we have assumed $b \ll R_*$ and $\Omega(R_* + b) \simeq \Omega_K(R_*)$. Now, it is apparent from (2.24) and (2.9) that the viscous torque is

$$G = -\dot{M}R^2\Omega + \dot{M}R_*^2\Omega_K. \qquad (2.26)$$

Hence, the luminosity to be radiated by the boundary layer is

$$\begin{aligned}L_{\mathrm{BL}} &= \frac{1}{2}\dot{M}R_*^2(\Omega_K^2-\Omega_*^2)-G_*\Omega_*\\ &= \frac{1}{2}\dot{M}R_*^2\left[\Omega_K^2-\Omega_*^2+2\Omega_*^2-2\Omega_*\Omega_K\right]\\ &= \frac{GM\dot{M}}{2R_*}\left[1-\frac{\Omega_*}{\Omega_K}\right]^2. \qquad (2.27)\end{aligned}$$

The boundary layer pictured above is only valid if the disc extends right down to the surface of the accreting star. However, the presence of magnetic field make this picture irrelevant by disrupting the disc flow (see Fig. 2.4). In such a case, magnetic pressure begins to dominate as the matter comes close to the stellar surface and disrupts the spherically symmetric infall at a radius r_M where the magnetic pressure first exceeds the ram and gas pressures of the matter. Near the star, the velocity of the matter reach supersonic values and at these values ram pressure, ρv^2, is far greater than the gas pressure. The magnetic pressure can be calculated from the following expression

$$P_{\text{mag}} = \left[\frac{4\pi}{\mu_0}\right]\frac{B^2}{8\pi} = \left[\frac{4\pi}{\mu_0}\right]\frac{\mu^2}{8\pi r^6} \tag{2.28}$$

where $\mu = B_* R_*^3$ is the magnetic moment of the compact object. r_M can be determined from the equality $P_{\text{mag}}(r_M) = \rho v^2|_{r_M}$

$$r_M = 5.1 \times 10^8 \dot{M}_{16}^{-2/7} m_1^{-1/7} \mu_{30}^{4/7} \text{ cm} \tag{2.29}$$

where μ_{30} is μ in units of 10^{30} G.cm^3 and $m_1 = M_n/M_\odot$. This can be also expressed in terms of the luminosity of the source, $L_{\text{acc}} = GM\dot{M}/R_*$. If the parametrization is made appropriate for a neutron star

$$r_M = 2.9 \times 10^8 m_1^{1/7} R_6^{-2/7} L_{37}^{-2/7} \mu_{30}^{4/7} \text{ cm} \tag{2.30}$$

where $L_{37} = L_{\text{acc}}/10^{33}$ erg.s^{-1}. This quantity, r_M is known as the Alfvén radius and within this radius the accreted material follows the magnetic field lines.

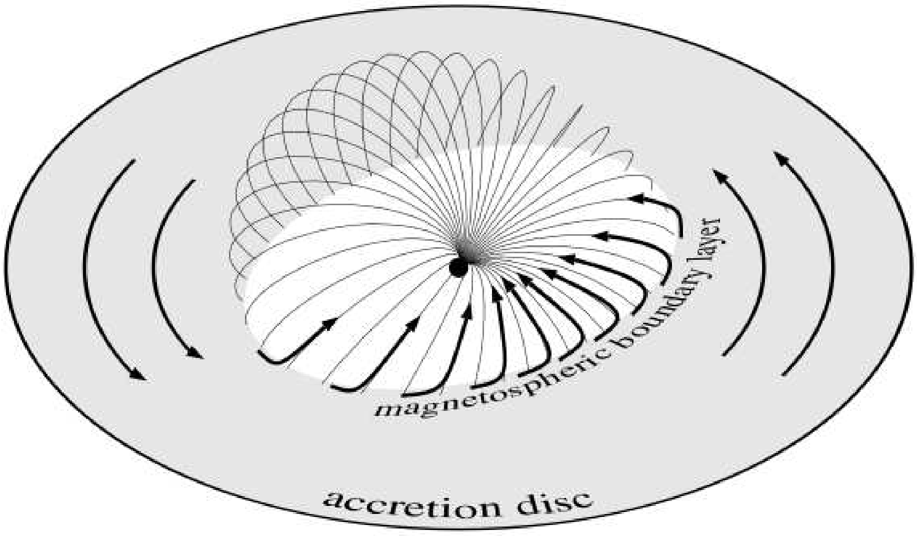

Figure 2.4: Accretion disc in the presence of magnetic field. The magnetic dipole lines roughly determine the boundary of the magnetosphere. Figure is extracted from Frank et al. (2002)

The expression of the Alfvén radius was determined using the equivalence of the magnetic and ram pressures. However, the actual factors are the magnetic and viscous

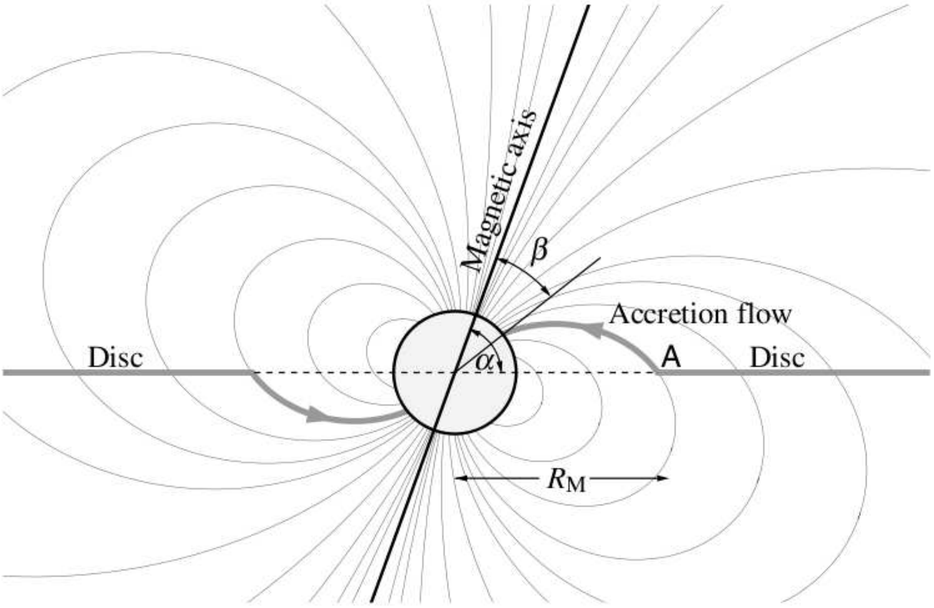

Figure 2.5: Schematic view of accretion of matter from a disc to the polecaps, figure from Frank et al. (2002)

torques, although the previous approach yields a good prediction. For a more accurate estimation, 'the condition for magnetic disruption at cylindrical radius $R = R_M$ is that the torque exerted by the magnetic field on the disc at R_M should be of the order of the viscous torque $G(R_M)$' (Frank et al., 2002). The main difficulty here is about predicting the magnetic torque quantitatively since the magnetic field configuration may be quite distorted from dipole-like structure. Nevertheless, R_M is generally found to be of the order of the spherical Alfvén radius r_M. In addition, steadiness of the accretion is affected from the inclination of the magnetic axis with respect to the disc plane because the the magnetic field lines also rotate with the compact object. Unless $\Omega_* < \Omega_K(R_M)$ is satisfied, the particles attached to the field lines at $R = R_M$ are repelled by the 'centrifugal barrier' at R_M and spiral outwards to larger R. A new parameter is introduced at this step called fastness parameter:

$$\omega_* = \Omega_*/\Omega_K(R_M) \tag{2.31}$$

and the requirement about the angular velocities reduces to $\omega_* < 1$.

Mentioning the magnetic effects raises the question whether the disc formation can be interrupted by the magnetic torques. Calculations show that R_M is always less than the circularization radius R_{circ} for Roche lobe accretion. Hence, the answer to the question is ”No!” in the case of Roche-lobe overflow accretion (since the circularization radius is a lower limit to the disc size). On the other hand, the stellar wind accretion case is more complicated due to the complexity of the accretion mechanism.

2.5 Fallback Disc Model

Anomalous X-ray pulsars are mysterious objects that show many unusual properties such as their soft X-ray spectra, their low luminosities, their steadily increasing periods, etc. They do not have detectable binary companions and some of their dynamical features resemble those of radio pulsars. In addition, their energy source that power their X-ray emission is still an important question. There are some theories proposed to solve this problem: rotation power, magnetar model or accretion power. Rotation power is eliminated by a very basic calculation. From timing measurements and using the characteristic values of AXPs, the rate of loss of rotational energy is $|\dot{E}| = 4\pi^2 I\dot{P}/P^3 \cong 10^{32.5}$ erg.s^{-1} which is order of magnitudes smaller than their X-ray luminosities (Chatterjee et al., 2000). The other two models, on the other hand, have both their observational supporters and they are in a fierce competition. Magnetar model suggests an internal energy source for AXPs which are modelled as isolated, ultramagnetized neutron stars (Duncan and Thompson, 1992). In this case either magnetic field decay (Thompson and Duncan, 1996) or residual thermal energy (Heyl and Hernquist, 1997) is the source of the emission. The magnetar model is a powerful model with all the dynamical irregularities it predicts and their observational counterparts. However, we will mainly focus on the accretion powered X-ray emission since our main scope is accretion discs.

There have been several different mechanisms put forward for the accretion powered X-ray emission model. First of these was by (Mereghetti and Stella, 1995) predicting the source of the accretion to be a low mass binary companion. The approach of Wang (1997) considered the neutron star of an AXP as an old object accreting from the interstellar medium. In another model, AXPs were proposed as relatives of HMXBs, which were accreting from the debris of a disrupted binary companion (van Paradijs et al., 1995; Ghosh et al., 1997). One other model was suggested by Chatterjee et al.

(2000) (CHN00 from now on). In their model, the source of power is the accretion from a fossil disc which occurs from matter falling back onto the neutron star just after its birth. Among all the accretion powered X-ray emission models, the last one is widely accepted since it has been confirmed by many observations.

The starting points of CHN00 were that there had not been any companions detected near the AXPs, and the steady spin-down of the AXPs indicated that there cannot have been an equilibrium between the pulsar and the disc. They improved the idea of Ghosh et al. (1997) which suggests time-dependent accretion by explaining ”whether a young, rapidly spinning neutron star can be spun down to periods $P \sim 10$ s on time-scales consistent with, e.g., age estimates based on associations with supernova remnants” (Chatterjee et al., 2000). According to the model of CHN00, there can be some inefficiency in the supernova explosion that will give birth to a neutron star such that a small amount of the ejected matter falls back instead of spreading into the interstellar medium. This material is naturally accreted by the neutron star (of course the accretion will be controlled by the Eddington limit, i.e. when this limit is exceeded the accretion process will turn into ejection). Formation of a disc around the neutron star depends on the angular momentum of the material as expected. If the total mass of the fall-back material is M_{fb} and mass of the material to form the disc is M_d, CHN00's model verifies the formation of a disc even when $M_d \ll M_{\mathrm{fb}}$. The circularization of material around the neutron star happens in the local dynamical time-scale, in a similar manner to the tidal disruption of stars by massive black holes (Cannizzo et al., 1990), and then this ring of matter forms the disc under the effect of viscous torques as explained earlier.

The physical properties of the fallback disc depends on many factors. As discussed in Section 2.4 the inner radius of the disc is limited by the Alfvén radius. The estimation of r_A is complicated in fallback disc case: the rate of accretion of matter cannot be known certainly as some of the material may be driven from the system before reaching the surface of the neutron star (Chatterjee et al., 2000). Nevertheless, some assumptions carry us to the correct order of magnitude for r_A.

A more crucial problem is the effect of the disc on the spin of the neutron star. The model attributes this to the location of three characteristic radii with respect to each other: magnetospheric radius $R_m \sim r_A$, light cylinder radius $R_{\rm lc} = c/\Omega_*$, and the corotation radius R_c defined by $\Omega_* = \Omega_K(R_c)$. If $R_m > R_{\rm lc}$, the disc will evolve independently without contributing to the emission and influencing the neutron star. In this case, the neutron star behaves as a normal radio pulsar. However, this case evolves into some other cases where the neutron star shows the characteristics of an accreting X-ray source. As pulsar spins down due to breaking of the magnetic field, R_c increases. The decreasing accretion rate causes R_m to decrease also; hence, these two radii approach each other. The fact that $R_m \gg R_c$ does not change much implies that there is a large difference between the spin and Keplerian frequencies, spin frequency being the larger, and this eventually causes transfer of angular momentum to the disc pushing some matter out to space. In other words, the spin down of the pulsar continues even though the accretion and X-ray emission is not efficient. This phase is known as the *propeller phase* (Illarionov and Sunyaev, 1975). The final phase is somewhat a quasi-equilibrium state which begins when Ω_* becomes closer to $\Omega_K(R_m)$ (a real equilibrium can never be obtained due to the steady decrease of the mass accretion rate which is the result of limited amount of matter to be accreted). In this ’tracking’ phase, accretion is more efficient and the source will exhibit high X-ray luminosity.

This model is successful explaining the period clustering of AXPs. As discussed above, the source emits strong radiation only in the last ’tracking’ phase when the spin and Keplerian periods are comparable, i.e. there arises a natural selection effect. Another implication of the accretion model that can be seen in observational analysis is the noisy timing instead of steady spin down because of the torque transfer during the accretion (Lipunov et al., 1992).

The model of CHN00 is improved throughout time to account for the high magnetic fields of AXPs and SGRs deduced from their magnetar-like bursts. In the recent model the pulsar has a high quadrupole field of $10^{14} - 10^{15}$ G responsible for the bursts, and a regular dipole magnetic field of $10^{12} - 10^{13}$ G that is acceptable by the previous model (Ekşı and Alpar, 2003; Ertan and Alpar, 2003; Ertan et al., 2006).

2.6 Accretion Torque

Most of the pulsars (neutron stars observed to send pulses) are found to have varying spin (or pulse) periods. The change is a net effect of the external and internal torques exerted on the star. External torques may be due to magnetic effects, accreted matter, etc., internal torques are mostly because of the angular velocity difference between the solid crust and superfluid interior of the neutron star. The different features distinguished by the pulse timing measurements are associated with those internal and external factors depending mostly on their time-scales. External effects reveal themselves in longer periods of time while internal torques cause shorter-time-scale variations (Lamb, 1989).

2.6.1 Accretion Torque in Disc-fed Pulsars

In the simplest case, a Keplerian disc exerts some torque on the neutron star since the accreted material generally does not have the same angular momentum as the neutron star surface (Pringle and Rees, 1972; Davidson and Ostriker, 1973; Lamb et al., 1973). Hence, the starting point is the transfer of the angular momentum of the inner disc, which is $l_{\rm in} = \sqrt{GMr_{\rm in}}$ $l_{\rm in}$ being the specific angular momentum, to the star by applying the accretion torque, if magnetic and viscous stresses are ignored

$$N_0 = \dot{M} l_{\rm in}. \tag{2.32}$$

The angular momentum of the neutron star is $J_s = I_s \Omega_s$ where I_s is the moment of inertia and Ω_s is the angular velocity of the star. Conservation of angular momentum leads to the equality of the change in the angular momentum and and the accretion torque:

$$\dot{J}_s = \frac{d}{dt}(I_s \Omega_s) = \dot{M} l_{\rm in}. \tag{2.33}$$

The rotational response of the star is expressed by

$$\dot{\Omega}_s = \frac{\dot{M}}{M}\left(\frac{l_{\rm in}}{l_s} - \frac{d\ln I_s}{d\ln M}\right)\Omega_s \tag{2.34}$$

where $l_s = J_s/M$ is the specific angular momentum of the star. It is clear that the relation between terms inside the parenthesis determines whether the neutron star will spin-down or spin-up. A dimensionless parameter can be defined to express this more clearly:

$$\zeta = \frac{l_{\rm in}}{l_s}\left(\frac{d\ln M}{d\ln I_s}\right) = \frac{l_{\rm in}}{\Omega_s}\left(\frac{dM}{dI_s}\right), \tag{2.35}$$

and using this (2.34) becomes

$$\dot{\Omega}_s = (\zeta - 1)\,\frac{\dot{M}}{M}\left(\frac{d\ln I_s}{d\ln M}\right)\Omega_s, \tag{2.36}$$

and whether the neutron star spins up or spins down depends on $\zeta > 1$ or $\zeta < 1$. respectively. There is an interesting case which can be seen if the rate of change of the rotational energy is calculated

$$\dot{E}_{\rm rot} = \frac{d}{dt}\left(\frac{1}{2}I_s\Omega_s^2\right) = 2\left(\zeta - \frac{1}{2}\right)\frac{\dot{M}}{M}\left(\frac{d\ln I_s}{d\ln M}\right)E_{\rm rot}. \tag{2.37}$$

It is apparent that when $1/2 < \zeta < 1$ the star gains rotational energy, but this range is in the interval that the star spins down. In fact, for intermediate mass neutron stars $\zeta \approx \frac{l_{\rm in}}{l_s} = \frac{\Omega_K(r_{\rm in})}{\Omega_s}\left(\frac{r_{\rm in}}{R}\right)^2$ holds and since $r_{\rm in} \gg R$, the dimensionless parameter is calculated to be much larger than 1, which means that the spin-up term is usually the dominant one.

The realistic situation was pictured by Ghosh et al. (1977) (also see (Ghosh and Lamb, 1979a,b): the total external torque in the case of time independent, axisymmetric, steady accretion flow is given by

$$N = \int_S \left(-\rho\bar{\omega}^2\vec{v}_p\Omega + \bar{\omega}\frac{B_\phi\vec{B}_p}{4\pi} + \eta\bar{\omega}^2\vec{\nabla}\Omega\right)\cdot\hat{n}dS \tag{2.38}$$

where $\bar{\omega}$ is the cylindrical radius, v_p and Ω are poloidal and angular velocity of the plasma. As expected, in the parenthesis, the first term is the matter contribution, the second term is the magnetic contribution and the last term is the viscosity term. Since these effects dominate at different distances from the surface of the star, Ghosh and Lamb (1979b) selects a surface which is the union of three parts to evaluate the integral as seen in Fig. 2.6: S_1 is a cylindrical surface at radius r_0 which separates the boundary layer from the outer transition region, S_2 is composed of two sheets just above and below the disc extending from r_0 to infinity, and S_3 is the union of two hemispherical surfaces at infinity. The integral over S_3 vanishes, the integral over S_2 gives the torque $N_{\rm out}$ applied by the magnetic field lines of the outer transition zone, and the integral over S_1 is the torque $N_{\rm in}$ of the magnetic field lines of the inner transition zone. For $N_{\rm in}$ only material stress contributes (since viscous stress is negligible in S_1 and magnetic stress does not have perpendicular component on this surface); thus,

$$\begin{aligned} N_{\rm in} &\approx -\rho v_r r_0^2 \Omega_K(r_0) \cdot 2\pi r_0 \cdot 2h \\ &= \dot{M}(GMr_0)^{1/2} \equiv N_0 \end{aligned} \tag{2.39}$$

where h is the semi-thickness of the disc. On the other hand, $N_{\rm out}$ is dominated by the magnetic stress since the viscous stress does not have any perpendicular component and the material stress is negligible (matter flow is along S_2). Hence

$$N_{\rm out} = \int\limits_{S_2} (rB_z B_\phi/4\pi) dS. \tag{2.40}$$

As a result, the total torque on the neutron star is $N = N_{\rm in} + N_{\rm out}$ and this can be expressed as

$$N = n(\omega_s) N_0 \tag{2.41}$$

where $n(\omega_s)$ is the dimensionless accretion torque,

$$n(\omega_s) = 1 + \frac{1}{2}(1 - \omega_s)^{-1} \times \int\limits_1^{y_s} b_{\rm out}(y)(y^{-3/2} - \omega_s) y^{-31/40} dy, \tag{2.42}$$

which is determined only by the fastness parameter (Elsner and Lamb, 1977)

$$\omega_s \equiv \Omega_s/\Omega_K(r_0), \tag{2.43}$$

the dimensionless outer radius of the transition zone, $y_s = r_s/r_0$, and the dimensionless poloidal magnetic field in the outer transition zone, $b_{\rm out}(y) \equiv B_z/\mu b_0 r^{-3}$ (Ghosh and Lamb, 1979a). (2.42) can be approximated as (Ghosh and Lamb, 1991)

$$n(\omega_s) \approx 1.4 \left(\frac{1 - \omega_s/\omega_c}{1 - \omega_s} \right), \tag{2.44}$$

where ω_c is the critical value of fastness parameter at which the accretion torque vanishes, and the fastness parameter can be expressed in terms of μ, M, Ω_s and $\dot{M}$ using the approximate inner radius of the disc, which is $r_0 \approx 0.52 r_A$, (Ghosh and Lamb, 1979b)

$$\omega_s = 1.2 P^{-1} \dot{M}_{17}^{-3/7} \mu_{30}^{6/7} (M/M_\odot)^{-5/7}. \tag{2.45}$$

where P is the spin period in seconds and $\dot{M}_{17}$ is $\dot{M}$ in units of 10^{17} g.s^{-1}.

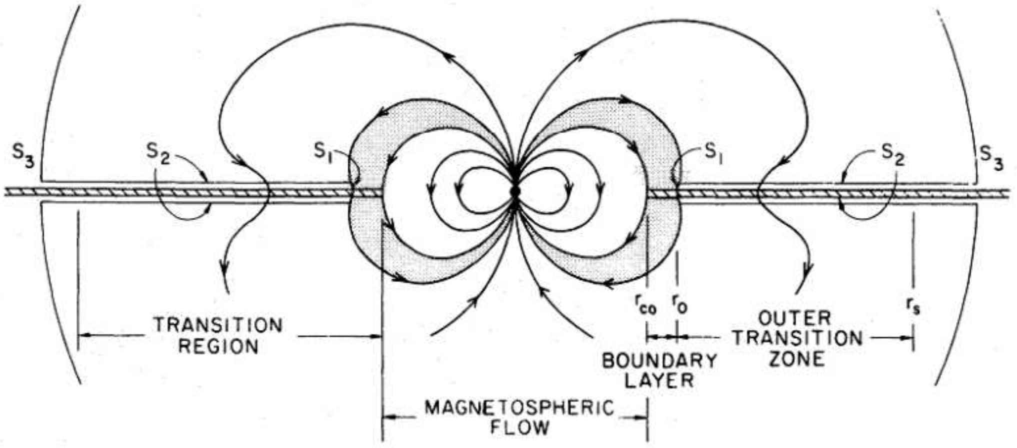

Figure 2.6: Surfaces defined by Ghosh and Lamb (1979b) to evaluate (2.38). S_1 is a cylindrical surface at radius r_0 which separates the boundary layer from the outer transition region, S_2 is composed of two sheets just above and below the disc extending from r_0 to infinity, and S_3 is the union of two hemispherical surfaces at infinity. The size of the boundary layer $\delta = r_0 - r_{\rm co}$ is around $0.04 r_0$.

Since the spin period, the mass accretion rate and the magnetic field directly affect the fastness parameters, whether the star spins up or down is determined by their relative magnitudes. For instance, in the case of a given mass and magnetic moment, if the spin period is long enough to make $\omega_s \ll 1$, the star experiences a strong spin-up torque. As P gets smaller towards the critical spin period P_c at which $\omega_s = \omega_c$, the spin-up torque vanishes, and when P becomes less than P_c the star goes through a spin-down phase. Hence, the star tends to get closer to P_c that corresponds to its accretion rate and remain there.

In the second case, if $\dot{M}$ is sufficiently large to make ω_s small compared to unity, the star spins up, and vice versa. The decrease of the magnitude of the spin-down torque continues until the mass accretion rate reaches a minimum at which $\omega_s = \omega_{\rm max}$, and the values of $\dot{M}$ less than this limit cannot provide a steady matter flow.

The critical value ω_c is estimated to be $\sim 0.35 - 0.85$, and the maximum value $\omega_{\rm max} \sim 1$ (Lamb, 1989).

It is apparent that the main parameter which decides if the star will spin up or spin down is the fastness parameter: In the case of a slowly rotating neutron star in the same direction with its accretion disc, the star receives positive angular momentum and spins up; if they are rotating in opposite directions the star spins down with the negative angular momentum. When the rotation rate of the neutron star is huge, it spins down for either direction of the accretion matter flow. Combining the equations $2\pi I\dot{\nu} = n(\omega_s)\dot{M}l_{\rm in}$, $L = \eta\frac{GM\dot{M}}{R}$, where $\eta \sim 1$ is the efficiency factor, and the expression for the Alfvén radius, the following relation between the rate of change of the pulse frequency and the luminosity can be obtained

$$\dot{\nu} = f_N(\mu, M)n(\omega_s)L^{6/7} = f_N(\mu, M)n(\omega_s)(4\pi d^2F)^{6/7} \tag{2.46}$$

where f_N is a function depending on μ and M, d is the distance to the source, and F is the X-ray flux on the observing instrument.

2.6.2 Accretion Torque in Wind-fed Pulsars

In the case of stellar wind accretion, the radial velocity of the captured material near the capture radius, r_a is expected to be very large. In addition, the magnetospheric effects are confined to a much smaller radius than r_a (Lamb et al., 1973; Arons and Lea, 1976; Elsner and Lamb, 1977) and so the the material flow is the most dominant component to exert torque on the neutron star:

$$N = \dot{M}l_a \tag{2.47}$$

where $\dot{M}$ is the rate of mass capture and l_a denotes the specific angular momentum of the accreting matter at radius r_a, which is expressed by (2.17). The capture rate is calculated from

$$\dot{M} = \pi\rho_w v_0 r_a^2 \tag{2.48}$$

where ρ_w is the wind density. Substituting the capture radius in (2.15) with $v_{\rm rel} \approx v_0$, the accretion torque is obtained as

$$N = \pi^2(2GM)^4\rho_w v_0^{-7}P_{\rm orb}^{-1} \tag{2.49}$$

where $P_{\rm orb}$ is the orbital period of the system. The relation between the frequency derivative and luminosity can also be derived for wind-fed pulsars (Ghosh and Lamb, 1979b)

$$\dot{\nu} \propto R(M/M_\odot)^{-1}I^{-1}l_aL. \tag{2.50}$$

There is no magnetic term in this expression since the magnetosphere does not have any effect on $\dot{M}$ or l_a. The stellar wind structure varies from source to source, and even in the same binary system. Hence, different physical properties leads to various relation between $\dot{\nu}$ and L:

1. when ρ_w is variable but v_0 is constant, which is the case when $v_{\rm orb} \gg v_w$, $\dot{M}$ only changes with ρ_w, so $\dot{\nu} \propto L$,
2. when ρ_w is constant but v_0 is variable, $r_a \propto v_0^{-2}$, $l_a \propto v_0^{-4}$ and $\dot{M} \propto v_0^{-3}$, so $\dot{\nu} \propto L^{7/3}$,
3. when both ρ_w and v_0 are variable but $\rho_w v_0 = const$, $r_a \propto \rho_w^2$, $l_a \propto \rho_w^4$ and $\dot{M} \propto \rho_w^4$, so $\dot{\nu} \propto L^2$.

Wang (1981), Anzer et al. (1987) and Ho (1988) have investigated more complicated situations when there are velocity and density gradients, to understand torque-reversals in wind-fed systems. In addition, some unstable circulations may arise in the flow due to the irregular variations of stellar winds in time-scales from minutes to years (Nagase, 1989). These can also reverse the direction of the accretion flow which is known as the flip-flop behaviour in wind-fed HMXBs and cause spin-up and spin-down transitions in short time-scales.

2.7 Pulse Profiles and Energy Spectra of Accretion Powered Pulsars

A pulse profile is the variation with time of the signal strength from a pulsar, usually plotted against pulse phase (also known as pulse longitude), where one complete rotation is equal to 360^0 of longitude. Pulse profiles vary erratically from pulse to pulse, but the integrated pulse profile, the average of a large number of pulse profiles, is characteristic of each individual pulsar. The shape of the profile is believed to reflect the structure of the pulsar's emitting region.

The structure of a pulsar's pulse profile is determined by three fundamental directions: the directions of the pulsar's rotation and magnetic axes, and the line of sight of the observer (Wang and Welter, 1981; White et al., 1983; Nagase, 1989; Ghosh, 2007). Hence, the pulse shapes and amplitudes of pulsars change from source to source, which is also affected from the emission processes and the transfer of matter through magnetized plasma. Nagase (1989) separated these pulse profiles into five main groups (see Fig. 2.7 for examples):

1. Single peak sinusoidal profiles which have little energy dependence (e.g. X Per, GX 304-1)
2. Double peak sinusoidal profiles with different amplitudes which have little energy dependence (e.g. SMC X-1, GX 301-2, 4U 1538-52)
3. Asymmetric single peak profiles with some additional features which have little energy dependence (e.g. Cen X-3, GX 1+4)
4. Single sinusoidal peak profiles at high and low energies, which turn into a close double peak profile at intermediate energies (e.g. Her X-1, 4U 1626-67)
5. Double peak sinusoidal profiles at high energy and complex multiple peak structure at low energy (e.g. Vela X-1, A 0535+26)

The basic reason why sometimes one and sometimes two peaks are observed is the relation between the angles of the magnetic axis, α and the line of sight with respect to the rotation axis, β: if $\alpha + \beta < \pi/2$ only one magnetic pole is visible producing a single peak; on the other hand, if $\alpha + \beta > \pi/2$ both of the poles can be seen, so the two peaks (Wang and Welter, 1981). Generally, the two peaks are not symmetric and this is due to the differences between the emission regions in the polar caps or an offset of the magnetic axis (Parmar et al., 1989; Leahy, 1991).

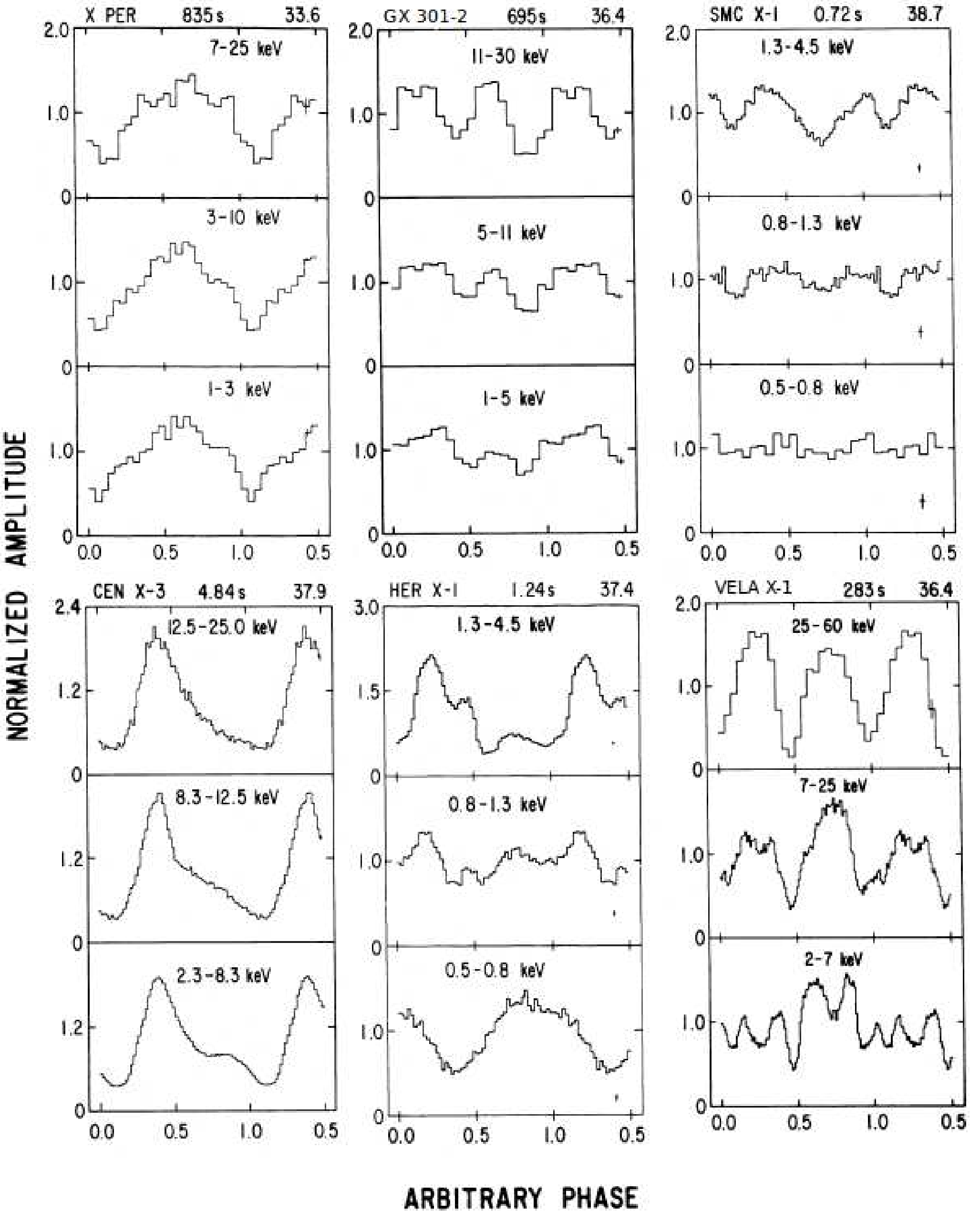

Figure 2.7: Pulse profiles of 6 accretion powered pulsars in different energy bands. Source names, pulse periods and luminosities (logarithm of) are given at the top of each panel. Figures are taken from White et al. (1983)

The energy spectra of accretion powered pulsars is mostly dominated by the thermal emission together with some complicated effects of magnetic field. The X-ray spectra can be usually modelled by ”power law with a high energy cut-off” which is expressed by the following function (White et al., 1983; Coburn et al., 2002)

$$N(E) = N_0 E^{-\Gamma} \times \begin{cases} 1, & E \leq E_{\rm cut} \\ e^{(E_{\rm cut}-E)/E_f} & E \geq E_{\rm cut} \end{cases} \tag{2.51}$$

in which the photon index Γ, and the high energy cut-off value $E_{\rm cut}$ are the characteristic values that help us to understand the emission features. Γ is in the range 0–1, and both $E_{\rm cut}$ and E_f are in the range 10–20 keV.

The X-rays emitted from the pulsar lose energy due to photoelectric absorption by the medium through which they travel. The function that describes this lost is as follows (Nagase, 1989)

$$M(E) = e^{n_{\rm H}\sigma(E)}. \tag{2.52}$$

The hydrogen absorption column density, $n_{\rm H}$ (in units of 10^{22} atoms.cm^{-2}), varies according to the coordinate of the source, while the photoelectric cross-section, $\sigma(E)$, depends on the composition of different elements in the medium through the line of sight. In fact, $n_{\rm H}$ is expected to change according to the position of an accretion powered pulsar in its binary orbit because of the variation in the distribution of the accreting matter and outer atmosphere of the companion. Observations have shown that the value of $n_{\rm H}$ may vary up to two orders of magnitude (e.g. Vela X-1 (Haberl and White, 1990), 4U 1907+09 (Roberts et al., 2001)).

The strong magnetic fields of the pulsars also reveal themselves in the X-ray spectra. The most common and explicit effect is the cyclotron resonance scattering features (CRSFs), which are caused by the scattering of photons in resonance by electrons whose energy states are quantized into Landau levels by the magnetic field (Meszaros, 1992), and the corresponding harmonic ”cyclotron” lines can be used to estimate the magnitude of the surface magnetic field.

A charged particle with some velocity starts to rotate around the magnetic field lines since the force due to the existence of magnetic field is orthogonal to its instantaneous direction of motion. There is a rotation frequency corresponding to this rotational motion which can be determined by the equality of the centripetal and magnetic forces, and it is called the cyclotron frequency. However, this motion is not a steady rotational motion as charged particles emit radiation if they have acceleration. Hence, most of the radiation is expected to be as a spectral line centred at the fundamental cyclotron resonance frequency

$$\omega_{\rm cyc} = \frac{eB}{m_e} \tag{2.53}$$

where e and m_e are the charge and mass of the electron. Considering the red-shift effect of the gravitational field of the pulsar, the relation between the line energy and the magnetic field is obtained as

$$E_0 = E_{\rm cyc}(1+z)^{-1} = 11.6B_{12}(1+z)^{-1} = 11.6B_{12}\left(1 - \frac{2GM}{Rc^2}\right)^{1/2} \text{ keV}, \tag{2.54}$$

where $E_{\rm cyc} = \hbar\omega_{\rm cyc}$, z is the gravitational red-shift, B_{12} is B in units of 10^{12} G, and R is the distance of the region where the line is formed from the centre of the neutron star.

There is an interesting correlation between the cyclotron line energy and the high energy cut-off, which is revealed by the observations (Makishima et al., 1999; Coburn et al., 2002), and this relation is a simple power law $E_{\rm cut} \propto E_0^{0.7}$ (Makishima et al., 1999).

CHAPTER 3

ACCRETION DISCS

The disc flow is generally confined so close to the orbital plane that the disc can be assumed to be two dimensional. This thin disc approximation is proved to be a correct approach in many cases.

3.1 Radial Disc Structure

As mentioned above, the accretion disc is primarily a ring at R_{circ} and evolves to be a disc in time under some viscous effects. When the mass and angular momentum conservation equations are solved involving a constant viscous torque, the development of surface density is found to be (Frank et al., 2002)

$$\Sigma(x,\tau) = \frac{m}{\pi R_0^2}\tau^{-1}x^{-1/4}exp\left(-\frac{(1+x^2)}{\tau}\right)I_{1/4}(2x/\tau) \tag{3.1}$$

where $I_{1/4}(z)$ is a modified Bessel function, $x = R/R_0$ and $\tau = 12\nu t R_0^{-2}$. This gives the Dirac delta function at $t = 0$ and a spreading structure as time goes by, as expected. Fig. 3.1 shows $\Sigma(x,\tau)$ as a function of x for various values of τ.

The typical time-scale for a ring of radius R to spread is

$$t_{\text{visc}} \sim R^2/\nu \tag{3.2}$$

as

$$v_R \sim \nu/R \tag{3.3}$$

$$t_{\text{visc}} \sim R/v_R \tag{3.4}$$

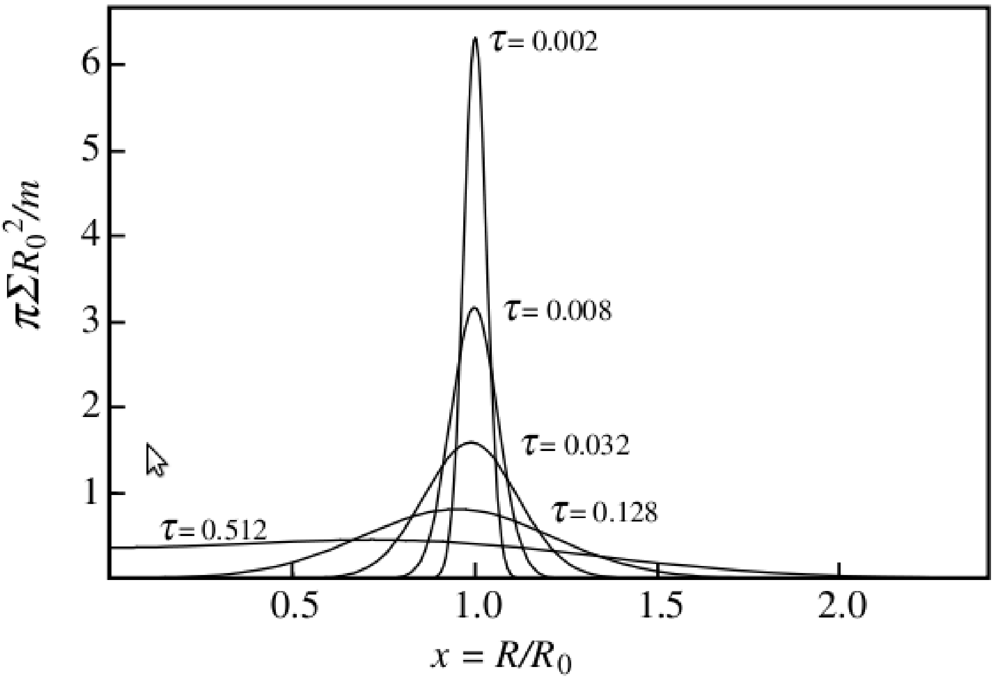

Figure 3.1: The spread of a ring of matter with mass m from an initial Kepler orbit at $R = R_0$ by viscous torques. Σ is the surface density, $x = R/R_0$ and τ is the dimensionless time variable $\tau = 12\nu t R_0$, with ν the constant kinematic viscosity.

t_{visc} is known as the viscous or radial drift time-scale and it is the time needed for a disc to form entirely ever since the primary ring.

3.2 Steady Thin Discs

The viscous time-scale is the longest time-scale of the accretion disc means that external variations with time-scales longer than t_{visc} do not have considerable effects on the disc, and so the disc arrives at a steady-state structure (can be applied to the conservation equations). In this state, the following expression is valid in the absence of strong magnetic fields (Frank et al., 2002)

$$\nu\Sigma = \frac{M}{3\pi}\left[1 - \left(\frac{R_*}{R}\right)^{1/2}\right] \tag{3.5}$$

and the viscous dissipation, the rate of energy loss due to viscosity, becomes

$$D(R) = \frac{3GM\dot{M}}{8\pi R^3}\left[1 - \left(\frac{R_*}{R}\right)^{1/2}\right]. \tag{3.6}$$

(so the energy flux of the disc is found to be independent of ν parameter).

The disc contains no flow in the vertical direction, say this is the z-direction. Then, hydrostatic equilibrium, the balance between pressure and gravitation gradients which is necessary for stability of the disc, must hold in z-direction

$$\frac{1}{\rho}\frac{\partial P}{\partial z} = \frac{\partial}{\partial z}\left[\frac{GM}{(R^2+z^2)^{1/2}}\right] \tag{3.7}$$

For a thin disc, $z \ll R$, so

$$\frac{1}{\rho}\frac{\partial P}{\partial z} = -\frac{GMz}{R^3} \tag{3.8}$$

Using the typical scale-height of the disc in the z-direction, H, and $z \sim H$ with $P \sim \rho c_s^2$, where c_s is the sound speed, one can arrive at

$$H \simeq c_s \left(\frac{R}{GM}\right)^{1/2} R \tag{3.9}$$

But the thin disc approximation requires $H \ll R$, which leads to

$$c_s \ll \left(\frac{GM}{R}\right)^{1/2} \tag{3.10}$$

i.e. local Kepler velocity should be highly supersonic for a thin disc (not necessarily throughout the disc). On the other hand, the radial velocity is determined to be

$$v_R = -\frac{3\nu}{2R}\left[1 - \left(\frac{R_*}{R}\right)^{1/2}\right]^{-1} \tag{3.11}$$

which is at the order of ν/R as expected earlier in (3.4) And involving the Shakura-Sunyaev α-parametrization

$$v_R \sim \frac{\nu}{R} \sim \alpha c_s \frac{H}{R} \ll c_s \tag{3.12}$$

At this point, the Mach number, $\mathcal{M}$

$$\mathcal{M} \equiv v_\phi / c_s \tag{3.13}$$

(3.12) and (3.9) can be written

$$H \sim \mathcal{M}^{-1} R, \qquad v_R \sim \alpha \mathcal{M}^{-1} c_s \tag{3.14}$$

All these effort is to determine the disc parameters such as density, temperature, thickness, opacity, viscosity, radial velocity of the accreting matter, etc. Collecting the equations obtained so far together with the pressure, which is the sum of radiation and gas pressures, and optical depth, τ, there remains to solve these equations with the appropriate approximations

$$\begin{aligned}
\rho &= \Sigma/H, \\
H &= c_s R^{3/2}/(GM)^{1/2}, \\
c_s &= P/\rho, \\
P &= \frac{\rho k T_c}{\mu m_p} + \frac{4\sigma}{3c} T_c^4, \\
\frac{4\sigma T_c^4}{3\tau} &= \frac{3GM\dot{M}}{8\pi R^3}\left[1 - \left(\frac{R_*}{R}\right)^{1/2}\right], \\
\tau &= \Sigma\kappa_R(\rho, T_c) = \tau(\Sigma, \rho, T_c) \\
\nu\Sigma &= \frac{\dot{M}}{3\pi}\left[1 - \left(\frac{R_*}{R}\right)^{1/2}\right], \\
\nu &= \nu(\Sigma, \rho, T_c, \alpha, ...)
\end{aligned} \tag{3.15}$$

3.3 The Structure of Steady α-discs (The ’Standard Model’)

The 8th equation (counting from top to bottom) in the set (3.16) implies that the dependence of the viscosity to the disc parameters is not clear. This ambiguity is removed by Shakura-Sunyaev α-prescription (2.13). The similar problem with the equation 6 is solved by assuming the Rosseland mean opacity which is given by Kramer’s law

$$\kappa_R = 5 \times 10^{24} \rho T_c^{-7/2} \quad \mathrm{cm^2 g^{-1}} \tag{3.16}$$

After the necessary calculations, the Shakura-Sunyaev disc solution turns out to be (Frank et al., 2002)

$$\begin{aligned}
\Sigma &= 5.2\alpha^{-4/5}\dot{M}_{16}^{7/10} m_1^{1/4} R_{10}^{-3/4} f^{14/5} \quad \mathrm{g.cm^{-2}}, \\
H &= 1.7 \times 10^8 \alpha^{-1/10}\dot{M}_{16}^{3/20} m_1^{-3/8} R_{10}^{9/8} f^{3/5} \quad \mathrm{cm}, \\
\rho &= 3.1 \times 10^{-8} \alpha^{-7/10}\dot{M}_{16}^{11/20} m_1^{5/8} R_{10}^{-15/8} f^{11/5} \quad \mathrm{g.cm^{-3}}, \\
T_c &= 1.4 \times 10^4 \alpha^{-1/5}\dot{M}_{16}^{3/10} m_1^{1/4} R_{10}^{-3/4} f^{6/5} \quad \mathrm{K}, \\
\tau &= 190\alpha^{-4/5}\dot{M}_{16}^{1/5} f^{4/5}, \\
\nu &= 1.8 \times 10^{14} \alpha^{4/5}\dot{M}_{16}^{3/10} m_1^{-1/4} R_{10}^{3/4} f^{6/5} \quad \mathrm{cm^2 s^{-1}}, \\
v_R &= 2.7 \times 10^4 \alpha^{4/5}\dot{M}_{16}^{3/10} m_1^{-1/4} R_{10}^{-1/4} f^{-14/5} \quad \mathrm{cm.s^{-1}},
\end{aligned} \tag{3.17}$$

where $f = \left[1 - \left(\frac{R_*}{R}\right)^{1/2}\right]^{1/4}$, $\dot{M}_{16} = \dot{M}/(10^{16}\mathrm{g.s}^{-1})$, $R_{10} = R/(10^{10}\mathrm{cm})$ and $m_1 = M/M_\odot$ (with μ=0.615 is applied). For $\alpha \leq 1$ the disc quantities are calculated to be in reasonable orders although α can in general be a function of $\dot{M}$, M, R, and z. From (3.18), one can deduce the ratio

$$H/R = 1.7 \times 10^{-2} \alpha^{-1/10} \dot{M}_{16}^{3/20} m_1^{-3/8} R_{10}^{1/8} f^{3/5} \tag{3.18}$$

or substituting $L_x = GM_1\dot{M}/(10^6 R_{10km}\mathrm{cm}) = 10^{37} L_{37}$ erg/s and $m_1 = 1.4M_{1.4}$:

$$H/R \simeq 2.3 \times 10^{-2} \alpha^{-1/10} R_{10km}^{3/20} M_{1.4}^{-21/40} L_{37}^{3/20} R_{10}^{1/8} \tag{3.19}$$

There are some cases where the thin disc approximation does not hold. These cases are related to the assumptions made while deriving the equation set (3.18). An apparent case is the conditions when Kramer's opacity is not valid and this arises in the inner regions of the disc near the neutron star or the black hole. Here electron scattering is the dominant opacity and the radiation may not be blackbody. If this case is combined with an increase in the ratio of radiation to gas pressure such that it becomes larger than 1, and a huge accretion rate of $\dot{M}_{16} \geq 1$, then the thin disc approximation breaks down. In other words, radiation pressure has such an effect to make the innermost regions of the disc quasi-spherical beyond some critical accretion rate. The disc is also expected to be 'thick' for disc temperatures larger than the blackbody temperature.

3.4 Time Dependence

In Section 3.2 we investigate the disc in the steady state. However, an accretion disc is open to external interventions and so it is necessary to work on the probable reactions of the disc to these experiences. By this way, it is easier to get information about the role of viscosity in accretion disc dynamics. The disc structure may modify on some typical time-scales. The one known to be the longest is the viscous time-scale

$$t_{\mathrm{visc}} \sim \frac{R^2}{\nu} \sim \frac{R}{v_R} \tag{3.20}$$

which is a measure of the diffusion time of matter through the disc under the effect of the viscous torques. The shortest characteristic time-scale is the dynamical time-scale observed to be the duration that inhomogeneities generate some specific variations in the disc light

$$t_\phi \sim \frac{R}{v_\phi} \sim \Omega_K^{-1}. \tag{3.21}$$

Deviations from hydrostatic equilibrium in the z-direction are smoothed out on a time-scale

$$t_z = H/c_s \tag{3.22}$$

and from (3.14) $t_z \sim R/\mathcal{M}c_s = R/v_\phi \sim t_\phi$. There is also the thermal time-scale which is the time-scale to readjust the thermal equilibrium:

$$t_{\mathrm{th}} = \frac{\text{heat content per unit disc area}}{\text{dissipation rate per unit disc area}} \sim \Sigma c_s^2/D(R) \sim \frac{R^3 c_s^2}{GM\nu} \sim \frac{c_s^2}{v_\phi^2}\frac{R^2}{\nu} \sim \mathcal{M}^{-2} t_{visc} \tag{3.23}$$

where (3.6) is used for $D(R)$. Furthermore, α-parametrization allows direct comparison between these time-scales

$$t_{\mathrm{visc}} \sim \frac{R^2}{\nu} \sim \frac{1}{\alpha}\frac{R}{H}\frac{R}{v_\phi}\frac{v_\phi}{c_s} \sim \alpha^{-1}\mathcal{M}^{-2}t_\phi, \tag{3.24}$$

$$t_\phi \sim t_z \sim \alpha t_{\mathrm{th}} \sim \alpha (H/R)^2 t_{\mathrm{visc}} \tag{3.25}$$

Hence, assuming $\alpha \leq 1$, $t_\phi \sim t_z \leq t_{\mathrm{th}} \ll t_{\mathrm{visc}}$. Numerical calculations for α-disc solutions reveal (Frank et al., 2002)

$$\begin{aligned} t_\phi \sim t_z \sim \alpha t_{\mathrm{th}} &\sim 100 m_1^{-1/2} R_{10}^{3/2}\,\mathrm{s}, \\ t_{\mathrm{visc}} &\sim 3\times 10^5 \alpha^{-4/5} \dot{M}_{16}^{-3/10} m_1^{1/4} R_{10}^{5/4}\,\mathrm{s}. \end{aligned} \tag{3.26}$$

It is apparent that while the dynamical and thermal time-scales are of the order of minutes, the viscous time-scale is of the order of days to weeks.

This sharp difference in the time-scales enables us to distinguish different types of instability. For example, in the case of thermal instabilities, the vertical structure responds very fast and maintains the hydrostatic equilibrium. The surface density, on the other hand, reacts in the viscous time-scale, and since this would be very slow the surface density can be assumed to be constant in such a case.

In order to consider the changes in the disc structure that happen on the viscous time-scale, both thermal and hydrostatic equilibrium can be taken to be undisturbed. Mathematically, the equations in the set (3.16) except the 5th and 7th (counting from top) remain unchanged. Reconstructing the equations as

$$\frac{4\sigma}{3\tau}T_c^4 = \frac{9}{8}\nu\Sigma\frac{GM}{R^3}, \tag{3.27}$$

$$2\pi R\frac{\partial\Sigma}{\partial t} = \frac{\partial\dot{M}}{\partial R} \implies \frac{\partial\Sigma}{\partial t} = \frac{3}{R}\frac{\partial}{\partial R}\left\{R^{1/2}\frac{\partial}{\partial R}\left(\nu\Sigma R^{1/2}\right)\right\}, \tag{3.28}$$

it appears that only (3.28) depends on time; thus, it will be easier to solve the equation set if the other parameters are expressed in terms of Σ. The first four equations in (3.16) can be combined to yield

$$\frac{GM\Sigma H}{R^3} = \frac{kT_c\Sigma}{\mu m_p H} + \frac{4\sigma}{3c}T_c^4. \tag{3.29}$$

From (3.27) and the sixth equation of (3.16) one can obtain

$$T_c^4 = \frac{27}{32\sigma}\Sigma^2\kappa_R\nu\frac{GM}{R^3}, \tag{3.30}$$

and this can be put in the following form using the Kramers' form (3.16) and the α-prescription (2.13)

$$T_c^4 \propto \alpha\Sigma^3 H T_c^{-7/2}(GM/R^3)^{1/2}. \tag{3.31}$$

This equation can be used in (3.29) and H is obtained as a function of R and Σ. Then, (2.13) turns into

$$\nu = \alpha c_s H = \alpha(kT_c/\mu m_p)^{1/2}H = \nu(R,\Sigma). \tag{3.32}$$

At this point, (3.28) becomes a nonlinear diffusion equation for $\Sigma(R,t)$ and requires numerical analysis to acquire a solution. Nevertheless, some implications of (3.28) worth mentioning.

Considering a deviation from the steady state $\Sigma_0(R)$ in the form $\Sigma(R) = \Sigma_0(R) + \Delta\Sigma(R)$, and letting $\mu = \nu\Sigma$ so that $\Delta\mu = (\partial\mu/\partial\Sigma)\Delta\Sigma$, (3.28) evolves into

$$\frac{\partial}{\partial t}(\Delta\mu) = \frac{\partial\mu}{\partial\Sigma}\frac{3}{R}\frac{\partial}{\partial R}\left[R^{1/2}\frac{\partial}{\partial R}\left(R^{1/2}\Delta\mu\right)\right]. \tag{3.33}$$

The key factor in this equation is $\partial\mu/\partial\Sigma$. The sign of it determines the stability of disc flow: in the case of negative derivative, material would tend to accumulate towards denser regions, and the disc would disintegrate into rings on a time-scale t_{visc} (Frank et al., 2002). Hence, $\partial\mu/\partial\Sigma > 0$ should be satisfied to maintain the steadiness of the disc, and this leads to the conditions $\partial\dot{M}/\partial\Sigma > 0$ or $\partial T(R)/\partial\Sigma > 0$. The relation between $T(R)$ and Σ will reveal the conditions for stability.

For the regions where gas pressure dominates radiation pressure: $T_c \propto T_c^4/\tau$. Since $\tau \sim \kappa_R \rho H$ and $\kappa_R \propto \rho T_c^n$, $T^4 \propto T_c^{9/2-n}$. On the other hand, from the α-prescription we have $\nu = \alpha c_s H \propto T_c$ and $T^4 \propto \dot{M} \propto \nu\Sigma \propto T_c\Sigma$. Using all of these, the following relation is obtained

$$T \propto \Sigma^{(13-2n)/(28-8n)}. \tag{3.34}$$

$\partial T(R)/\partial\Sigma > 0$ corresponds to the range $7/2 < n < 13/2$ which is valid in hydrogen ionization zones, i.e. wherever $T \sim T_H \sim 6500$ K. An accretion disc may often have such unstable regions since the temperature should pass through this critical value as it is increasing.

The other case when the radiation pressure dominates the disc, which is the case in the central regions of discs around neutron stars and black holes, combined with a pure scattering opacity, κ_R = constant, yields the relation which is known as the Lightman-Eardley instability (Lightman and Eardley, 1974)

$$T \propto \Sigma^{-1/4}. \tag{3.35}$$

The next question need to be answered in the case of viscous instability is how the disc comes into equilibrium state again. One of the initial assumptions is the maintenance of the thermal equilibrium; however, it fails when $\partial T/\partial\Sigma < 0$. If Q^+ is the heating term and Q^- is the cooling term, then time dependence of temperature can be written as

$$\frac{\partial T}{\partial t} \propto Q^+ - Q^-. \tag{3.36}$$

The first order differential equations (3.28) and (3.36) are autonomous since they do not contain an explicit t-dependence; hence, it is possible to investigate the qualitative behaviour of the system without solving it. The system can be represented as

$$\dot{T} = h(T, \Sigma), \tag{3.37}$$

$$\dot{\Sigma} = \epsilon k(T, \Sigma), \tag{3.38}$$

where $\dot{} = \partial/\partial t'$, $t' = t/t_{th}$, $\epsilon = t_{th}/t_{visc}$, and h, k are transformed right-hand sides of (3.36) and (3.28), respectively. It is apparent that $\dot{T} = \dot{\Sigma} = 0$ is an equilibrium solution of the system. In Fig. 3.2 this is presented as the intersection of the curves $h = 0, k = 0$. The arrows in the figure denote the directions that the system evolves.

The motion in T is always much more rapid than that in Σ (since $t_{th} \ll t_{visc}$); hence, the system always proceed in T to reach $h = 0$ curve without any significant movement in Σ, and this happens on the thermal time-scale. Then, the system will move along this curve to reach the fixed point at the intersection with the $k = 0$ curve.

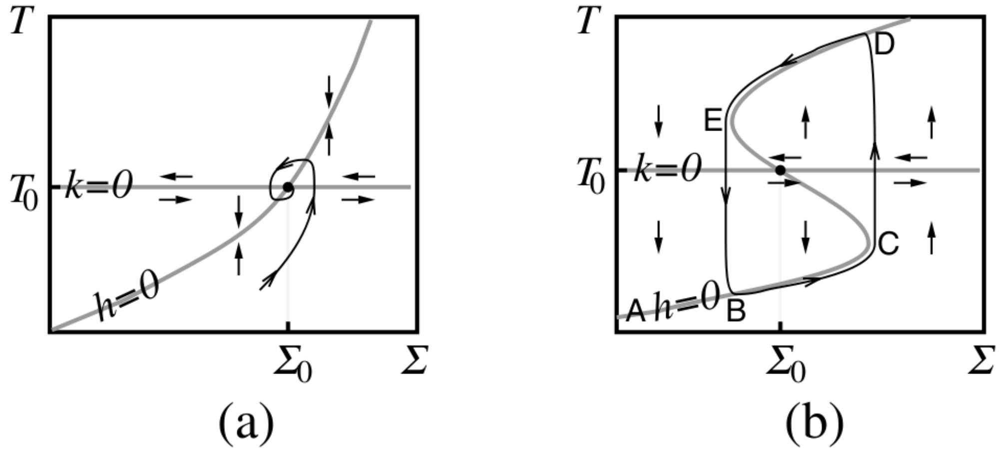

Figure 3.2: ”Phase plane in the vicinity of a fixed point, indicated by a solid dot at the intersection of the two critical curves $h = 0$ and $k = 0$: (a) stable fixed point; (b) unstable fixed point and stable limit cycle.” Frank et al. (2002)

The description of the situation above points out to two cases: The equilibrium point may be either on one branch which has positive slope, $\partial T/\partial\Sigma > 0$, or on the branch which has negative slope, $\partial T/\partial\Sigma < 0$. In the former case, the system will eventually find the equilibrium point and stay there (see Fig. 3.2(a)), but evolution way of the system for the latter case forbids the disc annulus to settle into a steady state as exhibited in Fig. 3.2(b).

3.5 Irradiation of Discs by the Central Source

The importance of radiation from an accretion disc is explained above, and dissipation is not the only reason for energy emission, irradiation of the disc by the central object is also significant for some systems. Point-like and extended central sources should be considered separately.

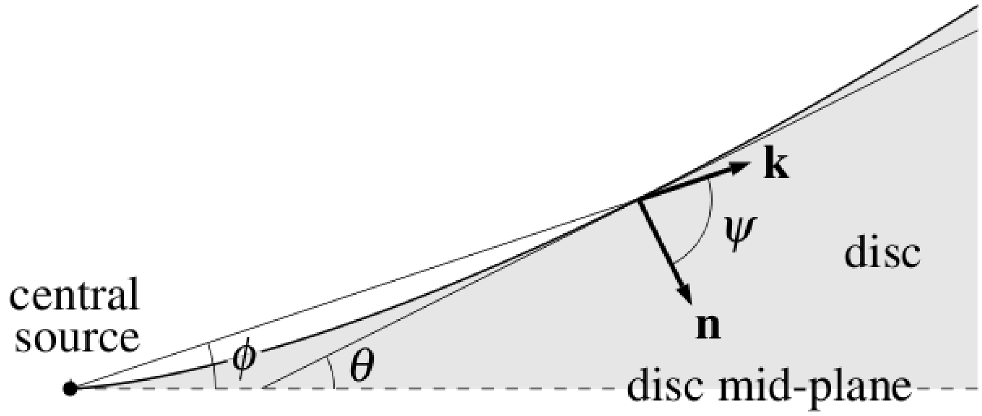

Figure 3.3: Geometry for irradiation (Figure is from Frank et al. (2002)). The direction of propagation of the radiation is along the unit vector **k** and the normal vector is **n**.

The flux of a point source crossing the surface of the disc at a radius R is

$$F = \frac{L_{pt}}{4\pi R^2}(1-\beta)\cos\psi, \tag{3.39}$$

where β is the effective fraction of the incident radiation scattered from the surface without absorption, and ψ is the angle between the local inward-directed disc normal and the direction of the incident radiation. Fig. 3.3 shows the disc geometry for irradiation, and there are the following relations between the angles and the disc thickness

$$\psi = \frac{\pi}{2} - \theta + \phi, \qquad \tan\theta = \frac{dH}{dR}, \qquad \tan\phi = \frac{H}{R}. \tag{3.40}$$

An effective temperature $T_{\rm pt}$ can be defined for the effect of irradiation, and using the smallness of dH/dR and H/R to obtain $\cos\psi \simeq \frac{dH}{dR} - \frac{H}{R}$ the ratio of the effective irradiation temperature to the effective temperature of the disc from (3.6) with $\sigma T^4(R) = D(R)$, is found to be (Frank et al., 2002)

$$\left(\frac{T_{\rm pt}}{T_{\rm eff}}\right)^4 = \frac{2}{3}\frac{RL_{\rm pt}}{GM\dot{M}}\frac{H}{R}\left[\frac{d\ln H}{d\ln R}\right](1-\beta). \tag{3.41}$$

$L_{\rm pt}$ is the luminosity of the central source and it is a good approximation to assume that it is due to accretion, which yields $L_{\rm pt} = GM\dot{M}/R_*$ In the resulting equation, $(H/R)\left[\frac{d\ln H}{d\ln R}\right](1-\beta)$ can be $\leq 10^{-3}$, so emission can be dominated by irradiation if the disc has a large enough R/R_* ratio, which is the case for low mass X-ray binaries ($R_* \sim 10^6$ cm and the outer disc radius is $\geq 10^{10}$ cm).

If the compact object is a black hole, then the central source for irradiation is the inner region of the disc. The calculations above still hold in this case with the addition of an extra factor $\sim H/R$. The effect of irradiation is weaker in this case, but it is still important.

However, for an extended source (central star with a larger vertical extension, like a white dwarf, or an accretion disc corona) the analogous ratio is (Frank et al., 2002)

$$\left(\frac{T_{\mathrm{ex}}}{T_{\mathrm{eff}}}\right)^4 = \frac{4}{9\pi}\frac{L_*}{L_{\mathrm{acc}}}(1-\beta) \tag{3.42}$$

Thus, the effective temperature is raised by only $\leq 2\%$.

Irradiation has several effects on an accretion disc. It causes a large temperature gradient along the disc which may result in bursts and outbursts. It has also some dynamical effects like warping of the disc by self-irradiation. We may focus on the dynamical effects rather than the energetic effects which are out of the scope of this thesis.

3.5.1 Warping of Discs

A significant effect of irradiation of an accretion disc is that it creates a torque on the optically thick disc surface because of the resulting radiation pressure. The torque appears when a small perturbation causes one side of the disc to receive more radiation than the other, and this will feed the initial asymmetry and then also the torque. In order for the disc to warp at some radius, a growing perturbation is required. The work of Pringle (1996) about ’Self Induced Warping of Accretion Discs’ reveals the following condition for warping

$$L \geq 12\pi^2 \nu_2 \Sigma v_\phi c \tag{3.43}$$

where ν_2 is the vertical kinematic viscosity coefficient. Using (3.5) and Keplerian velocity, this equation turns into

$$L \geq 4\pi \frac{\nu_2}{\nu} \dot{M} c^2 \left(\frac{R_{\mathrm{Schw}}}{2R}\right)^{1/2}, \tag{3.44}$$

in which $R_{\rm Schw} = 2GM/c^2$ holds. Moreover, assuming the central luminosity L originates from accretion at the steady rate $\dot{M}$ on to a compact object of radius R_*, then

$$L \simeq \dot{M}c^2 \frac{R_{\rm Schw}}{R_*}, \tag{3.45}$$

and finally the following equation can be used to judge whether warping is probable in various cases

$$\frac{R}{R_*} \geq 8\pi^2\psi^2 \frac{R_*}{R_{\rm Schw}} \tag{3.46}$$

where $\psi = \nu_2/\nu$. Indeed, for stellar mass neutron star and black hole binaries, where $M = 1M_\odot$ and $R_* = 10^6$ cm and $R_* = R_{\rm Schw}$, respectively, the minimum R calculated from (3.46) corresponds to reasonable orbits. With this result, it can be concluded that the thin disc approximation seems to be violated since warping increases the vertical extension of the disc. Nevertheless, in the local picture, the thin disc structure is still valid because the length-scale of warping is much larger than the local scale-height, H. The possible shapes of warping, on the other hand, can be deduced by numerical calculations. Fig. 3.4 shows some warped discs at different times.

3.6 Tides and Resonances

An accretion disc is not a generally quiet and peaceful place. Its thin plane structure may be destroyed easily and it might begin warping. One of the reasons for such a behaviour is the gravitational force exerted by the secondary star on the outer parts of the disc. Actually, the secondary just initiates the phenomenon; it is the viscosity, again, that prolongs the duration by applying torque to the matter rings in the disc. These tidal torques show some sharp modulations through the disc which is cut off at a particular radius as a result. The entire event may lead to significant variations in the disc properties most of which can be observable, like outbursts and superhumps.

Angular momentum transfer from inner parts to the outer parts of the disc requires a sink to absorb the angular momentum at the outer edge. There can be exchange of angular momentum with the secondary star; however, the resulting torque is not sufficient. The main agent is the viscosity again. It creates a net gravitational torque on the disc by distorting the symmetry about the line of centres, which is called the

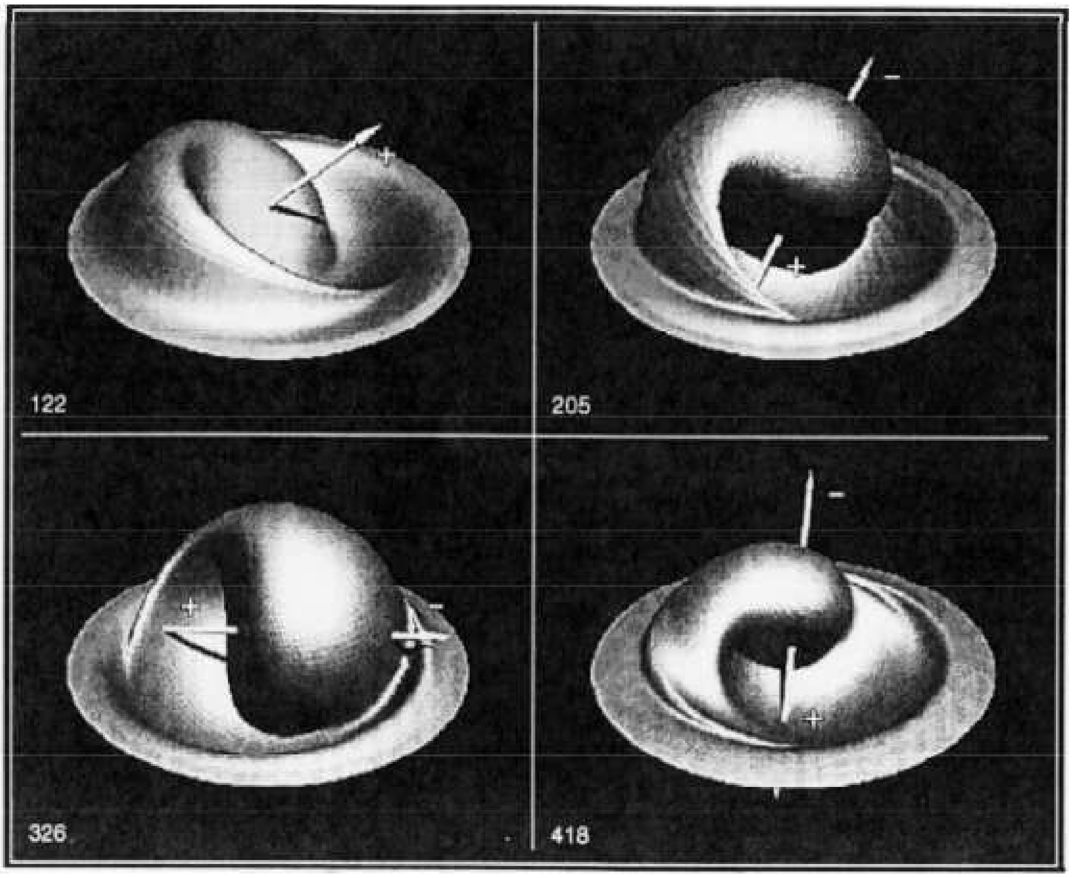

Figure 3.4: Time evolution of warped discs (Pringle, 1997). External illumination and logarithmic scale for radii are used such that the innermost radius $r = 1$ is at the origin ($\log r = 0$) and the outermost radius corresponds to $\log r = 4$. The time is shown on the left bottom corners in units of viscous time-scale.

tidal torque. The angular momentum equation for this case is

$$\dot{M}(GMR_{\mathrm{circ}})^{1/2} = \dot{M}(GMR_{*})^{1/2} + G_{\mathrm{tides}}. \tag{3.47}$$

The LHS of this equation is the rate angular momentum fed to the disc by the secondary star, the first term on the RHS is the rate of angular momentum at which the primary star accretes, and G_{tides} is the tidal torque required to be provided in order to compensate the difference between these two. Fig. 3.5 shows the result of a numerical calculation for the net effect of the tidal torque (Frank et al., 2002). Although the binary parameters determine the radius at which the tidal torque cut off the disc, R_{tides} is generally found to be

$$R_{\mathrm{tides}} \approx 0.9R_1, \tag{3.48}$$

where R_1 is the Roche lobe radius of the compact object.

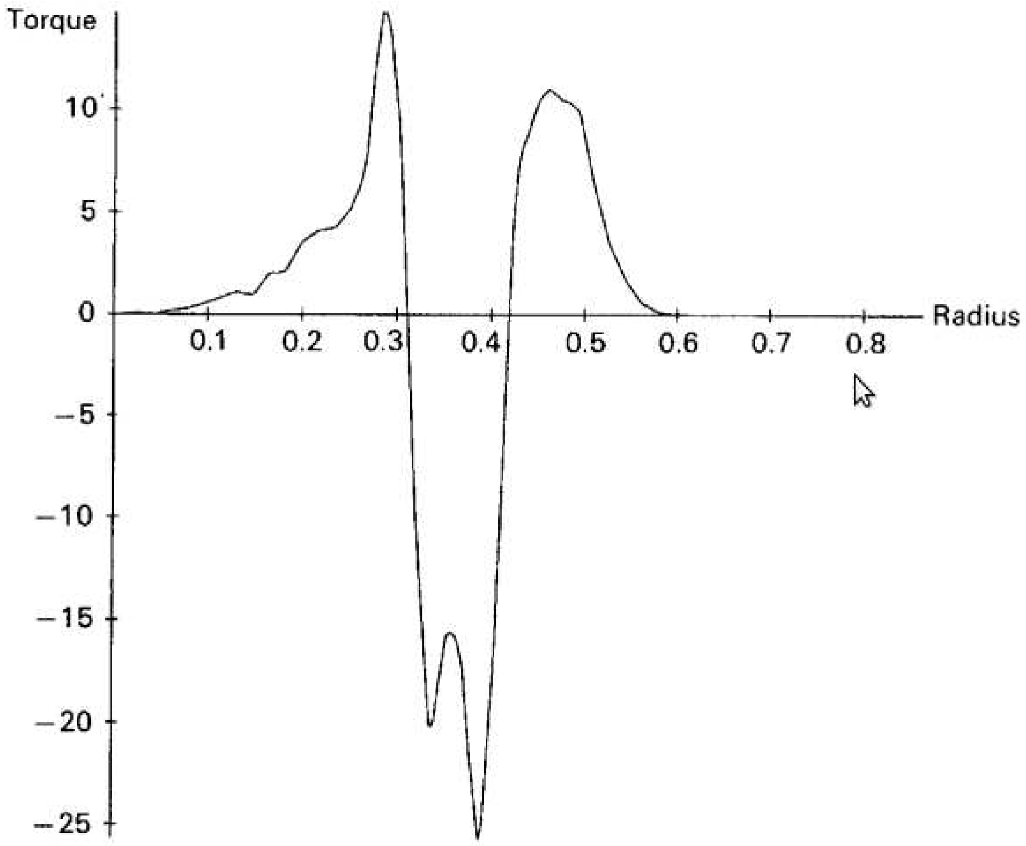

Figure 3.5: ”The average azimuthal torque. The disc is cut off at the tidal radius where the torque first changes sign. (Figure by Dr R. Whitehurst.)” (Frank et al., 2002)

’Resonance occurs when the frequency of radial motion of a particle in the disc is commensurate with the angular frequency of the secondary star as seen by the particle. This condition ensures that the particle will always receive a ’kick’ from the secondary at exactly the same phase of its radial motion, so allowing the cumulative effect of repeated kicks to build up and affect the motion significantly’ (Whitehurst and King, 1991). However, the radial and azimuthal motions of the particles in the disc are not always in phase owing to the tidal torques. Assuming the orbital angular and apsidal precession frequencies of the particle are Ω and ω, respectively, and the orbital period of the binary is $\Omega_{\rm orb}$, the frequency of radial motion (epicyclic frequency) of the particle is found to be $\Omega - \omega$. Since the particle sees the secondary star move with the angular frequency $\Omega - \Omega_{\rm orb}$, resonance is possible when

$$k(\Omega - \omega) = j(\Omega - \Omega_{\rm orb}) \tag{3.49}$$

where j and k are positive integers. ω can be neglected since the apsidal precession is

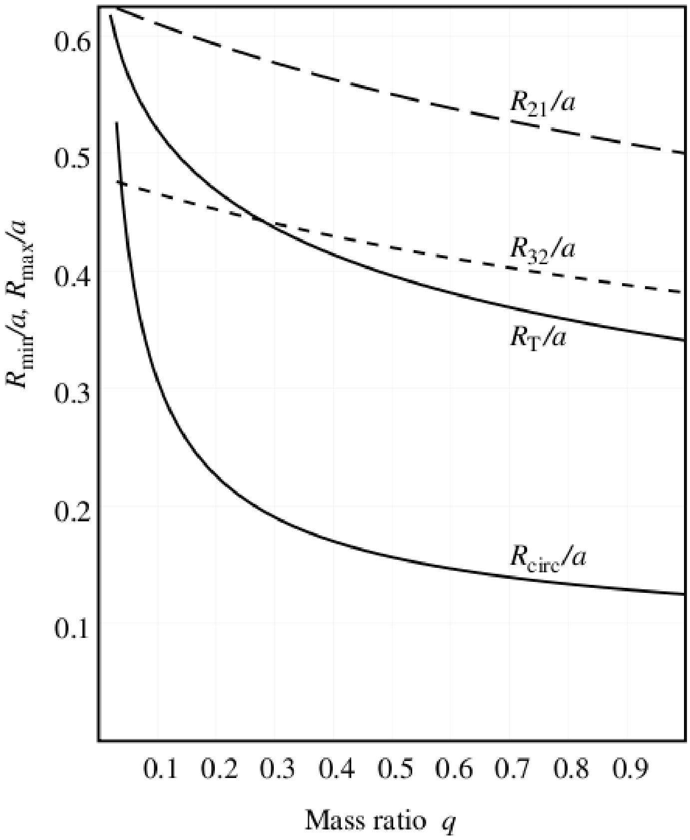

Figure 3.6: The solid curves are minimum (or circularization R_{circ}) radius and the maximum (or tidal R_T) radius for an accretion disc vs the mass ratio $q = M_2/M_1$. The dashed lines are the two most probable resonant radii R_{21} and R_{32}. Resonant orbits can only exist for small mass ratios q. (Frank et al., 2002)

much smaller than Ω and Ω_{orb}. Hence, resonances occur close to commensurabilities of the form $j : j - k$ between particle and binary frequencies. The eccentricity of an orbit directly affects the resonance: the growth rate of a resonance goes as e^k. Now, it is apparent that the strongest resonances originate at the $j : j - 1$ commensurabilities.

If the viscosity can perturb the disc orbits to extreme orbits, resonances destroy these orbits. Even quite aperiodic orbits are in Keplerian form, so the typical radii of resonant orbits near the $j : k$ commensurability is

$$R_{\mathrm{jk}} = \left[GM/\Omega_{\mathrm{jk}}^2\right]^{1/3}, \tag{3.50}$$

where Ω_{jk} is the value of Ω in the resonance condition (3.49). Using Kepler's third law $a = \left[G(M_1 + M_2)/\Omega_{\mathrm{orb}}^2\right]^{1/3}$, we obtain

$$\frac{R_{\mathrm{jk}}}{a} = \left(\frac{j-k}{j}\right)^{2/3} (1+q)^{-1/3}. \tag{3.51}$$

As shown in Fig. 3.6, mass ratio q and tidal radius R_T play an important role for the allowable resonances in the disc. It appears that the strongest resonance possible in the disc is that at $j = 3$ and $k = 2$. That is also compatible with observations and simulations which reveal that the particles in the precessing disc rim follow orbits very close to $P_{\mathrm{orb}}/3$.

CHAPTER 4

SOURCES

We selected some low mass and high mass X-ray binaries in order to see any possible effects of viscosity on the low frequency power density spectra of these sources. In addition, we studied the timing and spectral properties of the Be transient HMXB Swift 1626.6-5156, and the AXP source 1E 2259+586.

The selection criteria for the low mass and high mass X-ray binaries differ from each other, since these two groups do not resemble each other in many of their observational features.

The LMXBs were chosen according to the items listed below (Gilfanov and Arefiev, 2005)

(i) They are persistent, i.e. they do not show outbursts. Hence, their accretion disc was in the same state during the observation period.

(ii) Their orbital periods are known and rather long, $P_{\mathrm{orb}} \geq 10$ hours. The latter is necessary to minimize the aliasing effect.

(iii) Their average count rates exceed ≥ 2 cnt/sec.

(iv) Their signal to noise ratio at the orbital frequency is relatively high, $P_{\mathrm{signal}} \geq 10P_{\mathrm{noise}}$ in order to avoid the unaccounted systematic errors in the flux measurements of ASM.

GRS 1915+105, GX 13+1, Cir X-1, Cyg X-2, GX 349+2 and Sco X-1 are the LMXBs satisfying the required conditions.

We constructed our sample of HMXBs after evaluating the PDS of light curves for 45 high mass X-ray binaries with known orbital periods (Içdem and Baykal, 2011)

(i) We selected only persistent sources that are in the same state during the observation period. Twenty-five HMXRBs in our sample are Be transients that are not persistent X-ray sources and display outbursts because of the extremely wide eccentric orbit of neutron stars around their companions. Owing to the short outburst time span relative to the orbital period, we do not see breaks in their PDS. Outburst phases are the cause of substantial red noise in their PDS. Two sources Cen X-3 and Cyg X-1 have low frequency breaks in their PDS. However, these sources have significant signatures of high-low states in their light curves. These state transitions contaminate the long-term power density spectra, so that fake breaks may appear. To see these artificial effects, we carried out simulations as described in Chapter 5. In addition, we refer to Fig. 5.5 for the comparison between the PDS obtained from the real light curve and the simulated light curve. While creating the fake light curve, we took into account the state transitions of the source. Although we produced this light curve from a PDS obeying a power law trend (i.e. no breaks), it is clear from the figure that the simulated PDS resembles the real PDS. Hence, we estimate that the breaks in these sources are associated with the occurrence of high-low intensity states rather than the viscous time of the disc.

(ii) The sources with very low count rates, < 1 count/sec, such as LMC X-4 or 4U1538-52, have white-noise-dominated power density spectra at low frequencies.

(iii) In our analysis, we found that the remaining seven sources had low frequency breaks in their PDS together with power-law indices ~ 1.3. These are OAO 1657-415, SS 433, Vela X-1, SMC X-1, 4U 1700-377, GX 301-2, and LMC X-1. These values for α indices imply the existence of accretion discs (Lyubarskii, 1997). In Fig. 5.1,5.2 and Table 4.1 light curves and orbital parameters of the sources are presented, respectively.

The general properties of the sources we analysed in this thesis are mentioned in the following sections.

4.1 Low Mass X-ray Binaries

4.1.1 GRS 1915+105

The discovery of GRS 1915+105 was in 1992 by the WATCH instrument of the *Granat* satellite (Castro-Tirado et al., 1992). The optical companion is a low mass K-M III star (Greiner et al., 2001) and the compact object is a black hole with mass 14.0 ± 4.4 $M_\odot$, in a binary orbit of 33.5 days (Harlaftis and Greiner, 2004). GRS 1915+105 is a well-known microquasar since it is the first Galactic source to display superluminal motion (Mirabel and Rodríguez, 1994), and also it shows strong variability in its radio flux. It was found to have an unstable accretion disc which displays X-ray variability (Greiner et al., 1996). The binary attracts a great deal of attention by its superluminal jets that it ejects in its phase of relative radio-quiescence, which is thought to be 'jet-dominated' state with a $\sim$ 50 au scale inner radio jet (Fender et al., 2003; Dhawan et al., 2000).

4.1.2 GX 13+1

GX 13+1 is a persistent LMXB (Homan et al., 2004) that has rarely showed X-ray bursts (Fleischman, 1985; Matsuba et al., 1995) which indicates that the compact object in the system is a neutron star. Infrared spectral observations reveal that secondary star is a K5 giant (Bandyopadhyay et al., 1999) with a mass of 5 $M_\odot$ (Allen, 1973). The first mention of an X-ray halo around the binary was by Catura (1983) which is useful to determine limits on the dust grain density (Mathis et al., 1995) and the dust size distribution (Witt et al., 2001). The binary shows some periodic variation in its X-ray flux, such as the 57–69 Hz QPO discovered by Homan et al. (1998). There is also a long time periodic modulation of $\sim$ 24-day period which has been a controversial issue since it was considered to be due to the precession of the accretion disc; however, the discovery of the spectral type of the secondary led to the conclusion that the modulation is due to the orbital period rather than a quasi-periodic mechanism (Bandyopadhyay et al., 2002). Among the neutron star binary systems, iron K absorption lines was first discovered from GX 13+1 (Ueda et al., 2001).

4.1.3 Cir X-1

Cir X-1 was discovered in 1971 (Margon et al., 1971) and it is famous for its flares with a period of 16.55 days. These flares were observed in many regions of the electromagnetic spectrum: first in the X-ray band (Kaluzienski et al., 1976), then in the infrared (Glass, 1978, 1994), followed by radio (Haynes et al., 1978) and optical bands (Moneti, 1992). The flares are ascribed to intensive accretion near the periastron passage since the binary orbit is very eccentric, $e \sim 0.8$ (Murdin et al., 1980; Nicolson et al., 1980). Discovery of type-I X-ray bursts from the source (Tennant et al., 1986) was an indicative of the existence of a neutron star in the binary, which was reinforced by the detection of twin kHz QPOs in the X-ray power density spectra (Boutloukos et al., 2006). However, Cir X-1 exhibits some extraordinary properties such as black hole properties: jets on arcmin scale (Stewart et al., 1993; Tudose et al., 2006), radio loud luminosity (Whelan et al., 1977). The source shows also a hard X-ray emission (Iaria et al., 2001; Ding et al., 2003) and very strong X-ray variability (Jones et al., 1974; Samimi et al., 1979; Oosterbroek et al., 1995). On the other hand, the companion star has not been identified in all aspects yet.

4.1.4 Cyg X-2

’Cygnus X-2 is one of the brightest persistent low-mass X-ray binaries’ (Kuulkers et al., 1999). The compact object was determined to be a neutron star after the observations of the type-I X-ray bursts (Kahn and Grindlay, 1984; Kuulkers et al., 1995; Wijnands et al., 1996). The mass accretion rate from the secondary ($\dot{M} \sim 10^{18}$ g.s^{-1}) is considered to be near the Eddington limit (Smale, 1998). The binary period is $\sim$ 9.8 days (Cowley et al., 1979; Crampton and Cowley, 1980). Cyg X-2 also has been found to display kHz QPOs (Wijnands et al., 1998). The variations in the X-ray flux of Cyg X-2 are on very long time-scales, $\sim$ 78 days (Smale and Lochner, 1992; Wijnands et al., 1996). These variations may be due to the systematic changes in the position and shape of the Z track in the colour-colour and hardness-intensity graphs (Kuulkers et al., 1996; Wijnands et al., 1996, 1997). Nevertheless, there is not any agreement on the nature of these modulations.

4.1.5 GX 349+2

GX 349+2 (also known as Sco X-2) is also a bright X-ray source which has been studied mostly in X-rays (Schulz et al., 1989; Vrtilek et al., 1991; Ponman et al., 1988). Its companion was discovered by the help of is variable radio emission (Cooke and Ponman, 1991). Two simultaneous quasi-periodic oscillations were detected in the persistent flux of GX 349+2 at frequencies 712 and 978 Hz (Zhang et al., 1998). GX 349+2 is very similar to Sco X-1 in many respects. For example, their orbital periods are close, and both objects have been observed to show flaring behaviour. It differs from the other Z-sources in some of its observational features. Nevertheless, it is not observed very much; hence, it is poorly understood.

4.1.6 Sco X-1

Scorpius X-1 is the first extrasolar X-ray source to be discovered (Giacconi et al., 1962). It consists of a neutron star accreting from a Roche lobe-filling companion star. It is the brightest X-ray source in the sky. It has been observed in all energy bands since its discovery. The orbital period of the binary was found to be 18.9 hr (Gottlieb et al., 1975). As the other Z-sources, Sco X-1 also exhibits QPOs: three distinct types of QPOs have been reported, the near 6 Hz normal-branch oscillation (NBO), the near 45 Hz horizontal-branch oscillation (HBO) with a harmonic near 90 Hz, and the kilohertz quasi-periodic oscillations (kHz QPOs) (van der Klis et al., 1996, 1997). The secondary star of the binary was detected by the help of the determination of the radial velocities of the secondary and primary (Steeghs and Casares, 2002).

4.2 High Mass X-ray Binaries

4.2.1 Vela X-1

Vela X-1 is a very variable source which was detected in 1967 (Chodil et al., 1967). Eclipses of period $\sim$ 9 days were revealed by Ulmer et al. (1972) from periodic intensity variations. The optical companion of the pulsar, GP Vel/HD 77581 is a

B0.5 supergiant (Brucato and Kristian, 1972; Hiltner et al., 1972). The 283 s-X-ray pulse period was discovered from the data of *SAS-3* satellite (Rappaport and McClintock, 1975; McClintock et al., 1976). The eccentricity and orbital period were determined by Bildsten et al. (1997) very accurately: $e = 0.0898 \pm 0.0012$ and $P = 8.964368 \pm 0.000040$ d. The mass of the compact object can be estimated by predicting the mass of the optical companion. An early estimate for M_x was in 1974 by Zuiderwijk et al. (1974) as $M_x > 2.5M_\odot$, which indicates together with the lack of regular pulsations that the compact object is a black hole. After the detection of regular pulsations the masses of the companions were determined directly and the compact star was found to be a neutron star.

The 283-s X-ray pulsation period has been found to vary on all time-scales from days to years. These variations were described by a random walk in pulse frequency (Deeter et al., 1989) and they are explained as due to the fluctuations in the transfer of angular momentum by the wind accretion.

4.2.2 GX 301-2

GX 301-2 consists of a neutron star orbiting a B2 Iae star (WRA 977) which is an about 10^6-year old star. The system exhibits periodic X-ray pulsations of period ~ 700 s (White et al., 1976). The mass ratio of GX 301-2 is similar to that of Vela X-1, which is ~ 21.7. It has a highly eccentric orbit, $e \sim 0.467$ (Sato et al., 1986) with orbital period 41.5 days. The high eccentricity causes a large variation in the mass accretion rate onto the neutron star over the orbit and so the X-ray luminosity of the source changes in the range $(2 - 200) \times 10^{35}$ erg.s^{-1}, which is detected by a periodic outburst (Watson et al., 1982).

GX 301-2 is considered to be wind-accreting system. Using the hydrogen Balmer lines, a terminal wind velocity of ~ 400 km.s^{-1} was measured at a distance of $3R_c$ (R_c is the radius of the secondary) (Parkes et al., 1980).

The X-ray spectrum of the binary is highly affected from the high magnetic field of the pulsar. Hence, it is crucial to be informed about the magnetic field structure to understand the physics and the geometry of the accretion mechanism and the X-ray emission (Nagel, 1981; Meszaros and Nagel, 1985a,b; Araya and Harding, 1999; Araya-Góchez and Harding, 2000).

4.2.3 4U 1700-377

4U 1700-377 was first detected by the *Uhuru* satellite in 1973 and it is defined to be an X-ray eclipsing binary system with an orbital period of 3.4 days (Jones et al., 1973). The optical counterpart of the system is estimated as the luminous O6.5 Iaf star HD 153919. There has not been any X-ray periodicity detected other than that of the orbital period. In addition to this fact, the X-ray spectrum of the source is reported to be hard (Brown et al., 1996). These were interpreted as the compact object was a low mass black hole rather than a neutron star. The mass of the compact object of the system was estimated to be $\sim 2.44M_{\odot}$ and its X-ray spectrum resembles to those of accreting neutron stars (Clark et al., 2002). Due to these properties it is more common to refer to the compact companion as a neutron star, and account for the lack of pulsations as a result of "either a weak magnetic field or an alignment of the magnetic field with the spin axis" (Clark et al., 2002).

4.2.4 SMC X-1

SMC X-1 is a well-known accretion-powered high mass X-ray binary (Papaloizou, 1979). The system is composed of a neutron star of mass ~ 1.06 $\mathrm{M}_{\odot}$ (van der Meer et al., 2007) having spin period of 0.71 s (Lucke et al., 1976). The accreted material is sustained by the B0I star Sk 160 of mass ~ 17.2 $\mathrm{M}_{\odot}$ (Reynolds et al., 1993). It is significant by being the only HMXB with a supergiant companion in Small Magellanic Cloud (SMC) so far (Galache et al., 2008).

SMC X-1 is one of the most powerful X-ray pulsars and is the only X-ray pulsar displaying evidence of steady spin-up (Wojdowski et al., 1998) with an orbital decay of $P_{\mathrm{orb}}/\dot{P}_{\mathrm{orb}} \sim 3.4 \times 10^{-6}$ yr^{-1} (Levine et al., 1993; Wojdowski et al., 1998). It also displays a super-orbital X-ray flux variations of on average ~ 55 days unlike the 35-day cycle of Her X-1, length of even adjacent super-orbital cycles are highly variable. This super-orbital period is assumed to be arising due to the precession of a warped disc (Wojdowski et al., 1998; Trowbridge et al., 2007).

4.2.5 OAO 1657-415

OAO 1657-415 is another accreting pulsar which was first discovered with the *Copernicus* satellite (Polidan et al., 1978). Although the pulse period of 38.22 s was detected just after its discovery (White and Pravdo, 1979), it was not until 1993 that the binary orbit and the eclipsing nature of the system were discovered (Chakrabarty et al., 1993). It is difficult to identify an optical counterpart; however, an infrared counterpart was found by Chakrabarty et al. (2002), which is considered to be a highly reddened B supergiant. Since its discovery, the pulsar was found to exhibit a long-term spin-up from 38.218 s (White and Pravdo, 1979) to 37.329 s (Chakrabarty et al., 2002), including some spin-down intervals (Bildsten et al., 1997). There have been some models to account for these spin-up and spin-down trends of the source: formation of episodic accretion discs from stellar wind accretion (Baykal, 1997), spin-down of the rapidly rotating magnetised pulsar by accretion from a disc triggered by the magnetic, propeller driven outflows (Lovelace et al., 1999).

4.2.6 SS 433

SS 433 is a very famous object since it is the first microquasar discovered in our Galaxy (Margon, 1984). Many observations have been carried out in all energy bands for more than 30 years. It is a high-luminosity massive X-ray binary system showing signs of a precessing accretion disc of period 162.5 day and related jets (Margon, 1984; Fabrika, 2004). Te compact object is probably a black hole accreting material from its late A-supergiant companion (Gies et al., 2002; Hillwig et al., 2004; Cherepashchuk et al., 2003, 2005) at very high super-Eddington rate.

There are several periodicities detected related to the system: the precessional one ($\sim$ 162 days), the orbital one (13.08 days) and the nutational one (6.28 days) (Cherepashchuk, 2002). These periodic variations have been well studied to determine some of the system's parameters such as the inclination angle and the jet precession angle (Eikenberry et al., 2001; Collins and Scher, 2002). In spite of the interest in the system, there are still a lot of questions to be answered regarding the nature of the compact object and masses of the companions. With a simple search in the literature, one can easily see that there is a large variation in the mass estimates of the companions and their mass ratio, q. It is considered to be a black hole candidate having a Roche-lobe-overflow-powered accretion disc similar to the low mass X-ray binaries (Begelman et al., 2006).

4.2.7 LMC X-1

LMC X-1 is the first persistently luminous X-ray source discovered in the Large Magellanic Cloud (Mark et al., 1969). The first estimates for the orbital period and the mass of the compact object were $\sim$ 4 days and $\sim$ 6 $M_{\odot}$, respectively (Hutchings et al., 1983, 1987). These made LMC X-1 the fourth dynamical black hole candidate. More accurate estimates for the orbital period were not until 2006, by Levine and Corbet (2006) using the X-ray data of *RXTE*. Similarly, the optical counterpart was determined as an O7/O8 giant identified as ”star 32” by Cowley et al. (1978); Cui et al. (2002). Orosz et al. (2009), in their recent analysis , found accurate values for the masses of the companions, the inclination angle, orbital period (see Table 4.1 for the values) by constructing a dynamical model for the system from their analysis of the optical and near-infrared data obtained by the ANDICAM instrument on the 1.3-m telescope at CTIO, (which is operated by the Small and Moderate Aperture Research Telescope System, SMARTS, consortium) and the Magellan Inamori Kyocera Echelle (MIKE) spectrograph (Bernstein et al., 2003) and the 6.5-m Magellan Clay telescope at LCO, together with X-ray data of *RXTE*-ASM.

4.2.8 SWIFT J1626.6−5156

Swift J1626.6−5156 was discovered on 2005 December 18 with the *Swift* Burst Alert Telescope (BAT) (Palmer et al., 2005) when it became detectable owing to its outburst. Being a transient and accretion powered neutron star, the pulsar was determined to have a spin period of $\sim$ 15 s (Palmer et al., 2005; Markwardt and Swank, 2005). The source was observed to emit two X-ray flares shortly after its 2005 outburst, which continued for $\sim$ 450 s and increased the pulsed fraction increased up to $\sim$ 70% (Reig et al., 2008). The average count rate and the pulsed fraction of the source recovered very quickly to their pre-flare values after the flares. The source was reported to possess a weak QPO at a characteristic frequency of 1 Hz with a fractional rms of 4.7% (Reig et al., 2008).

The optical companion of the pulsar, 2MASS16263652-5156305, USNO-B1.0 0380-0649488, is considered to be a Be star because of its strong Hα emission (Negueruela and Marco, 2006); however, it is usually faint in infrared band, which is unusual for Be stars.

Baykal et al. (2010) studied long term monitoring *RXTE*-PCA observations of this new source belonging to the time interval 53724 - 54410 MJD. ”They obtained timing solution of the source and found the orbital period to be 132.89 days. They also constructed long term pulse frequency history of Swift J1626.6−5156 and showed that the time-scale of the X-ray modulations varied, which led to earlier suggestions (Reig et al., 2008; Decesar et al., 2009) of orbital periods at about a third and half of the orbital period of Swift J1626.6-5156.” (Icdem et al., 2011b).

4.3 Anomalous X-ray Pulsar

4.3.1 1E 2259+586

The anomalous X-ray pulsar (AXP) 1E 2259+586 was discovered by Fahlman and Gregory (1981) within the supernova remnant G109.1-1.0 exhibiting 7 s pulsations. It has been spinning-down for more than 10 years with an average spin-down rate $\dot{\nu} \sim 1.0 \times 10^{-14}$ Hz.s^{-1} (Iwasawa et al., 1992). Baykal and Swank (1996) found a marginal spin-up episode between 1991 and 1992 analysing the data of *ROSAT*.

”1E 2259+586 drew attention by its outburst in June 2002 consisting of over 80 short SGR-like bursts (Gavriil et al., 2004). During this outburst, flux level of the source increased by a factor of more than 20 accompanied with a glitch (sudden change in the spin frequency and/or the spin down rate) of fractional frequency change $\frac{\nu}{\nu} \sim 4.24 \times 10^{-6}$ (Kaspi et al., 2003; Woods et al., 2004).” (Icdem et al., 2011a). In 2007, a second glitch of $\frac{\Delta\nu}{\nu} \sim 8.5 \times 10^{-7}$ was detected but this time without any bursts (Dib et al., 2008).

The near- and mid-infrared observations with *Spitzer Space Telescope* might point out to the existence of a passive X-ray-heated dust disc (Kaplan et al., 2009). The distance to the AXP (and also to the SNR G109.1-1.0) was estimated to be 4.0 ± 0.8 kpc using the 21-cm H I-line and CO-line spectra of the SNR G109.1-1.0, H II region Sh 152, and the adjacent molecular cloud complex (Tian et al., 2010).

The 2002 glitch of the source was analysed in great detail by Woods et al. (2004) using the observations of *XMM* and *RXTE* satellites. Using their results, they ”concluded that the pulsar experienced something which was not sudden at all and included two components, one of them was on the surface and the other distributed over a wider region. Hence, both the superfluid interior and the magnetosphere were affected.”

Table 4.1: The binary parameters for LMXBs and HMXBs.

Source	$M_1(M_\odot)$	$M_2(M_\odot)$	$P_{\rm orb}(days)$	$a(10^{10}{\rm cm})$	q	D(kpc)	$Ref.$
Low Mass X-ray Binaries							
GRS1915+105	14.0 ± 4.4	0.81 ± 0.53	33.5 ± 1.5	747 ± 78	0.058 ± 0.033	12.1 ± 0.8	Harlaftis and Greiner (2004),Fender et al. (1999)
GX13+1	1.4	5 ± 1	24.7	461 ± 25	3.6 ± 0.9	7 ± 1	Bandyopadhyay et al. (1999)
Cir X-1	1.4	4 ± 1	16.6	334 ± 21	2.9 ± 0.8	5.5	Johnston et al. (1999)
Cyg X-2	1.78 ± 0.23	0.60 ± 0.13	9.85	180 ± 7	0.34 ± 0.04	7.2 ± 1.1	Orosz and Kuulkers (1999)
GX349+2	1.4	1.5 ± 1	0.938 ± 0.004	40.0 ± 4.7	1.07 ± 0.73	9.2	Wachter and Margon (1996)
Sco X-1	1.4	0.42	0.79	30.5 ± 1.1	0.30 ± 0.05	2.8 ± 0.3	Steeghs and Casares (2002)
High Mass X-ray Binaries							
OAO1657-415	$1.4 - 4.0$	14-18	10.4436	$106.0/\sin(i)$	4.5-10	6.4 ± 1.2 Chakrabarty et al. (2002)	Chakrabarty et al. (1993)
SS433	~ 9	~ 30	13.082	740	~ 3.33	5	Cherepashchuk et al. (2005)
Vela X-1	2.27 ± 0.17	27.9 ± 1.3	8.964368	410.4	12.29 ± 0.35	1.9 ± 0.2 Sadakane et al. (1985)	Quaintrell et al. (2003)
	1.88 ± 0.13	23.1 ± 0.2		341.9	12.29 ± 0.74		
GX 301-2	1.85 ± 0.6	39-53	41.5		21.74 ± 6.62	$3 - 4$	Kaper et al. (2006)
SMC X-1	1.06 ± 0.1	17.2 ± 0.6	3.8923		16.23 ± 2.10	61	van der Meer et al. (2007)
LMC X-1	10.91 ± 1.41	31.79 ± 3.48	3.90917		2.91 ± 0.70	~ 50	Orosz et al. (2009)
4U 1700-377	2.44 ± 0.27	58 ± 11	3.412		23.77 ± 7.14	1.8	Clark et al. (2002)

Notes. M_1 and M_2 are masses of the primary and secondary companions, respectively. $P_{\rm orb}$ is the orbital period, a is the binary separation, q is the mass ratio M_1/M_2 and D is the distance of the system. The two sets of parameters for Vela X-1 correspond to inclination angles $i = 70.1$ deg and 90 deg, respectively. $Ref.$ refers to References for the parameters.

CHAPTER 5

VISCOUS TIME-SCALE in X-RAY BINARIES

5.1 *RXTE* Observations

We used data gathered by the All Sky Monitor (ASM) instrument of *Rossi X-ray Timing Explorer* (*RXTE*) observatory, covering the period from 1996 to 2010. The ASM instrument operates in the 2–12 keV energy range with its position sensitive Xenon proportional counter, performs flux measurements for over ~ 500 X-ray sources, and scans 80% of the sky every 90 minutes. Each flux measurement has a duration of ~ 90 seconds. Some gaps sometimes appear in time as long as a few months in the light curves of ASM sources because of navigational constrains and the appearance of very bright transient sources. The dwell-by-dwell light curves were retrieved from the public *RXTE*-ASM archive at HEASARC.

We derived the power density spectra (PDS) of the sources from the cosine transform of the discrete autocorrelation function (see Section 5.2 for a detailed explanation). We also estimated the PDS using HEASARC software ’powspec’ with Miyamoto normalization (Miyamoto et al., 1992) in our data analysis. Both estimations of PDS give consistent results.

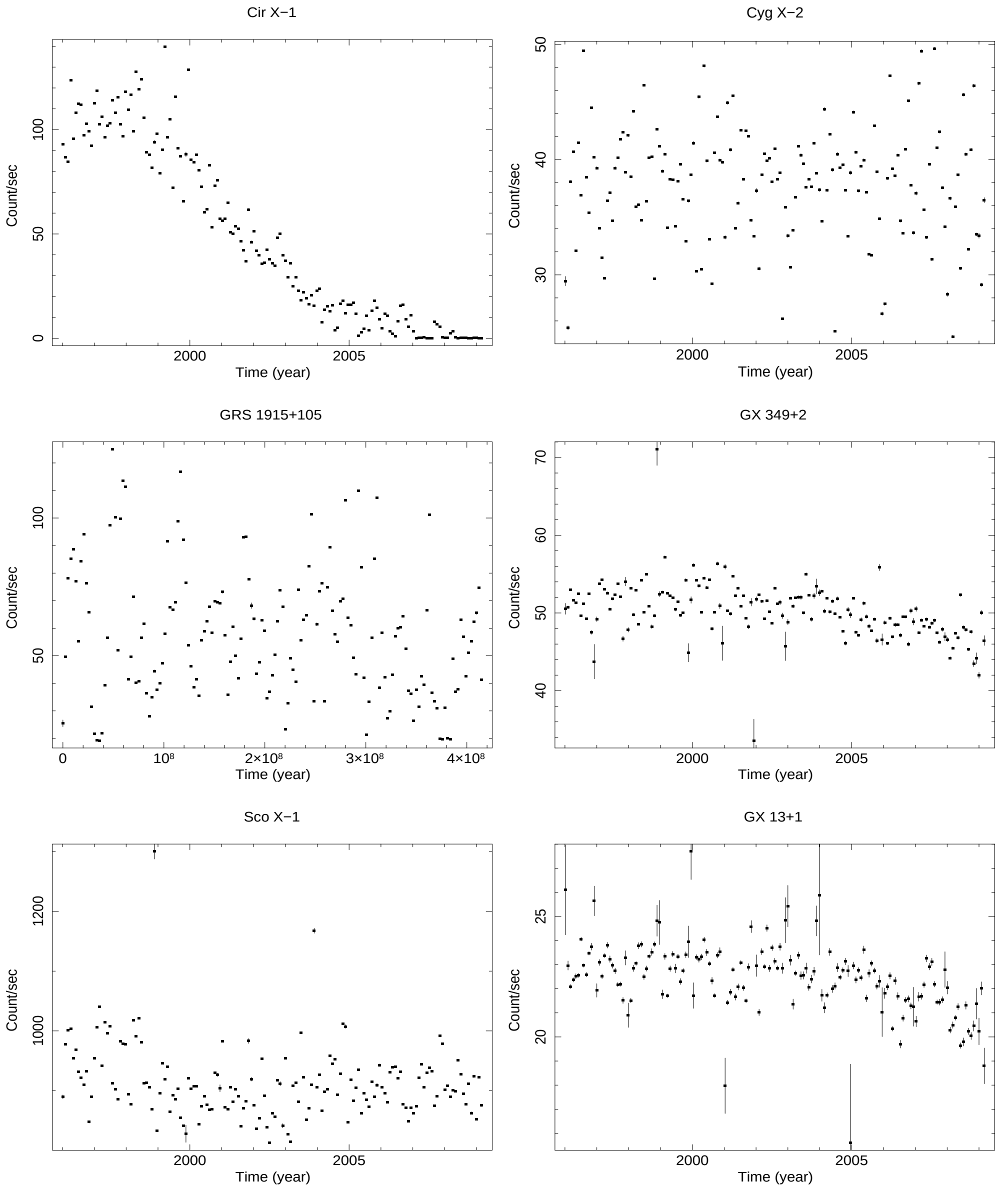

Figure 5.1: Long-term light curves of the low-mass X-ray binaries

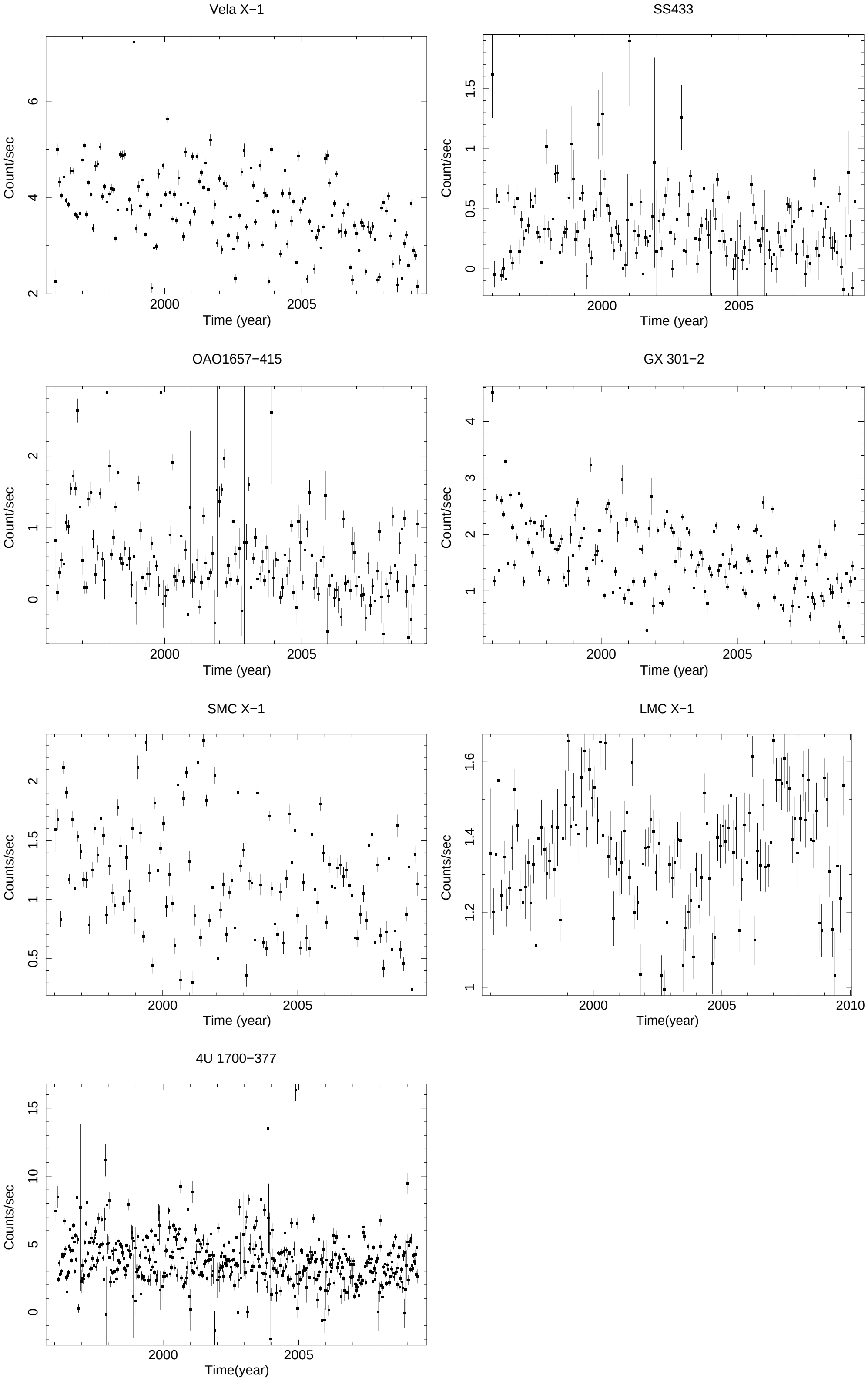

Figure 5.2: Long-term light curves of the high-mass X-ray binaries

5.2 Generation of Power Density Spectrum

Power density spectrum is a useful tool to evaluate how the power of a signal or time series is distributed with frequency; hence, it enables us to reveal repeating patterns hiding in a random signal. There are several methods to obtain a power density spectrum from a signal, like the Fourier transform, Welch's method or the maximum entropy method. Among these, the Fourier transform technique is the most common one.

Using the Fourier transform, we decompose the signal into sine functions. For a time dependent function $x(t)$, an array of different cosine functions with specific frequencies ω_j can be added together with an amplitude a_j , and phase ϕ_j

$$x(t) = \frac{1}{N}\sum_j a_j \cos(\omega_j t - \phi_j) = \frac{1}{N}\sum_j [A_j \cos\omega_j t + B_j \sin\omega_j t] \tag{5.1}$$

where the amplitudes are calculated using $x_k = x(t_k)$ as

$$A_j = \sum_{k=0}^{N-1} x_k \cos\omega_j t \tag{5.2}$$

$$B_j = \sum_{k=0}^{N-1} x_k \sin\omega_j t. \tag{5.3}$$

These can also be written in terms of complex numbers:

$$a_j = \sum_{k=0}^{N-1} x_k \mathrm{e}^{i\omega_j t_k} \tag{5.4}$$

$$x_k = \frac{1}{N}\sum_{j=-N/2}^{N/2-1} a_j \mathrm{e}^{-i\omega_j t_k} \tag{5.5}$$

where a_j are complex Fourier amplitudes which are Fourier transforms of the signal x_k. This notation can also be used for a discrete series of signals with N bins. In this case, if the differential time step is $\delta t = T/N$ and the time series is composed of number of photons detected in equally spaced time intervals, i.e. x_k is the data for the k-th time bin of interval $t = (k-1)\Delta t : k\Delta t$, where k runs from 0 to $N-1$, then the frequency counterpart is $\omega_j = 2\pi j/T$, where j and k are $j = -\frac{N}{2}, ..., \frac{N}{2} - 1$,

$k = 0, ..., N - 1$. Hence, the discrete Fourier transform of the time series is given by

$$a_j = \sum_{k=0}^{N-1} x_k \mathrm{e}^{2\pi ijk/N}, \quad j = -\frac{N}{2}, ..., \frac{N}{2} - 1 \tag{5.6}$$

$$x_k = \frac{1}{N} \sum_{j=N/2}^{N/2-1} a_j \mathrm{e}^{-2\pi ijk}, \quad k = 0, ..., N - 1. \tag{5.7}$$

The total number of photons is given by the 0-th amplitude, i.e. $a_0 = \sum\limits_{k}^{N-1} x_k$. There is an important theorem called Parseval's theorem which states that

$$\sum_{k=0}^{N-1} |x_k|^2 = \frac{1}{N} \sum_{j=-N/2}^{N/2-1} |a_j|^2. \tag{5.8}$$

This theorem is useful to define the 'power' of the signal at a specific frequency. For example, Leahy normalization is defined based on the variance of the count data, since $\mathrm{Var}(x_k) \equiv \sum_k (x_k - \overline{x})^2 = \sum_k x_k^2 - \frac{1}{N} \left(\sum_k x_k\right)^2 = \frac{1}{N} \sum_j |a_j|^2 - \frac{1}{N} a_0^2$, as (Leahy et al., 1983)

$$P_j \equiv \frac{2}{N_{\mathrm{ph}}} |a_j|^2 \quad j = 0, ..., N/2 \tag{5.9}$$

where $N_{\mathrm{ph}} = \sum\limits_{k=0}^{N-1} x_k$ is the total number of counts in the time series, and we used the fact that for real data $|a_j| = |a_{-j}|$. There is also another type of normalization, where power is defined as rms^2/Hz (Miyamoto et al., 1992). According to Miyamoto normalization, the power density in the j-th frequency bin, which is centred at frequency $f_j = j/T$ Hz, expressed in units of rms^2/Hz equals

$$P_j = \frac{2|\hat{x}_j|^2}{N_{\mathrm{ph}}} \frac{1}{\langle r \rangle} = \frac{2|\hat{x}_j|^2}{\langle r \rangle^2 T} \tag{5.10}$$

where $T = N\Delta t$ is its total duration and $\langle r \rangle = N_{\mathrm{ph}}/T$ is the average count rate. One advantage of the Miyamoto normalized power spectrum is that its integral directly gives the squared rms fractional variability provided that the expected (white) noise level is subtracted.

There is an alternative way to obtain the power spectrum which is known as the Wiener-Khinchin theorem. According to this theorem the power spectral density of a wide-sense-stationary random process is the Fourier transform of the corresponding auto-correlation function. The advantage of using the auto-correlation function is that it enables us to work with unequally sampled data.

We obtained the power density spectra (PDS) of the sources by the method based on the discrete auto-correlation function (Edelson and Krolik, 1988), which is the method used by Gilfanov and Arefiev (2005) for their calculations (we used their FORTRAN code with some minor changes). We determined the power of the signal at each frequency using

$$P_j = \frac{2}{\langle r \rangle^2 T}\left(A_0 N + 2\sum_{l=0}^{N-1}(N-l)\langle A_l \rangle \cos\frac{2\pi jl}{N} \right) \tag{5.11}$$

where $\langle A_l \rangle = \langle x_k x_{k+l} \rangle$ is the discrete auto-correlation function. The noise level in the power density spectrum equals, where σ_k is the error in the measurement of x_k

$$P_{\rm noise} = 2\frac{\sum_{k=0}^{N-1}\sigma_k^2}{\langle r \rangle^2 T}. \tag{5.12}$$

5.3 Power Density Spectra

The viscous time scale is the longest time-scale of an accretion disc, which has the meaning that perturbations with longer time-scales are not correlated with each other, rather their frequency counterparts appear in the power density spectra as a ’white noise’ structure. On the other hand, modulations with shorter time-scales are considered to have a relation, which make it possible to model their power density-frequency curves by a power law: $P \sim \nu^{-\alpha}$ where $\alpha \sim 1$. The slope being ~ 1 is the result of the fact that the total X-ray flux is contributed by the whole accretion disc at every radius, i.e. any α-parameter fluctuation at radius r has an effect on the total accretion rate, and so flux, at the frequency $\nu \sim 1/t_{\rm visc}(r)$ as demonstrated by Lyubarskii (1997) and stated by Gilfanov and Arefiev (2005).

We stated that our main aim in this study is to relate the break frequency of X-ray binaries, i.e. the transition frequency from white noise to red noise in the power density spectrum, with the viscous time-scale. One practical way to interpret analysis results is to compare the theoretical ratio $f_{\rm visc}/f_{\rm orb}$ to the observational ratio $f_{\rm break}/f_{\rm orb}$. In accordance with this purpose, we generated the PDS of the long term ASM light curves of our sources by the method described in 5.2. These PDS are geometrically binned so that the broken power law trend can be seen easily. The point of interests are the break frequencies and the power law indices after those frequencies; hence, the PDS were modelled by broken power laws. The PDS with the best-fitting models, and the deduced parameters are given in Figs. 5.4 and 5.3, and Table 5.1, respectively. The orbital and super-orbital periods of the sources are displayed on the power density spectra by dashed lines. ”Although these modulations are quite clear as peaks at the corresponding frequencies, it is not possible to determine their values from the PDS accurately since we use geometrical binning and the resolutions of the PDS are low” (Içdem and Baykal, 2011).

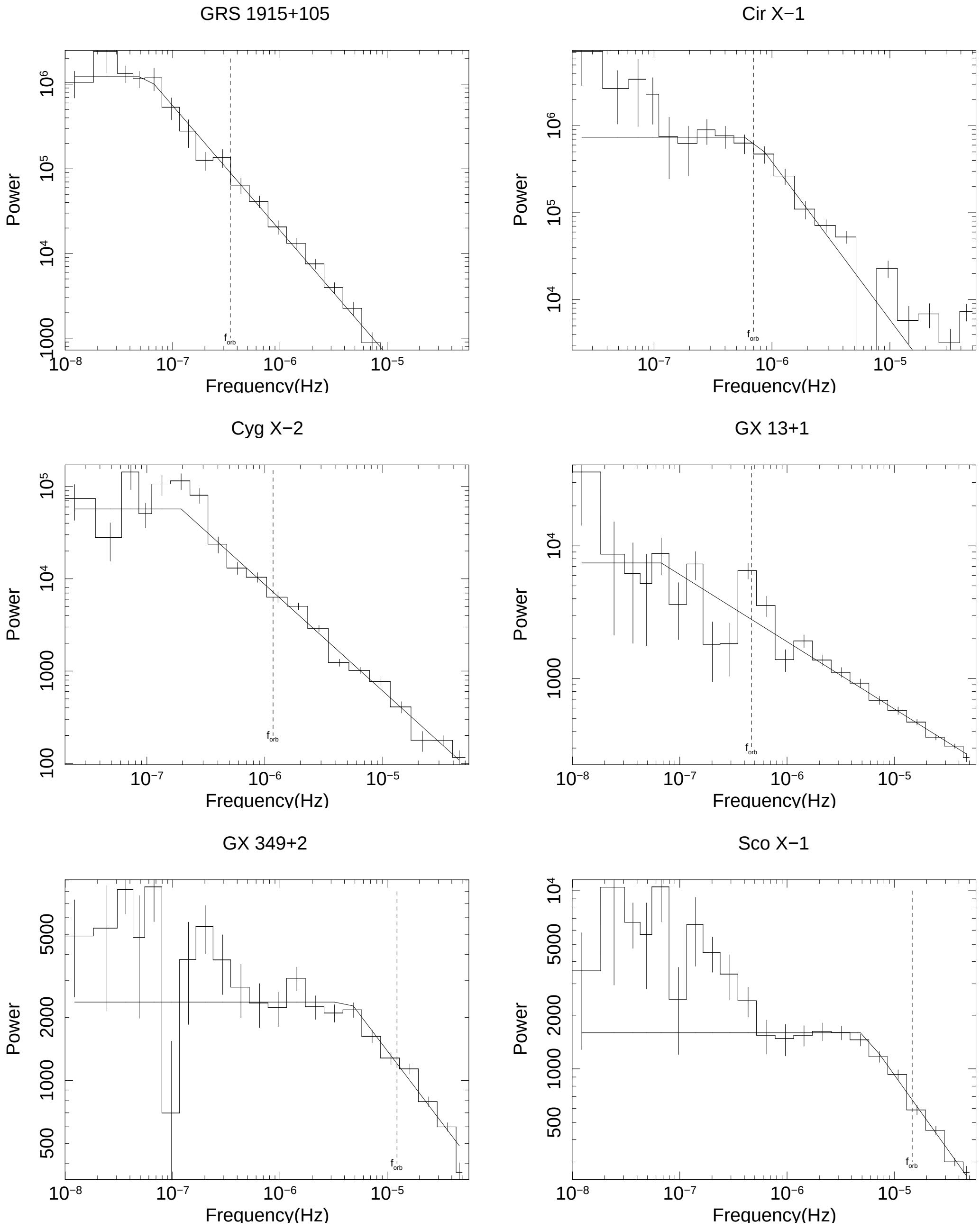

Figure 5.3: Power density spectra of low mass X-ray binaries with best power law models

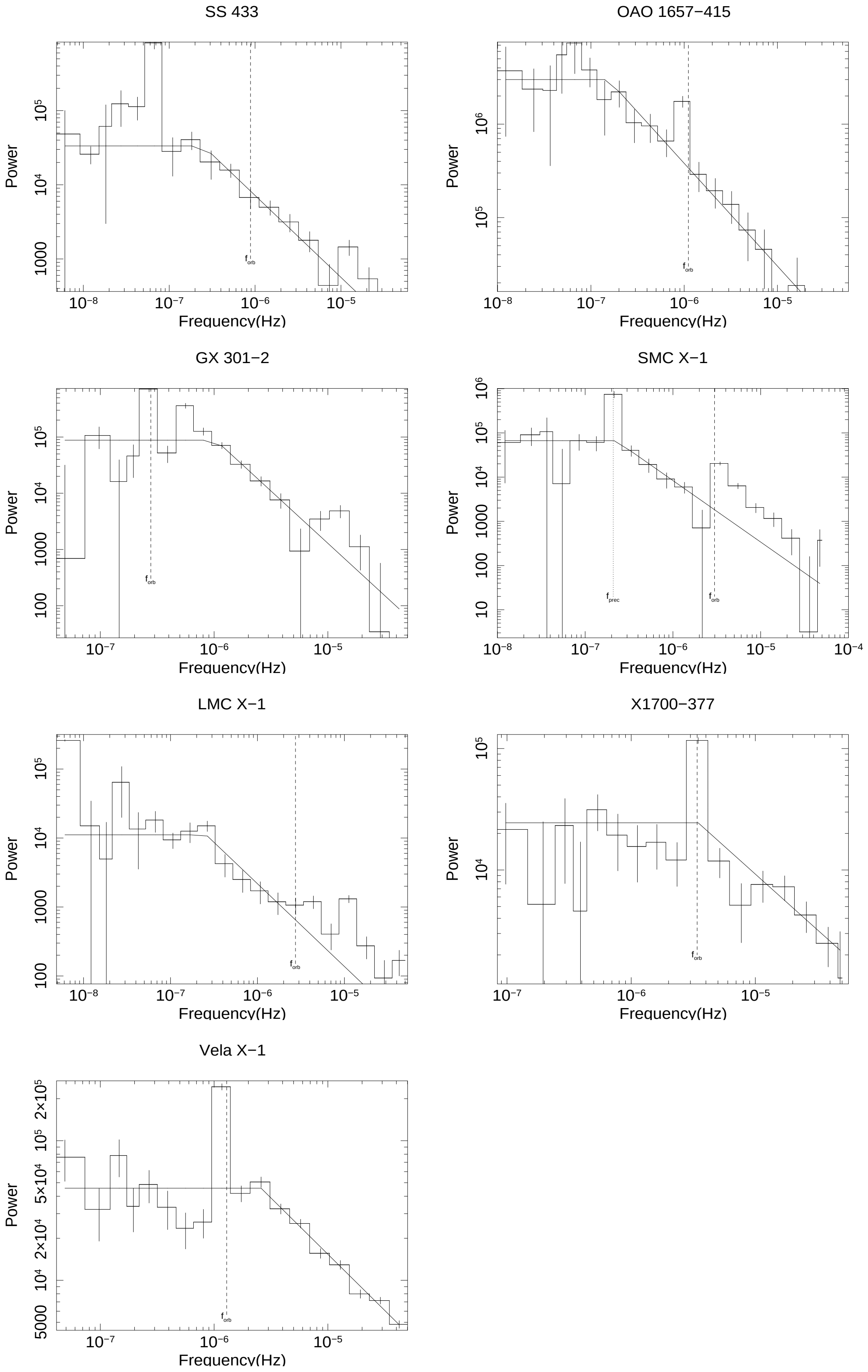

Figure 5.4: Power density spectra of high mass X-ray binaries with the best power-law models and AXP 1E 2259+586

Table 5.1: The parameters of power spectra approximation.

Source	(cnts/sec)	$L_x (10^{37}$ ergs/s)	f_{break} (Hz)	α	f_{range} (Hz)	f_{break} / f_{orb}	Gilfanov and Arefiev (2005)'s Results	
							f_{break} (Hz)	α
Low Mass X-ray Binaries								
GRS1915+105	58.99	33	$5.85^{+0.82}_{-0.41} \times 10^{-8}$	1.47 ± 0.04	$1 \times 10^{-8} - 1 \times 10^{-5}$	0.17	$6.50^{+2.68}_{-1.64} \times 10^{-8}$	$1.26^{+0.18}_{-0.11}$
GX13+1	22.46	4.2	$6.71 \pm 0.47 \times 10^{-8}$	0.51 ± 0.01	$1 \times 10^{-8} - 4 \times 10^{-5}$	0.14	$1.13 \pm 0.25 \times 10^{-7}$	0.56 ± 0.3
Cir X-1	108.11	12.5	$6.99^{+0.56}_{-0.63} \times 10^{-7}$	$1.82^{+0.13}_{-0.12}$	$1 \times 10^{-8} - 4 \times 10^{-5}$	0.17	$1.14^{+0.12}_{-0.18} \times 10^{-6}$	1.51 ± 0.13
Cyg X-2	38.5	7.6	$1.95 \pm 0.10 \times 10^{-7}$	1.15 ± 0.02	$2 \times 10^{-8} - 4 \times 10^{-5}$	0.17	$3.66^{+0.36}_{-1.47} \times 10^{-7}$	1.13 ± 0.09
GX349+2	50.82	16.4	$4.53 \pm 0.27 \times 10^{-6}$	0.68 ± 0.27	$2 \times 10^{-8} - 4 \times 10^{-5}$	0.37	$2.78^{+0.63}_{-0.92} \times 10^{-6}$	0.66 ± 0.06
Sco X-1	915.45	27.4	$5.24 \pm 0.26 \times 10^{-6}$	0.83 ± 0.34	$1 \times 10^{-8} - 4 \times 10^{-5}$	0.36	$6.14^{+1.06}_{-0.71} \times 10^{-6}$	$0.89^{+0.10}_{-0.06}$
High Mass X-ray Binaries								
OAO1657-415	2.25	0.3	$1.74^{+0.30}_{-0.30} \times 10^{-7}$	$1.15^{+0.12}_{-0.09}$	$2 \times 10^{-8} - 4 \times 10^{-5}$	$0.157^{+0.027}_{-0.027}$	–	–
SS 433	1.53	0.1	$4.59^{+0.83}_{-0.83} \times 10^{-8}$	$1.22^{+0.11}_{-0.09}$	$2 \times 10^{-8} - 4 \times 10^{-5}$	$0.052^{0.009}_{-0.009}$	–	–
Vela X-1	5.00	0.4	$3.30^{+0.18}_{-0.20} \times 10^{-6}$	$0.81^{+0.03}_{-0.03}$	$2 \times 10^{-8} - 4 \times 10^{-5}$	$2.556^{+0.155}_{-0.155}$	–	–
GX 301-2	1.58	0.8 – 2.0	$1.03^{+0.17}_{-0.16} \times 10^{-6}$	$1.86^{+0.30}_{-0.25}$	$4 \times 10^{-8} - 4 \times 10^{-5}$	$1.47^{+0.22}_{-0.22}$	–	–
LMC X-1	1.36	~ 23	$2.57^{+0.42}_{-1.01} \times 10^{-7}$	$1.20^{+0.31}_{-0.31}$	$5 \times 10^{-9} - 4 \times 10^{-5}$	$0.087^{+0.015}_{-0.034}$	–	–
SMC X-1	1.22	55	$2.25^{+0.9}_{-0.9} \times 10^{-7}$	$1.39^{+0.45}_{-0.45}$	$1 \times 10^{-8} - 4 \times 10^{-5}$	$0.076^{+0.036}_{-0.024}$	–	–
4U 1700-377	3.83	~ 0.1	$2.58^{+0.43}_{-0.35} \times 10^{-6}$	$0.83^{+0.16}_{-0.12}$	$8 \times 10^{-8} - 4 \times 10^{-5}$	$0.76^{+0.13}_{-0.10}$	–	–

Notes. L_x is the X-ray luminosity calculated using respective count rates and source distances listed in Table 4.1. α is appropriate power law slope. The last two column contain the findings of Gilfanov and Arefiev (2005) for low mass X-ray binary sources.

There are some periodic modulations in the X-ray flux of the sources as clearly seen in the power spectra with apparent peaks. These may be caused by the orbital motion of the system or the quasi-periodic/periodic modulation due to the precession of accretion disc, etc. Since these distort the normal trend of the PDS, it comes to mind whether the existence or the position of the breaks are affected by these modulations. To solve this problem, we carried out simulations using the orbital period and precession periods of each source. The procedure for the simulations is as follows: ”We took Fourier amplitudes from the real power spectra, and for the phases of Fourier amplitudes, we used Gaussian white noise with unit variance. We sampled the light curves of each source as if observed by ASM such that their power densities are consistent with the power law $P \sim f^{-1.3}$. We then convolved these time series by introducing periodic signals for both the orbital motion and precession period if the source had a periodicity. Consequently, using the simulated light curves we constructed the power density spectrum.” (Içdem and Baykal, 2011) Eventually, no breaks appeared due to orbital or precession modulation of light curves. As an example, the simulation results of Vela X-1 are presented in Fig.5.5.

There are also some other short-term variations, like magnetic field effects on the inner disc and flickering, but those are detected at high frequencies, i.e. higher than our Nyquist frequency $> 1.0 \times 10^{-4}$ Hz, so they do not ’pollute’ the low frequency power density spectra we analyse.

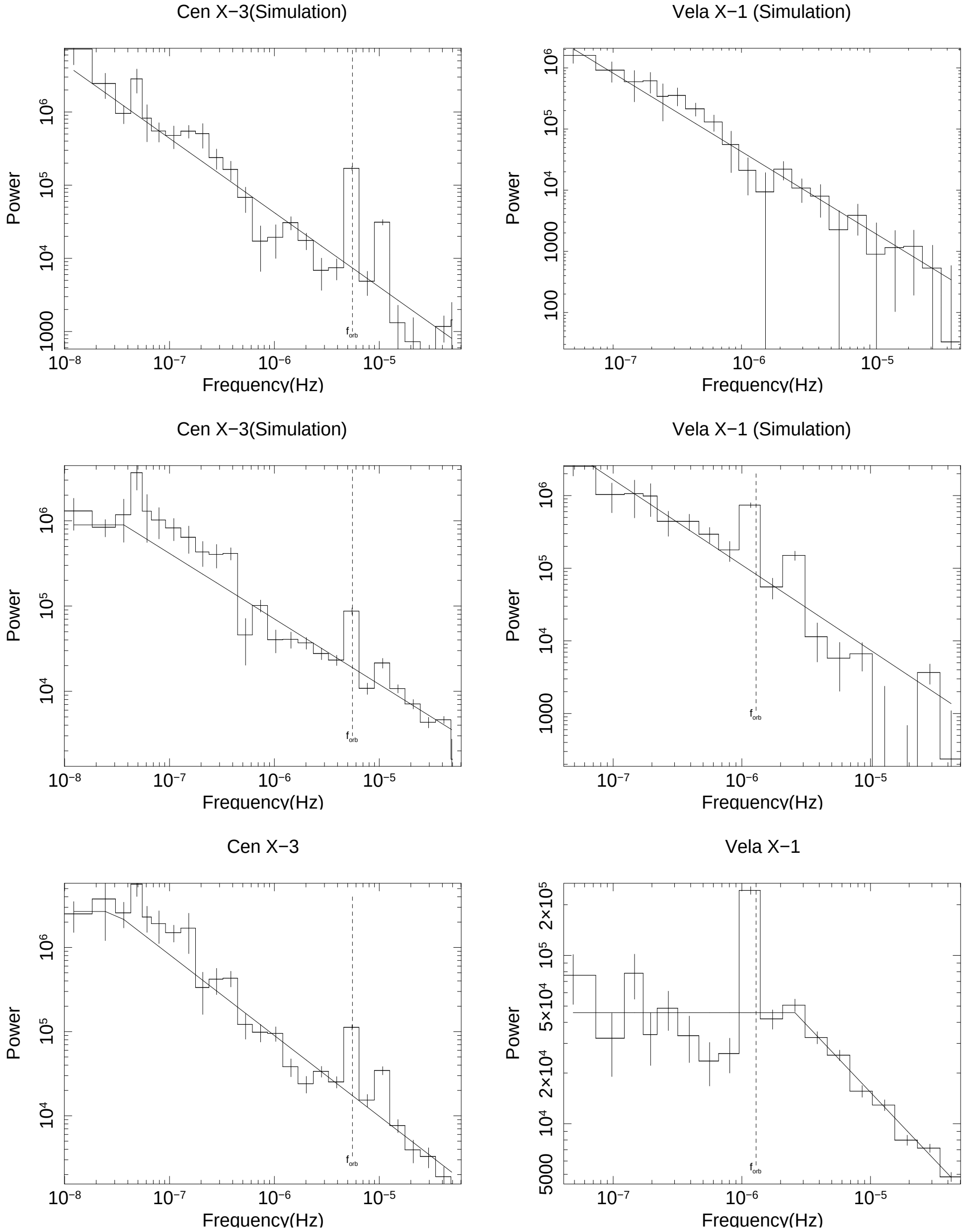

Figure 5.5: On the left side, the simulation results of Cen X-3 is presented. The top figure is the power density spectrum in power law with orbital modulation, the middle one is the same as the former but the state transitions are taken into account, and the bottom figure is the real PDS of Cen X-3. On the right side, the simulation results of Vela X-1 is presented. The top figure is the power spectrum only in power law, the middle one is the PDS in power law with orbital modulation, and the bottom figure is the real PDS of Vela X-1. It is clear from the figures that sinusoidal orbital modulation does not affect the trend of the power law, but the state transitions cause an artificial break in the PDS.

5.4 Discussion

X-ray binaries show X-ray flux variations in a broad range of time-scales. The power density spectrum of a system often reveals a number of periodic and quasi-periodic phenomena that can be related to orbital motion of the binary system, rotation of the central star and some quasi-periodic phenomena. In addition, aperiodic variability is observed, giving rise to the broad band continuum component in the power density spectrum, extending from $\sim 10 - 100$ ms to the longest time-scales accessible for monitoring instruments (Gilfanov and Arefiev, 2005). Due to the fact that the conditions for creation of X-ray radiation are only provided in the vicinity of the central object, the variations in the X-ray flux give us some idea about the events, such as the alterations in the mass accretion rate, going on there. When the periodic features in the X-ray spectra are taken into account, it is seen that low frequency X-ray variations also appear besides high frequency variations. High frequency variations are typical for the characteristic time-scales in the region of main energy release due to large gravitational interactions and so short lifetimes before falling into the object, but the shorter ones correspond to the many orders of magnitude of these time-scales, so they should originate from the outer parts of the accretion flow and propagate to the region of main energy release. The size of the accretion disc is finite and so there is a longest time-scale for an event, such as perturbation of the disc, changes in the mass transfer rate, defined for an accretion disc. This is the viscous time-scale on its outer boundary, $t_{\rm visc}(R_d)$. If the frequency of a variation is smaller than $t_{\rm visc}(R_d)^{-1}$ the corresponding X-ray flux variations are considered to be uncorrelated; therefore, the corresponding power density spectrum is expected to exhibit a white noise behaviour along these frequencies.

We stated that our main aim in this study is to relate the break frequency, i.e. the transition frequency from white noise to red noise in the power density spectrum, with the viscous time scale. One practical way to interpret analysis results is to examine the ratio $f_{\rm visc}/f_{\rm orb}$ theoretically and the ratio $f_{\rm break}/f_{\rm orb}$ observationally.

From (3.24) and using $\mathcal{M} = v_\phi/c_s \sim H_d/R_d$ we can deduce that

$$t_{\rm visc} \sim \alpha^{-1} \left(\frac{H_d}{R_d}\right)^{-2} \left(\frac{GM_1}{R_d^3}\right)^{-1/2} \tag{5.13}$$

The orbital frequency of the binary system having a binary separation a is determined from the third Kepler law

$$P_{\mathrm{orb}} = 2\pi a^{3/2}[G(M_1 + M_2)]^{-1/2}, \tag{5.14}$$

and the following ratio is obtained

$$\frac{f_{\mathrm{visc}}}{f_{\mathrm{orb}}} = \frac{2\pi\alpha}{\sqrt{1+q}}\left(\frac{H_d}{R_d}\right)^2\left(\frac{R_d}{a}\right)^{-3/2} \tag{5.15}$$

We have derived the ratio H/R as (3.19) and with the typical low mass X-ray binary quantities, this ratio is found to be around 0.02-0.04. Account for the irradiation effects does not change this ratio significantly due to large optical depth of the Shakura-Sunyaev disc (Liutyi and Siuniaev, 1976). With plausible values of two other parameters, $\alpha \sim 0.5$ and $R_d/a \sim 0.3 - 0.6$, the standard disc theory predicts (Gilfanov and Arefiev, 2005):

$$\left(\frac{f_{\mathrm{visc}}}{f_{\mathrm{orb}}}\right) \sim 0.005 - 0.07 \tag{5.16}$$

for low mass X-ray binaries. The same ratio is a bit larger for the high mass X-ray binaries. The probable region for the dependence f_{visc} vs. f_{orb} is displayed in Fig. 5.6 as the shaded region.

Table 5.1 indicates that the values $f_{\mathrm{visc}}/f_{\mathrm{orb}}$ are separated into two groups: range of the first one is 0.05-0.4 and the other range is 0.8-2.6. Both are quite far from the interval predicted by the ’standard theory’ calculated above. However, Fig. 5.6 below points to an obvious correlation between break and orbital frequencies. The question is why these observations are so different from the predictions of the ’Standard Theory’. We try to discuss some possible explanations in the next sections by treating the LMXBs and HMXBs differently since they are quite dissimilar systems.

5.4.1 LMXBs

Equation (5.15) indicates that we should firstly question the component $\alpha(H/R)^2$ to find an explanation for our results while the thin disc requirement should be kept in mind, which will require very large values of α. One other discussion is on the value of R_d/a, and this should be handled taking account of the limits for the accretion disc radius, which is roughly sketched in Fig. 3.6.

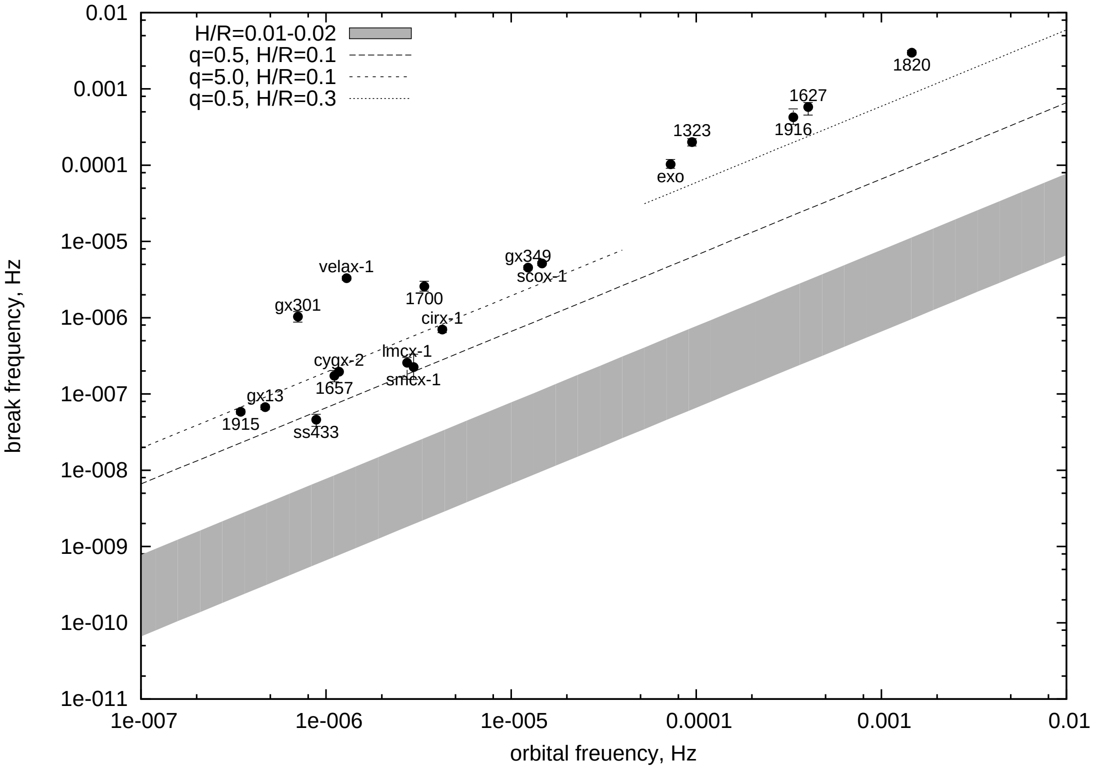

Figure 5.6: The relation between the PDS break frequency and the orbital frequency of the binary system the findings of Gilfanov and Arefiev (2005) regarding short-period LMXRBs being included. The large shaded area toward the bottom of the plot is the widest region possible for the dependence $f_{\rm visc}$ vs. $f_{\rm orb}$ according to the α-disc, obtained from Eq.(5.15) in the mass ratio range $2.91 \leq q \leq 22.77$ for $\alpha = 0.5$.The dashed lines are predictions for larger values of the disc thickness H/R with $\alpha = 0.5$ and q values indicated on the plot. Most of the errors in $f_{\rm break}$ are on the order of marker (or symbol) size.

There are also some other important proposals to explain the differences between the theoretical predictions and observational facts. Among these, the one using the resonance phenomenon mentioned above and the one focusing on the effects of irradiation by the central object on the accretion disc deserve careful consideration.

5.4.1.1 Disc thickness or α-parameter?

Before handling α and H/R, we should recall the physical limits for the radius of an accretion disc. As stated in Section 2.1 the formation of the disc starts at the circularization radius, $R_{\rm circ}$, so an accretion disc cannot have an outer radius less than this value. On the other hand, the upper limit for a steady disc radius is given by the tidal truncation radius, which is very likely close to the largest non-intersecting periodic orbit (Paczynski, 1977). Using the calculations of Paczynski, Gilfanov and Arefiev (2005) approximates the largest non-intersecting orbit

$$\frac{R_{\text{tidal}}}{a} = 0.112 + \frac{0.270}{1+q} + \frac{0.239}{(1+q)^2} \tag{5.17}$$

accurate to $\sim 3\%$ in the range of $0.06 \leq q \leq 10$ (applicable to LMXBs). On the other hand, many observations show that the radii of steady discs are close to their expected tidal truncation radii.

An average value of $q \sim 3.0$ gives R_d/a and using the appropriate $\alpha \sim 0.5$, our results require $H/R \geq 0.1\alpha_{0.5}^{-1/2}$. Therefore, if we want to preserve thin disc approximation, i.e. $H/R \sim$ a few times of 0.01, we find α to be 2-50; however, this contradicts $\alpha \leq 1$. If we keep $\alpha \leq 1$ in the thin disc case, we need help from the ratio R_d/a and calculate it to be < 0.03 which is again far from the observed values and also notably smaller than the value of R_{circ}/a determined using (2.3) and (2.4) to be ~ 0.1. Another interpretation is proposed by Gilfanov and Arefiev (2005): the possibility that only the inner part of the disc, $R/a \leq 0.03$, contributes to the observed variability of X-ray binaries in X-ray spectrum. However, some of the sources (Sco X-1, GX 349+2) exhibit considerably sharp breaks and this is a sign of very narrow transition region from (outer) very low $\dot{M}$ perturbations to inner and larger ones.

5.4.1.2 Tidal resonances, instability?

In Section 3.6 we discussed some conditions necessary for resonance phenomenon and stated that resonances may cause tidal instabilities that eventually truncate the disc at a certain radius. Resulting in smaller R_d/a values, resonances may appear to be plausible to account for our results. However, we have to go more deeply into the situation. The most important fact we need to bear in mind is that the resonance radius expressed by (3.51) should be in the limits predicted for disc radius. Section 3.6 mentions the argument about R_{21} and R_{32} resonant radii in the mass ratio range $q \leq 1$ and concludes that only R_{32} is possible for $q \leq 0.3$ since R_{21} requires extremely low mass ratios to be in between R_{circ} and R_{tidal}. 2:1 and 3:2 resonances are the two strongest resonances, the higher ordered ones are not such effective and indeed they are not probably excited in the accretion discs. Coming back to our sources, it appears that the mass ratio is smaller than 0.3 for only one binary, GRS 1915+105; hence, we cannot accept resonances alone as a part of our discussion. Nevertheless, it worth noting that resonances may be a reason for dichotomy between long and short orbital period-binaries as indicated in the paper of Gilfanov and Arefiev (2005), in which they report the break frequencies of 6 additional low mass ratio binaries and show that significant dichotomy in the value of $f_{\rm break}/f_{\rm orb}$ ratio between long and short period-binaries.

The absence or weakness of resonances in the discs of our sources does not mean that we cannot encounter any tidal instability; resonances just strengthen the tidal effects. There should be some other impacts of tidal instability, usually generated by the secondary star in close binaries, other than truncation of the disc. There are some suggestions for the mechanism by which the tidal instability is affecting the viscous time of the disc, neither of which has been proven to be completely true. These can be summarized as follows:

(i) Tidal forces cause tidal waves in which mass transfer occurs. The propagation speed of these waves is much larger than the radial drift velocity, so the waves may decrease the viscous time-scale (Gilfanov and Arefiev, 2005).

(ii) Tidal interaction heats the outer disc and increases the temperature of the disc and coronal flow. Therefore, the viscous time scale drops down (Whitehurst and King, 1991).

(iii) The tidal forces have an influence on the trajectories in the disc, so may change the eccentricity or cause precession. Taking these into consideration implies we should give up the idea of Keplerian orbits and this is a rather complicated issue.

5.4.1.3 Back to disc thickness

Searching for an explanation for the distinction between the theory and observational outcomes brings us back to the thickness of the disc, but from a different point of view this time. There are two propositions by Gilfanov and Arefiev (2005).

First one is the semi-thick disc case. Calculations show that optical depth of the disc is highly dependent on the disc thickness, but not in a positive way. Gilfanov and Arefiev (2005)'s argument is as follows. Under the assumption of vertical hydrostatic equilibrium and stationarity, both the mid-plane disc temperature and the density are steep functions of the disc thickness: $T/T_{\rm vir} \propto (H/R)^2$, $\rho \propto (H/R)^{-3}$. Due to strong dependence of the Rosseland mean opacity on the density and temperature, typically as $\kappa_R \propto \rho^{\approx 1} T^{\approx -3.5}$ in the parameters range of interest, the optical depth of the disc $\tau_R = \kappa_R \rho H$ is also a steeply decreasing function of the disc thickness, $\tau_R \propto (H/R)^{-\gamma}$ with the power law index γ changing from ~ 12 to ~ 3 as H/R increases. Therefore, even a moderate increase of the disc thickness would lead to dramatic decrease of its optical depth. This is why it is called semi-thick disc. As a result, for $H/R \sim 0.1$, the accretion disc in the majority of LMXBs from our sample would be optically thin. This would contradict to a number of observational facts, mostly from the optical band, proving existence of the optically thick outer disc in LMXBs. On this basis, the possibility of the semi-thick, $H/R \sim 0.1$ outer disc in LMXBs can be excluded (Gilfanov and Arefiev, 2005).

The other suggestion, which is stronger, is founded on a two phase accretion flow with a Shakura-Sunyaev-like disc in the mid-plane surrounded by the tenuous optically thin coronal flow with the aspect ratio $H/R \sim 0.1 - 0.2$ and temperature $T \sim 10^{-2} T_{\rm vir}$. This hypothesis is competent only if about the same amount of mass is accreted through the central disc and the corona in unit time, i.e. $\dot{M}_{\rm corona} \sim \dot{M}_{\rm disc}$. Still, that does not mean the disc and the corona contain equal masses of matter. In fact, the dependence of surface density on disc thickness, $\Sigma \propto (H/R)^{-2}$, deduced from the Shakura-Sunyaev disc solution (3.18), brings out that only about 10% of total mass is located in the corona:

$$\frac{\Sigma_{\rm corona}}{\Sigma_{\rm disc}} \sim \frac{f_c}{1 - f_c} \left(\frac{H_{\rm corona}}{H_{\rm disc}} \right)^{-2} \leq 0.1 \tag{5.18}$$

since $f_c = \dot{M}_{\rm corona}/\dot{M} \sim 0.5$ and $H_{\rm corona}/H_{\rm disc} \leq 0.03/0.1 = 0.3$ (Gilfanov and Arefiev, 2005).

The coronal flow may be initiated by many ways. The idea of a plausible mechanism belongs to Meyer and Meyer-Hofmeister (1994). It is basically based on the phenomenon of irradiation by the primary, and Compton heating and cooling of the disc-corona system, which we discussed in section 3.5. The X-ray emission near the central relativistic object increases the fraction of the coronal flow (Meyer et al., 2000; Jimenez-Garate et al., 2002).

The existence of corona over an accretion disc can be confirmed by some other observational methods. The presence or absence of the corona in one's line of sight alters what s/he sees in the spectrum, obvious in Fig. 5.7, but that type of observation is only possible for X-ray binaries with high inclination angles - the ADC sources and dippers. These sources undergo partial X-ray eclipses which enable one to detect the corona with its physical properties like optical thickness. Most of the calculations regarding temperature, radial extent, optical depth etc. of the corona have been in agreement with the predictions.

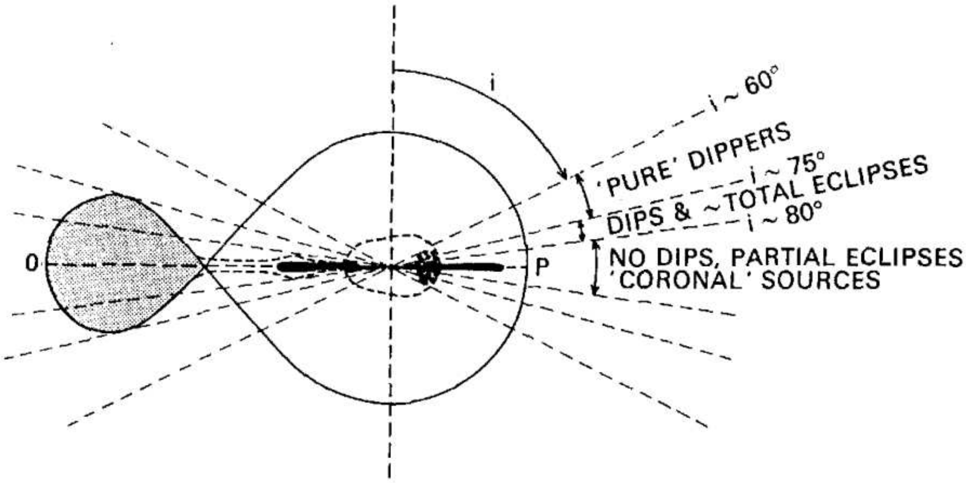

Figure 5.7: Axial cross-section showing the structure of the accretion disc and the corona (Taken from Frank et al. (2002) P106)

5.4.2 HMXBs

The break frequencies determined for the 7 HMXBs separate them into two groups as seen in Fig. 5.6. The break frequencies of Vela X-1, 4U 1700-377 and GX 301-2 are 5-33 times higher normalized frequencies than those of the other HMXBs. Since the normalized break frequencies are associated with viscosity time-scales of the accretion discs, higher break frequency implies tinier discs around Vela X-1, 4U 1700-377, and GX 301-2 compared to the other sources. This distinction could only be due to differences in their accretion processes (Içdem and Baykal, 2011). As mentioned earlier there are two main accretion mechanisms for HMXBs owing to the nature of the optical counterparts in these systems: Roche-lobe overflow and stellar wind accretion. Roche lobe overflow is a more steady accretion process and leads to formation of persistent discs. Stellar wind accretion, on the contrary, is a very chaotic mechanism and produces thin and unstable accretion discs. Among the HMXBs analysed here, SS 433 and SMC X-1 have been determined to be Roche-lobe overflow binaries, Vela X-1, GX 301-2 and 4U 1700-377 are wind-accreting systems. The remaining two sources, OAO 1657-415 and LMC X-1 have not been identified as Roche-lobe overflow or wind-accreting systems, but they have been observed to exhibit signs of both of the mechanisms. Each source is handled individually by taking into account the findings about it, so that its break frequency value can be interpreted better.

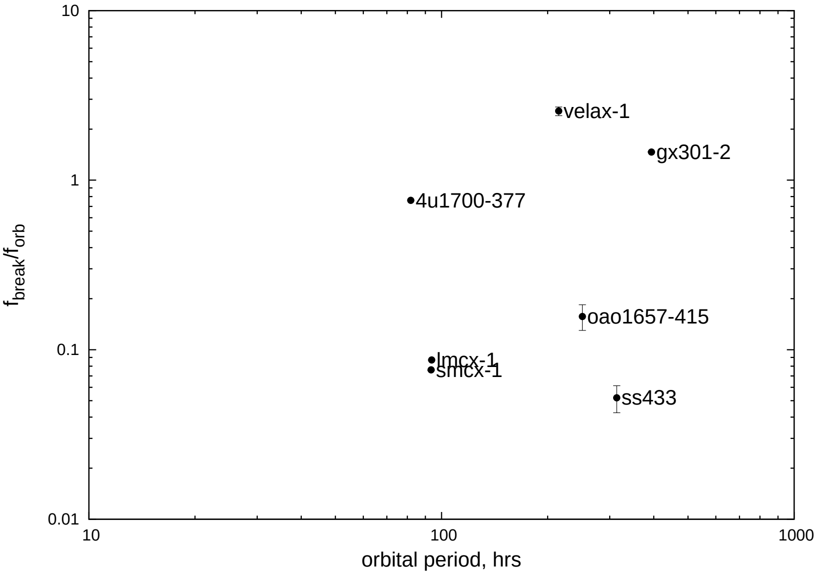

(a)

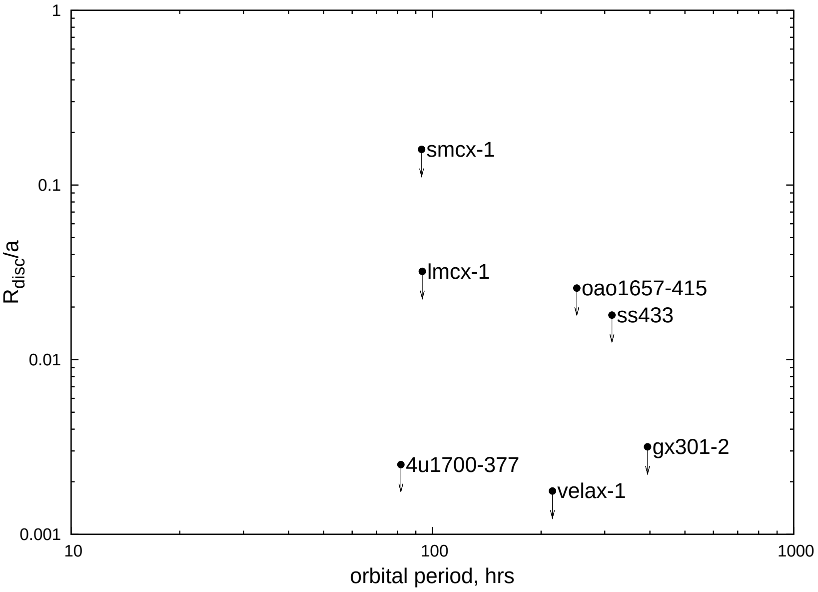

(b)

Figure 5.8: (a)Dependence of the ratio $f_{\text{break}}/f_{\text{orb}}$ on the orbital period of the binary system. Some of the errors in $f_{\text{break}}/f_{\text{orb}}$ are on the order of the marker (or symbol) size. (b)Relation of the normalized outer disc radius to the orbital period of the system. The arrows represent the possible ranges of the outer disc radii (Blondin, 2000).

5.4.2.1 Vela X-1

Vela X-1 is a pulsar-supergiant binary in which mass transfer is provided by the violent stellar wind of the supergiant. The frequency of the X-ray pulses observed from the pulsar have shown rapid variations, which are indicative of spin-up and spin-down phases for its rotation (Deeter et al., 1989) and this variability is mainly attributed to some torque reversals exerting on the pulsar, i.e. the direction of the torque changes because of the reversal of the direction of rotation of the matter surrounding the pulsar, which forms a temporary disc. Simulations suggest that this temporary disc originates as a result of the the flip-flop instability of the accretion shock from the stellar wind to the pulsar (Blondin and Pope, 2009). Calculations of Boynton et al. (1984) points out to 2-3-day torque reversals for Vela X-1. In fact, this range is not far from the viscous time inferred from the break frequency determined from its PDS. What torque reversal period tells is that ”the resulting disc is very unstable and cannot extend to a large radius in the observed 2-3 days as its dispersion is dominated by viscosity” (Içdem and Baykal, 2011).

It is possible to estimate inner and outer limits for the radii of an accretion disc to be formed in Vela X-1. Section 2.4 mentions the effects of high magnetic fields on the accretion discs. Since the magnetic field of the pulsar is rather high, $\sim 10^{12} - 10^{13}$ G, it is the most effective factor limiting the disc from inside. Using (2.30), the Alfvén radius is calculated to be $r_{Alfvén} \simeq 3.9 \times 10^8$ cm. Prediction of outer radii of accretion discs of wind-driven HMXBs is not straightforward as there are many factors to consider. Nevertheless, ”the upper limit to a possible disc radius is considered to be determined by the tidal forces and $R_{\rm tidal} \simeq 0.9 R_{\rm L}$ independent of the characteristics of the disc ($R_{\rm L}$ is the Roche-lobe radius of the compact star)” (Içdem and Baykal, 2011). The Roche-lobe radius is given by the following analytical expression (Eggleton, 1983)

$$\frac{R_{\rm L}}{a} = \frac{0.49}{0.6 + q^{2/3}\ln(1 + q^{-1/3})}, \tag{5.19}$$

which implies that $R_{\rm tidal} \simeq 6.0 \times 10^{11}$ cm for Vela X-1. Hence, an accretion disc that can survive in Vela X-1 have a radius that is greater than the Alfvén radius and smaller than the tidal radius. This does not contradict with the disc radius estimate, $R_d \simeq 4 \times 10^9$ cm, calculated by equating the $f_{\rm break}/f_{orb} = 2.56$ ratio to the the theoretical expression for $f_{\text{visc}}/f_{\text{orb}}$ (5.15), derived from the Shakura-Sunyaev disc model with a thin disc approximation.

5.4.2.2 GX 301-2

GX 301-2 has been observed to experience several spin-up episodes since 1984, which may be indicative of the formation of equatorial accretion discs from tidal streams (Koh et al., 1997). These tidal streams were found to last for about 20 days, i.e. twice in an orbital period. The break frequency of GX 301-2 corresponds to a $\sim$ 11-day time-scale. Thus, ”the duration of the temporary accretion disc and the time-scale we obtained from its break frequency are of the same order implying that it has a small accretion disc, as Fig.5.8-b also indicates” (Içdem and Baykal, 2011).

5.4.2.3 4U 1700-377

The optical companion of 4U 1700-377, HD 153919, was reported to under-fill its Roche-lobe by Conti (1978); hence, the accretion of matter should be driven by wind flow instead of the Roche-lobe overflow. In addition, X-ray flux variations of period $\sim$ 13.8 days and episodic quasi-periodic oscillations have been detected from 4U 1700-377 (Hong and Hailey, 2004). These facts reinforce the probability of the formation of a short-scale transient disc. Its break frequency value corresponds to $\sim$ 4.4-day time-scale, and its location on Fig.5.8-b indicates that its accretion disc may be of similar size to those of Vela X-1 and GX 301-2.

5.4.2.4 SMC X-1

The location of SMC X-1 is among the low-mass X-ray binaries, i.e. Roche-lobe overflow systems. This is expected since it is a confirmed Roche-lobe overflow system. Its normalized break frequency is very small, 0.076, and implies that the pulsar has a very large accretion disc.

5.4.2.5 OAO 1657-415

There has not been any solid evidence to prove that OAO 1657-415 is either a Roche-lobe overflow or a wind-accreting system. However, it has been observed to display torque reversals as in the case of Vela X-1, but with much longer time-scales of the order of weeks (Finger and Prince, 1997). In addition, its X-ray flux and angular acceleration fluctuations implies the formation of episodic accretion discs (Baykal, 1997, 2000). The normalized break frequency is 0.16 implies a time-scale of $\sim$ 66 days and this value is in accordance with its torque reversal time-scale (Finger and Prince, 1997). In fact, ”that OAO 1657-415 has a unique place in the Corbet diagram in-between supergiant under-filled Roche Lobe overflow and Be transients suggests that there is a longer living accretion disc relative to the supergiant wind-fed systems” (Içdem and Baykal, 2011).

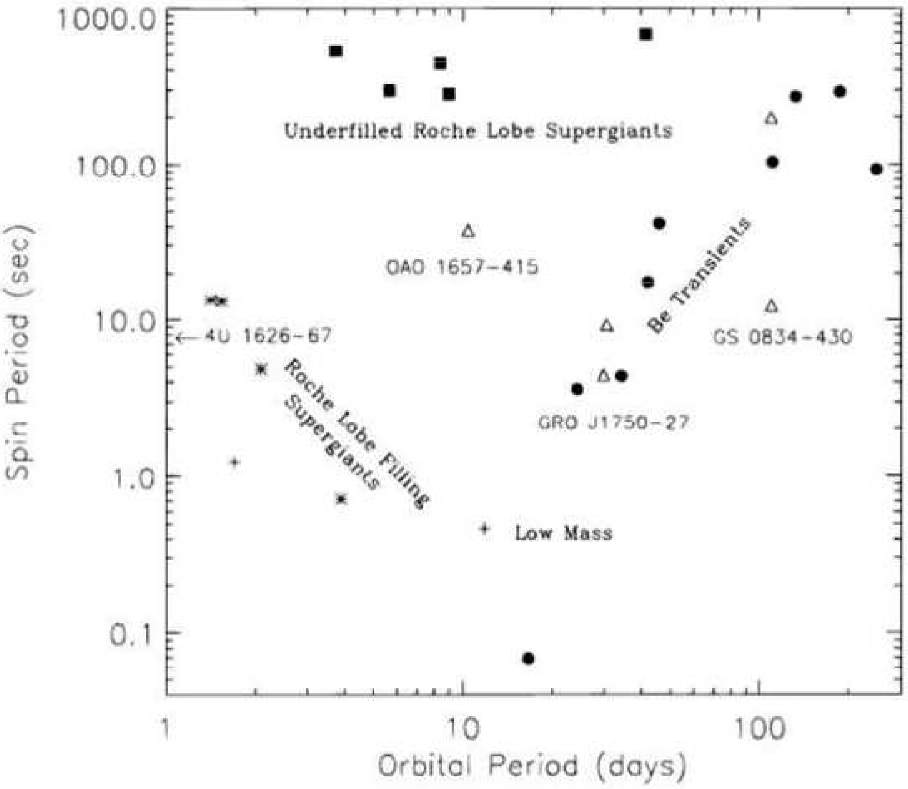

Figure 5.9: Spin period (P_{spin}) vs. orbital period (P_{orb}) plot for accretion powered pulsars, or the Corbet Diagram (Corbet, 1984). *Asterisks*: SG/XBs that are Roche lobe filling. *Squares*: SG/XBs that underfill their Roche lobe. *Circles*: Be/XBs. *Pluses*: LMXBs. *Triangles*: binary pulsars with unknown companion type (Bildsten et al., 1997).

5.4.2.6 SS 433

SS 433 is a very famous black hole binary. Its break frequency determined here is consistent with the previously reported value, $\sim 10^{-7}$ Hz, of Revnivtsev et al. (2006). It was confirmed to have a Roche-lobe-overflow-powered accretion disc similar to the low mass X-ray binaries (Begelman et al., 2006). Thus, it is not unusual to expect it to behave somewhat similarly to low-mass X-ray binaries regarding its accretion disc features. Its position on the plot of the correlation of break frequency to orbital frequency (see Fig.5.6) is very close both to the LMXBs and to SMC X-1. Thus, although their compact objects differ, SS 433 and SMC X-1 resemble each other with their accretion discs.

5.4.2.7 LMC X-1

LMC X-1 is a good candidate for being a black hole binary. It is an unusual HMXB because it is a wind driven system with a steady state disc. ”The reason why it is considered to be a wind accretor despite having a persistent disc is that the optical counterpart of the compact star fills only 45% of its Roche lobe (Orosz et al., 2009)” (Içdem and Baykal, 2011). As usual, LMC X-1 is expected to have a shorter viscous time-scale than those of Roche-lobe overflow systems because of its smaller disc size. However, its normalized break frequency, 0.087, is very low and it is located among Roche-lobe-overflow binaries on the $f_{\rm break}$-$f_{\rm orb}$ correlation plot despite being expected to be near the group of Vela X-1. The claim of Ruhlen and Smith (2010) is a plausible explanation for this unexpected fact. They say that ”LMC X-1 is neither a Roche-lobe-overflow binary nor a wind-accretor, but sits at the boundary” and their reasoning is that the emission and spectral properties of the source do not belong to any specific group. Nonetheless, more detailed analysis should be performed to reveal some key properties of LMC X-1 and so to account for its unusual behaviour.

CHAPTER 6

TIMING and X-RAY SPECTRAL FEATURES of SWIFT J1626.6-5156

6.1 Observations

We analysed *RXTE*-PCA data of SWIFT J1626.6−5156 in the interval from 53724 MJD to 55113 MJD with a total exposure of ~ 449 ks composed of 411 separate observations with exposures between ~ 1 ks and ~ 2 ks.

The number of active PCUs of *RXTE* vary in time, and so did it during observations covered in our analysis. ”Before MJD 53964, there were 1-2 ks long observations every 2-3 days. After MJD 53964, observations were sampled in pairs, containing two consecutive 1-2 ks long observations separated by ~ 0.3 – 0.6 days. Each of these pairs were separated from each other by ~ 9 – 10 days” (Icdem et al., 2011b). All available layers of the PCUs were used for the timing analysis, while for the spectral analysis only the PCU2 layers were used.

In addition to the *RXTE*-PCA data, a single observation of the *Chandra*-ACIS (AXAF CCD Imaging Spectrometer, (Garmire et al., 2003)) belonging to 54897 MJD with an exposure of 20 ks in the ACIS-S FAINT TE (times exposure) mode was analysed to strengthen the timing results.

6.2 Timing Analysis

Light-curves for the timing analysis were extracted from 3-20 keV energy interval with a time resolution of 0.375 s from *RXTE*-PCA GoodXenon data. We subtracted a background model, which is obtained by the standard PCA analysis tool pcabackest using the public estimator models for *RXTE*-PCA data, from these light-curves. After that, these arrival times were also corrected to the Solar system barycentre.

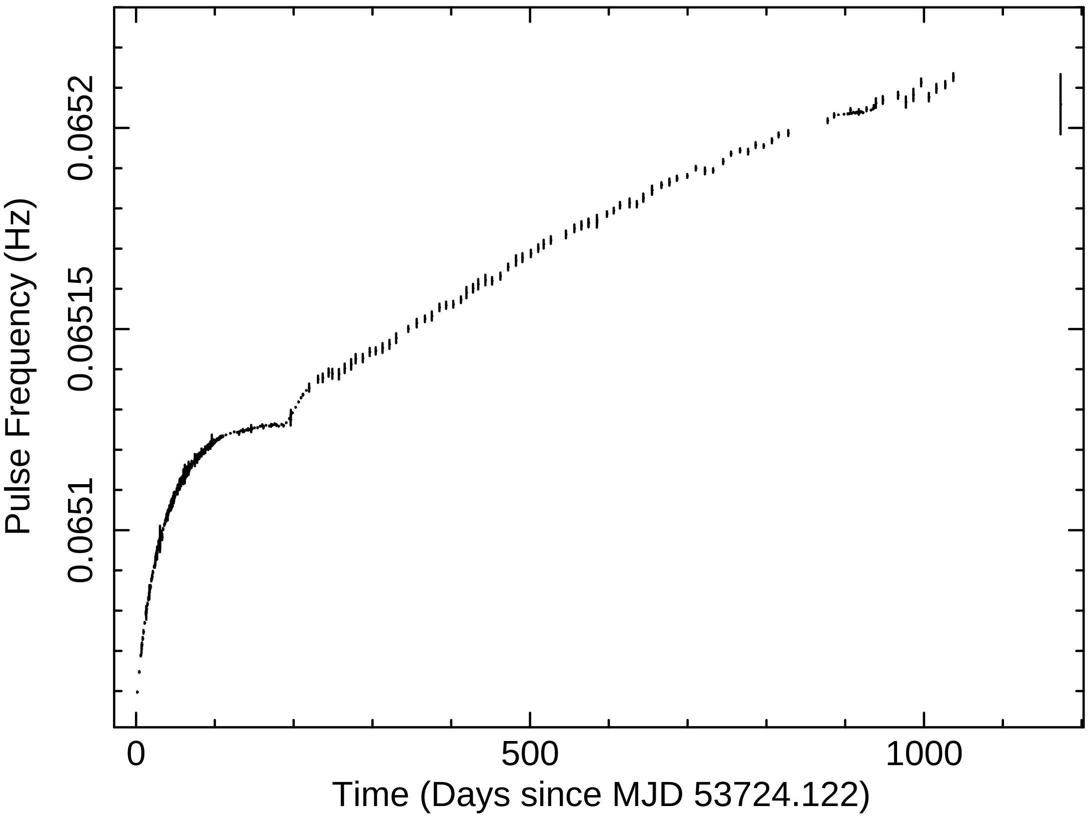

Figure 6.1: Pulse frequency evolution of SWIFT J1626.6−5156 after correcting for the binary orbital motion. The rightmost point corresponds to the Chandra-ACIS observation.

Pulse timing analysis was done using the method of cross-correlation of the harmonic representations of the pulses as described in Sec. 7.1. The pulses for the time interval between 53724 and 55113 MJD were obtained using the quadratic frequency evolution whose parameters were found by Baykal et al. (2010) (see Table 6.1 for the parameters)

$$\nu = \nu_0 + \dot{\nu}(t - t_0) + \frac{1}{2}\ddot{\nu}(t - t_0)^2. \tag{6.1}$$

Table 6.1: Timing solution of Swift J1626.6-5156 (taken from Baykal et al. (2010))

Parameter	Value
Epoch for spin frequency (MJD)	54178.24(5)
ν (Hz)	0.065161110(3)
$\dot{\nu}(10^{-12}$ Hz.s$^{-1})$	1.31(2)
$\ddot{\nu}(10^{-21}$ Hz.s$^{-2})$	-7.5 ± 3.2
Orbital period (days)	132.89(3)
$a/c \sin i$ (lt-s)	401(5)
Orbital epoch at $\pi/2$ (MJD)	54031.44(5)
Eccentricity	0.08(1)
ω (longitude of periastron)	340(9)

”We were not able to obtain pulse frequencies using the cross-correlation technique for the data after MJD ~ 54750 since the pulse profiles obtained for these data were found to be statistically insignificant” (Icdem et al., 2011b). The pulse frequency evolution of SWIFT J1626.6−5156 is presented in Fig. 6.1.

The *Chandra*-ACIS observation of Swift J1626.6−5156 on 54897 MJD were used to extract a 20 ks-light-curve with a time resolution of 0.44 s, and 8 pulse profiles were obtained from ~ 2.5 ks long segments of this light-curve. Using the template pulse profile obtained from the whole observation to cross-correlate with these sample pulses, the spin period of the source is determined to be $(6.52059 \pm 0.00075) \times 10^{-2}$ Hz. The template pulse profile belonging to the energy range 0.3-8 keV is presented in Fig. 6.2.

Fig. 6.3 displays the pulse frequency derivatives of the source between 53724 and 54750 MJD, which was acquired by linear fitting of consecutive pulse frequencies with a time span of $\sim 10 - 140$ days, as a function of the corresponding 3-20 keV unabsorbed flux values.

6.3 Spectral Analysis

The 3-20 keV unabsorbed flux values of Swift J626.6−5156 presented in Fig. 6.3 were determined from the X-ray spectra of *RXTE*-PCA data. The time intervals were

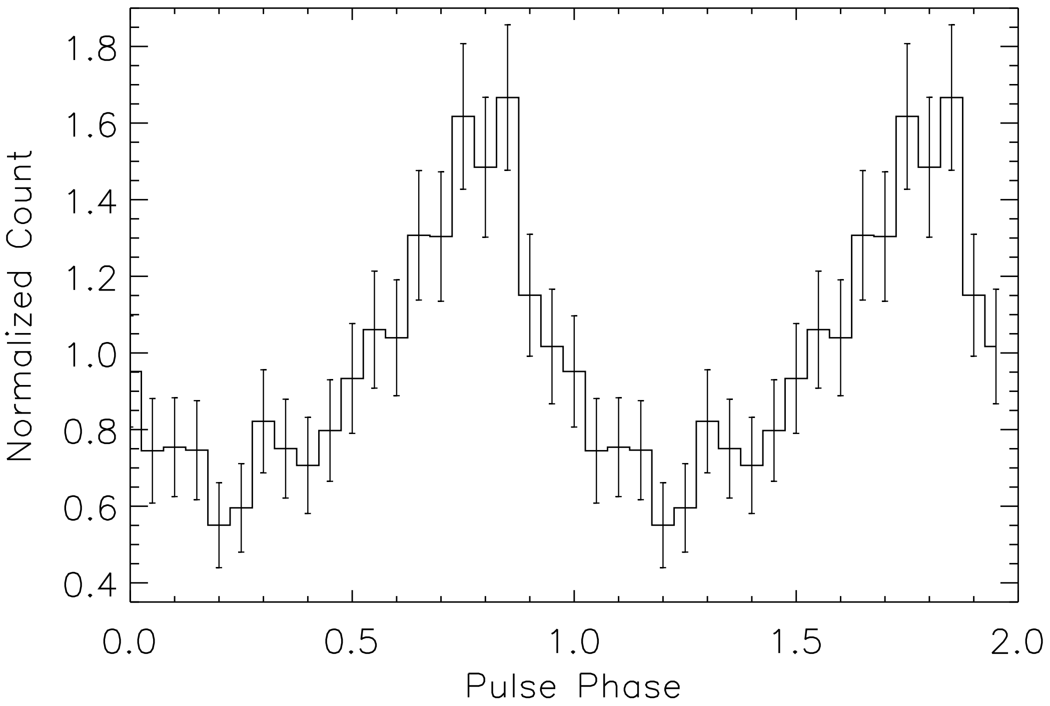

Figure 6.2: 0.3-8 keV pulse profile obtained from the Chandra ACIS observation.

selected so that they correspond to the spin frequency derivative measurements. These spectra were constructed with the standard FTOOLS 6.9 data analysis software, using the Standard-2 mode data, which provides 128 channels with 16-sec time resolution. The auxiliary background and response matrix files were also created in a suitable form. Because of the sensitivity problems of the instrument, the energy channels corresponding to energies $E < 3 \& E > 20$ keV were eliminated. The remaining photons were used to model the X-ray spectra of the source by power law with high energy cut-off and an additional Gaussian centred at the iron line peak. 0.6% systematic error was added to the errors (see Wilms et al. (1999); Coburn et al. (2000)). Also, the X-ray spectrum of the source in the 0.3-8 keV energy range is obtained from the *Chandra*-ACIS data using the standard analysis tools of CIAO Software Package. In Table 6.2, we present a collection of the spectral results.

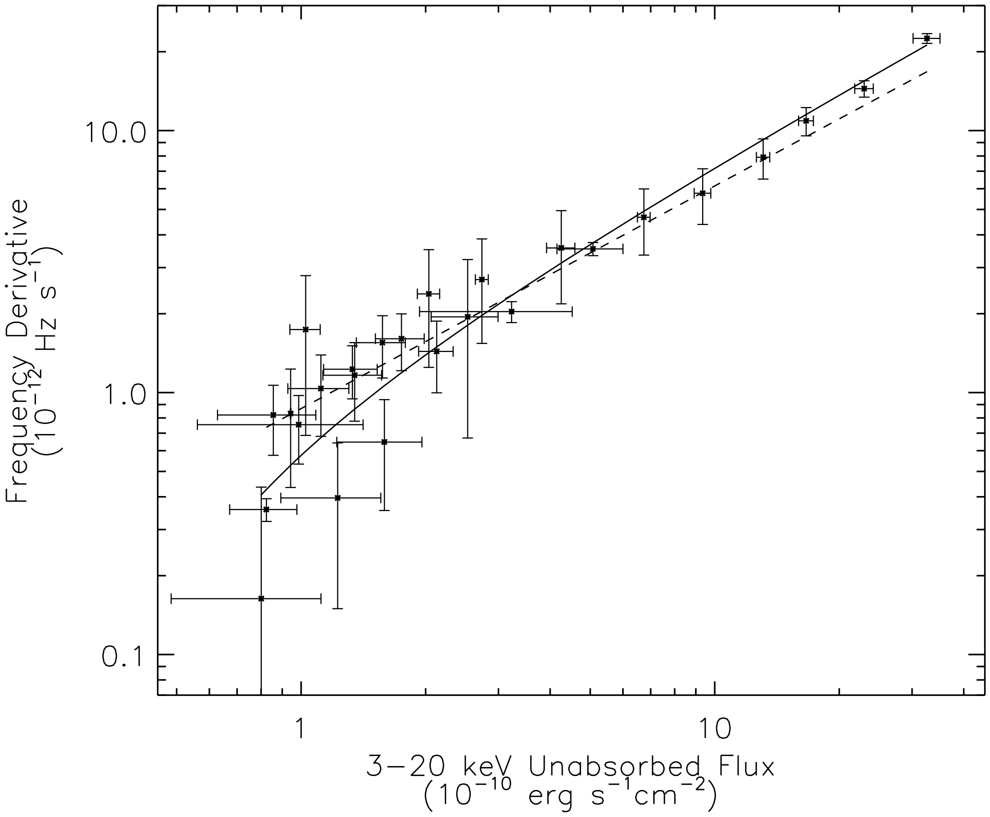

Figure 6.3: Frequency derivative of SWIFT J1626.6−5156 as a function of 3-20 keV unabsorbed X-ray flux obtained from RXTE-PCA observations. Solid and dashed lines correspond to the torque models with and without dimensionless torque parameter respectively.

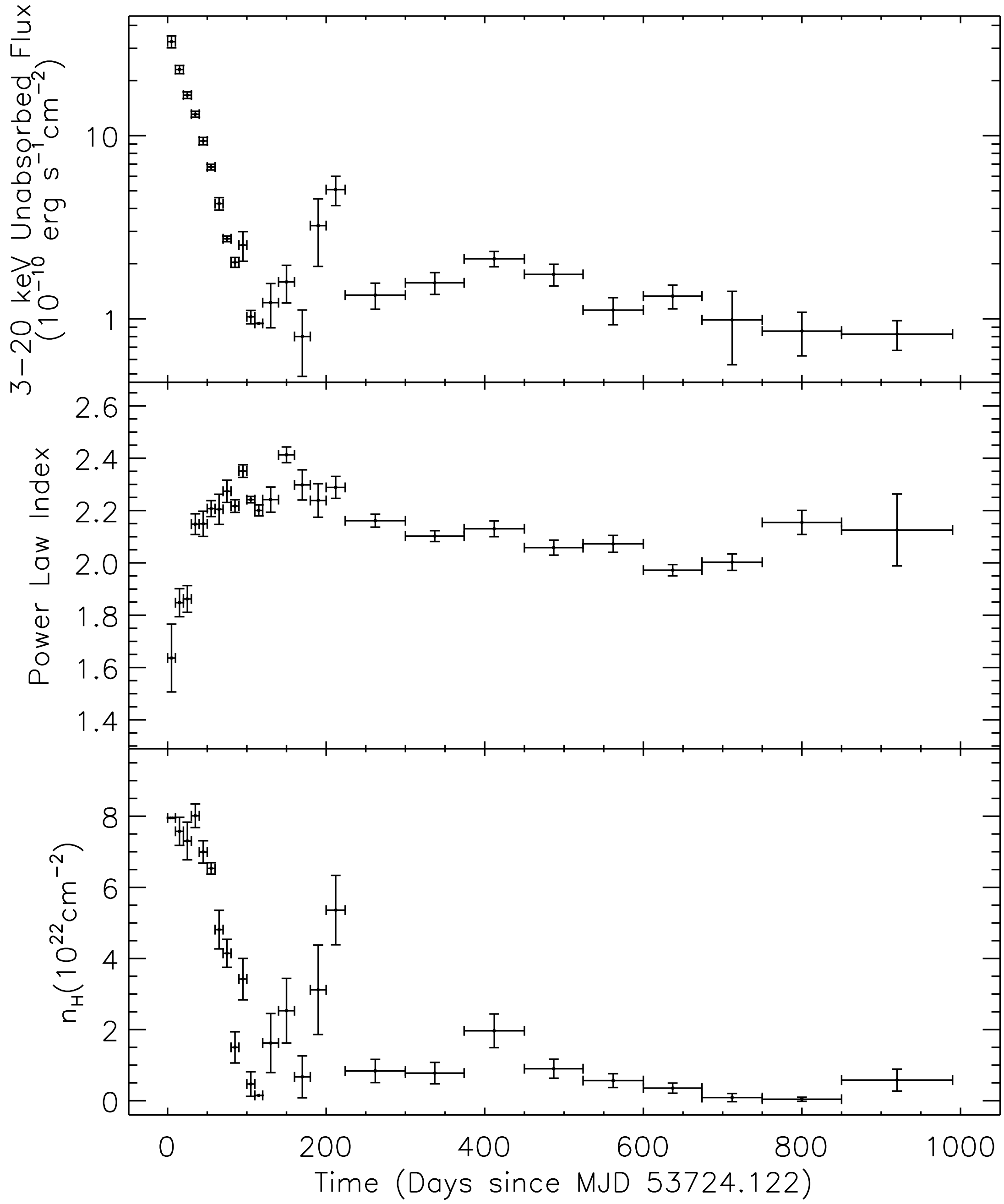

Figure 6.4: Temporal variations of 3-20 keV unabsorbed X-ray flux, power law index and Hydrogen column density.

To fit the X-ray spectra, we used an absorbed power law model with an high energy cut-off expressed as $e^{(E_C-E)/E_F}$ where E_C is the cut-off energy and E_F is the e-fold energy (see White et al. (1983)). In addition to this model, Iron line complex was modelled as a Gaussian peaking at $\sim$ 6.5 keV. We could not resolve Cyclotron lines of the source around $\sim 10-20$ keV as suggested by Coburn et al. (2006). Temporal variations of the unabsorbed X-ray flux, power law index and Hydrogen column density were presented in Figure 6.4. Average values of cut-off energy and e-fold energy values were found to be $\sim$ 15keV and $\sim$ 10keV respectively. To demonstrate long term spectral evolution of the source, we also constructed 3 long term RXTE-PCA spectra of the source (see Table 6.2).

6.4 Discussion

Accretion powered pulsars are expected to exhibit a correlation between their spin-up rates and X-ray fluxes as explained in Section 2.6. This has been verified by the observations of many accretion powered pulsars: EXO 2030+375 (Parmar et al., 1989; Wilson et al., 2002), A 0535+26 (Finger et al., 1996b; Bildsten et al., 1997), 2S 1417-62 (Finger et al., 1996a; İnam et al., 2004), GRO J1744-28 (Bildsten et al., 1997), GRO J1750-27 (Scott et al., 1997), 2S 1845-024 (Finger et al., 1999), XTE J1543+568 (in't Zand et al., 2001), SAX J2103.5+4545 (Baykal et al., 2002, 2007) and XMMU J054134.7-682550 (Inam et al., 2009). As a result of our analysis, Swift J1626.6−5156 can be considered as an accretion powered pulsar that exhibit spin-up rate and X-ray flux correlation, which is apparent in Fig. 6.3.

The following equations, which are discussed in Section 2.6, enables us to estimate some physical properties of the source:

$$n(\omega_s) \simeq 1.4(1-\omega_s/\omega_c)/(1-\omega_s) \tag{2.44}$$

$$\omega_s = 1.2P^{-1}\dot{M}_{17}^{-3/7}\mu_{30}^{6/7}(M/M_\odot)^{-5/7} \tag{2.45}$$

$$\dot{\nu} = f_N(\mu, M)n(\omega_s)L^{6/7} = f_N(\mu, M)n(\omega_s)(4\pi d^2F)^{6/7} \tag{2.46}$$

The critical fastness parameter ω_c has been estimated as $\sim$ 0.35 (Ghosh and Lamb,

Table 6.2: X-ray Spectral Parameters of SWIFT J1626.6−5156 (errors indicate the 1σ confidence level)

Instrument	RXTE-PCA	RXTE-PCA	RXTE-PCA	Chandra-ACIS
Time Interval (MJD-MJD)	53724-53901	53901-54751	54751-55113	54897.31-54897.56
Exposure (ks)	227	175	47	20
n_H (10^{22}cm^{-2})	6.31(1.31)	1.21(76)	0.50 (fixed)	0.83(11)
Power Law Index	1.90(9)	2.00(5)	2.46(7)	0.94(12)
Power. Law Norm. (10^{-2}photons.keV^{-1}.cm^2.s^{-1} at 1keV)	37.4(8.6)	6.43(82)	1.00(10)	$6.93(2.26) \times 10^{-3}$
Iron Line Peak (keV)	6.32(39)	6.57(11)	6.57(9)	6.58 (fixed)
Iron Line Sigma (keV)	1.40(23)	0.76(12)	0 (fixed)	0 (fixed)
Iron Line Norm. (10^{-4}photons.cm^{-2}.s^{-1})	66.8(32.0)	7.41(2.41)	0.68(19)	$2.08(30) \times 10^{-2}$
Cut-off Energy (keV)	12.4(3)	15.4(5)	16.1 (fixed)	-
E-fold Energy (keV)	21.7(2.4)	10.1(2.1)	8.47 (fixed)	-
Energy Range(keV-keV)	3-20	3-20	3-20	0.3-8
Unabsorbed X-ray Flux (10^{-10}.ergs.s^{-1}.cm^{-2})	14.1(1)	1.97(2)	0.13(4)	$9.43(1.26) \times 10^{-3}$
Reduced χ^2 / d.o.f	1.42 / 32	1.47 / 32	0.61 / 36	1.25 / 34
Systematic Error	0.6%	0.6%	0.6%	-

1979b; Wang, 1987; Ghosh, 1994; Li and Wickramasinghe, 1998; Torkelsson, 1998; Dai and Li, 2006).

The case for the dimensionless torque ($n(\omega_s)$) to be unity arises when material torques dominate. When the magnetic torques cannot be neglected, the dimensionless torque should be calculated using (2.44). ”In Fig. 6.3, we present fits with $n = 1$ and the case for which the dimensionless torque is not unity (solid lines). We found that the model including non-unity dimensionless torque gives a better fit with a reduced χ^2 of 1.05 compared to the fit with the unity dimensionless torque giving a reduced χ^2 of 6.14.” (Icdem et al., 2011b).

The source distance can be estimated using (2.46) and Fig. 6.3 as $\simeq$ 15 kpc. This implies a surface magnetic field of $\simeq 9\times10^{11}$ G which is typical for accretion powered pulsars (see Coburn et al. (2002)). In fact, this magnetic field value is in accordance with the cyclotron lines around $\sim 10-20$ keV, which was previously suggested for the source (Coburn et al., 2006). Although this distance estimate is a bit large considering the extension of the Milky Way, galactic coordinates of the source (l=332.779925°, b=-2.002751°) suggest that the source is at the rim of the galaxy and this is exactly what the large distance indicates.

”From Fig. 6.2, it is shown that pulses from SWIFT J1626.6−5156 do not cease even after $\sim$ 1200 days from the outburst, which indicates that the source still accretes matter without any significant accretion geometry change.”(Icdem et al., 2011b).

The minimum n_{H} value obtained from the X-ray spectra of the source is about 10^{22} cm^{-2} (see Table 6.2 and Fig. 6.4). If this value is compared with the Galactic n_{H} estimates obtained from HI maps (Kalberla et al., 2005; Dickey and Lockman, 1990), it can be seen that similar values of n_{H} are expected from the location of the source.

Fig. 6.4 shows that power law index is anticorrelated with the X-ray flux. ”This indicates that the spectrum becomes softer with decreasing X-ray flux which is expected and may be interpreted as a consequence of mass accretion rate changes without a need of an accretion geometry change (Meszaros et al., 1983; Harding et al., 1984).” (Icdem et al., 2011b). 2S 1417-62 (İnam et al., 2004) and SAX J2103.5+4545 (Baykal et al., 2007) have been reported to display similar anticorrelations. In Fig. 6.4, it is also apparent that Hydrogen column density is in good correlation with the X-ray flux. A similar relation seen in 2S 1417-62 was interpreted as a result of the relationship between the matter concentration around the neutron star and the mass accretion rate in Be/X-ray pulsar systems (İnam et al., 2004).

CHAPTER 7

TIMING ANALYSIS of AXP 1E 2259+586

”The dataset used for the pulse timing of AXP 1E 2259+586 consists of *Rossi X-Ray Timing Explorer* (*RXTE*) proportional counter array (PCA) observations of the AXP 1E 2259+586 covering the time between March 2000 (MJD 51613) and October 2010 (MJD 55483). The PCA operates in the energy range 2–60 keV using an array of five collimated xenon/methane multi-anode proportional counter units (PCUs). The instrument has a total effective area of $\sim$ 6500 cm^2 and a field of view of $\sim 1^o$ FWHM (Jahoda et al., 1996).

A total of 479 observations were included in the pulse timing analysis presented in this thesis. The duration of observations vary from 10.6 ks to 0.2 ks, most of them are greater than 1 ks. During the analysed *RXTE*-PCA observations, the number of active PCUs varied between 1 and 4. Due to timing concerns,all the available layers of all PCUs were used in the analysis. ” (Icdem et al., 2011a)

7.1 Pulse Timing Analysis

For all xenon layers of the GoodXenonWithPropane or GoodXenon mode and event mode data, the selected energy range was 2–10 keV. After that the data obtained was binned with 125 ms time resolution and the solar system barycentre correction was applied to the resulting light curves. ”We used the standard analysis tools for *RXTE*-PCA data included in FTOOLS package to obtain the light curves and to merge them into a light curve covering all the interval mentioned above.” (Icdem et al., 2011a). The light curves were folded at frequencies given by Woods et al. (2004). Then, using the pulse frequency, which is the fundamental frequency in the power density spectrum, we applied a phase-folding technique in order to determine the precise pulse frequency evolution: ”The time series was split into intervals of approximately same duration, and each segment was folded with a quadratic ephemeris with the same frequency and frequency derivative,

$$\nu(t) = \nu_0 + \dot{\nu}(t - t_0) \implies \phi(t) = \phi_0(t_0) + \nu_0(t - t_0) + \dot{\nu}(t - t_0)^2 \tag{7.1}$$

so that we obtained a pulse profile for each time interval, which is made up of 20 phase bins. Then, we switched to the harmonic representation of pulse profiles as introduced by Boynton (1985)” (Icdem et al., 2011a)

$$\begin{aligned} f(\phi) &= F_0 + \sum_{k=1}^{10} \frac{F_k}{h_k} \cos k(\phi - \phi_k), \\ &= F_0 + \sum_{k=1}^{10} \left(\frac{A_k}{h_k} \cos k\phi + \frac{B_k}{h_k} \sin k\phi \right) \end{aligned} \tag{7.2}$$

where $A_k = F_k \cos k\phi_k$ and $B_k = F_k \sin k\phi_k$ are cosine and sine amplitudes, respectively, and h_k is the filter factor for the k-th harmonic, which is taken to be 1 in usual pulse-timing analysis (the reason why we include h_k in the equation is explained below). If a template pulse profile is extracted from a longer time interval in the quiescence period of the source and is represented by $g(\phi)$, then each harmonic of each folded pulse will have a relative phase with respect to the phase of the corresponding harmonic of the template pulse. Hence, it is more convenient to represent the pulses in the following way

$$g(\phi) = \sum_{k=1}^{10} \frac{G_k}{h_k} \cos k(\phi - \phi_k). \tag{7.3}$$

$$f(\phi) = \sum_{k=1}^{10} \frac{F_k}{h_k} \cos k(\phi - \phi_k + \Delta\phi_k) \tag{7.4}$$

Then, the maximum of the cross-correlation between the pulse profiles with the template pulse takes us to the pulse arrival times, $\Delta\phi$, in other words the value that maximizes the cross-correlation is the time of arrival:

$$C(\Delta\phi) = \int_0^{2\pi} f(\phi) g(\phi + \Delta\phi) d\phi. \tag{7.5}$$

Cross-correlation is repeated at numerous phase steps in a full cycle of the pulse period. At the end of this procedure, the phase maximizing the cross-correlation bring the template and the sample pulse very close, but there is usually still some phase difference between them and this problem is solved by using the Taylor expansion of the cross-correlation for small phase offsets and applying the resulting expression by iterations (Boynton, 1985):

$$\Delta\phi = \frac{\sum_{k=1}^{10} k \frac{G_k}{h_k}\frac{F_k}{h_k} \sin k\Delta\phi_k}{\sum_{k=1}^{10} k^2 \frac{G_k}{h_k}\frac{F_k}{h_k} \cos k\Delta\phi_k}. \tag{7.6}$$

The phase difference between the sample and master pulses is determined after this step. The whole procedure is applied to all the sample pulses in order to obtain the phase offset series.

As indicated above $h_k = 1$ in usual pulse-timing analysis. If one wants to do the analysis with filtered pulses, then h_k is put into action. ”Pulse filtering” method was proposed by Boynton (1985) in order to obtain minimum variance estimates in pulse phase. The method is based on the idea to attenuate the most noisy harmonics by multiplying them by a filter factor so that the filtered harmonics would have a white noise spectrum rather than the initial red noise spectrum. The optimal filter factor, determined empirically, is the reciprocal square root of the measured shape noise power spectrum:

$$h_k = \left(P_{k,\mathrm{phot}}/P_k\right)^{1/2}. \tag{7.7}$$

The measured noise power spectrum, P_k, can be calculated by the sum of squares of the difference between both the sine and cosine coefficients of the sample and master pulses over the whole pulse and by the normalization of this power with the total number of sample pulses as follows

$$P_k = \frac{1}{N}\sum_{j-1}^{N} N_j \left(\Delta A_{j,k}^2 + B_{j,k}^2\right) \tag{7.8}$$

where N_j is the number of individual pulses superposed in the jth sample pulse. Before calculating this difference the coefficients of the master pulse are multiplied by a scale factor in order to minimize the mean-square difference between the master and

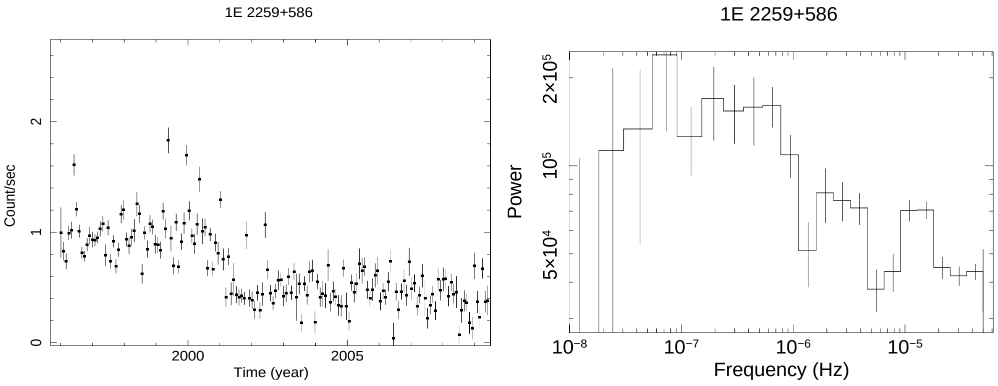

Figure 7.1: Long-term light curve and power density spectra of AXP 1E 2259+586

sample pulse (Deeter et al., 1987)

$$\Delta A_k = A_k - \alpha A'_k, \quad \Delta B_k = B_k - \alpha B'_k \tag{7.9}$$

$$\alpha = \frac{\sum\limits_{k=1}^{m} (A'_k A_k + B'_k B_k)}{\sum\limits_{k=1}^{m} (A'^2_k + B'^2_k)} \tag{7.10}$$

where m is the number of harmonics. The normalization factor in (7.7), $P_{k,\mathrm{phot}}$, is the constant power density from photon-counting (Poisson) noise and is determined as

$$P_{k,\mathrm{phot}} = \frac{2}{N} \sum_{j=1}^{N} N_j \sigma_j^2. \tag{7.11}$$

This method gives successful results, i.e. reduces the variance of the pulse phases significantly, if the excess pulse-shape noise spectrum is red enough.

7.2 Discussion

We appeal to pulse timing method for AXP 1E 2259+586 since its long term PDS does not give us satisfying information about the existence of an accretion disc surrounding the pulsar, i.e. its PDS cannot be modelled by a broken power model (see Fig. 7.1) and so we want to estimate the torque noise of the source in order to strengthen our prediction about the nature of the source.

The pulse profiles of the source AXP 1E 2259+586 were obtained by the procedure explained in the section 7.1. The pulses are generally powerful enough to carry out the timing analysis. A sample pulse is given in Fig. 7.2. The phase offset of a sample pulse from the template pulse, which was obtained from a longer time interval in which the source had been steady, after switching to the harmonic representation. A comparison between the real pulse and synthetic pulse reconstructed from the first ten harmonics can be seen in Fig. 7.3. As they are quite similar, representation of the pulses with ten harmonics is convenient to determine the phase offset series from the cross-correlation.

In figure 7.4 we present the phase offset vs time plot in three steps, obtained by using the procedure explained above. In this figure, the top panel is obtained by using the long-term spin-down trend, $\nu_0(t) = \nu_0 + \dot{\nu}_0(t - t_0)$, of the pulsar. As this plot explicitly shows there are two main instants after which the slope of the phase series changes. Just after these instants a modified pulse frequency should be introduced in order to flatten the phase offset series, $\nu_0 \rightarrow \nu_1 = \nu_0 + \dot{\nu}_0(t - t_0) + \Delta\nu_1$, and so we can determine the frequency shifts. The second panel is the phase offset evolution after the appropriate correction is applied for period after the first frequency shift. However, this operation is not sufficient to readjust the series following the second frequency shift. Hence, an additional correction was made after the second shift to obtain the third panel, $\nu_2 = \nu_1 + \Delta\nu_2$. Hence, the plot in the third panel contains three time intervals separated by two main frequency shifts, and the phase evolution of each interval was obtained using different ν_0s and t_0s. It should be emphasized that the spin down rate of the source was kept fixed at the value before the glitch in the estimation of pulse arrival times throughout the analysis, which is $\dot{\nu} = -9.920 \times 10^{-15}$ Hz.s^{-1}. An interesting thing here is that the first and the last correction revealed two other smaller frequency shifts around 53750 and 54880 MJD since the linear trend of the phase offsets is deformed after these instant. In the third panel, we also present the best-fitting models in the 5 distinct regions that are separated by the instant frequency shifts. The characteristics of the glitches may not be very similar; thus, we expect different best-fitting functions for the phase evolutions after the glitches. The residuals after the fits are given in the fourth panel at the bottom. The parameters calculated from those best-fitting models are presented in Tables 7.1 and 7.2. The long term spin evolution of 1E 2259+586 tells us that the AXP has undergone two big glitches and two frequency shifts in the time period mentioned above, i.e. its spin frequency has changed four times since then.

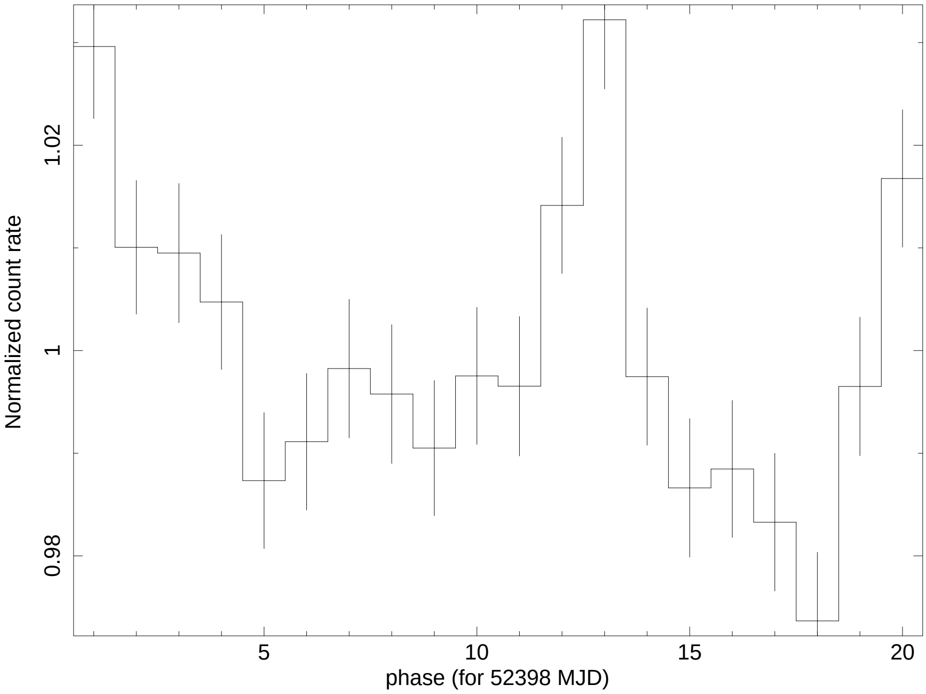

Figure 7.2: A sample pulse. The phase interval [0,1] is extended to [1,20]

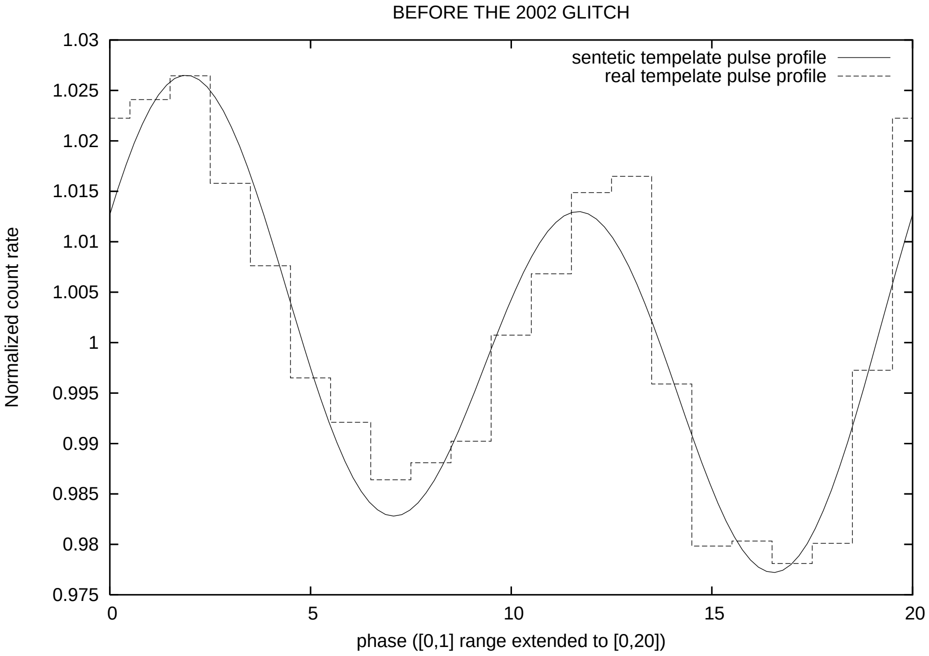

Figure 7.3: Real and synthetic pulse profiles

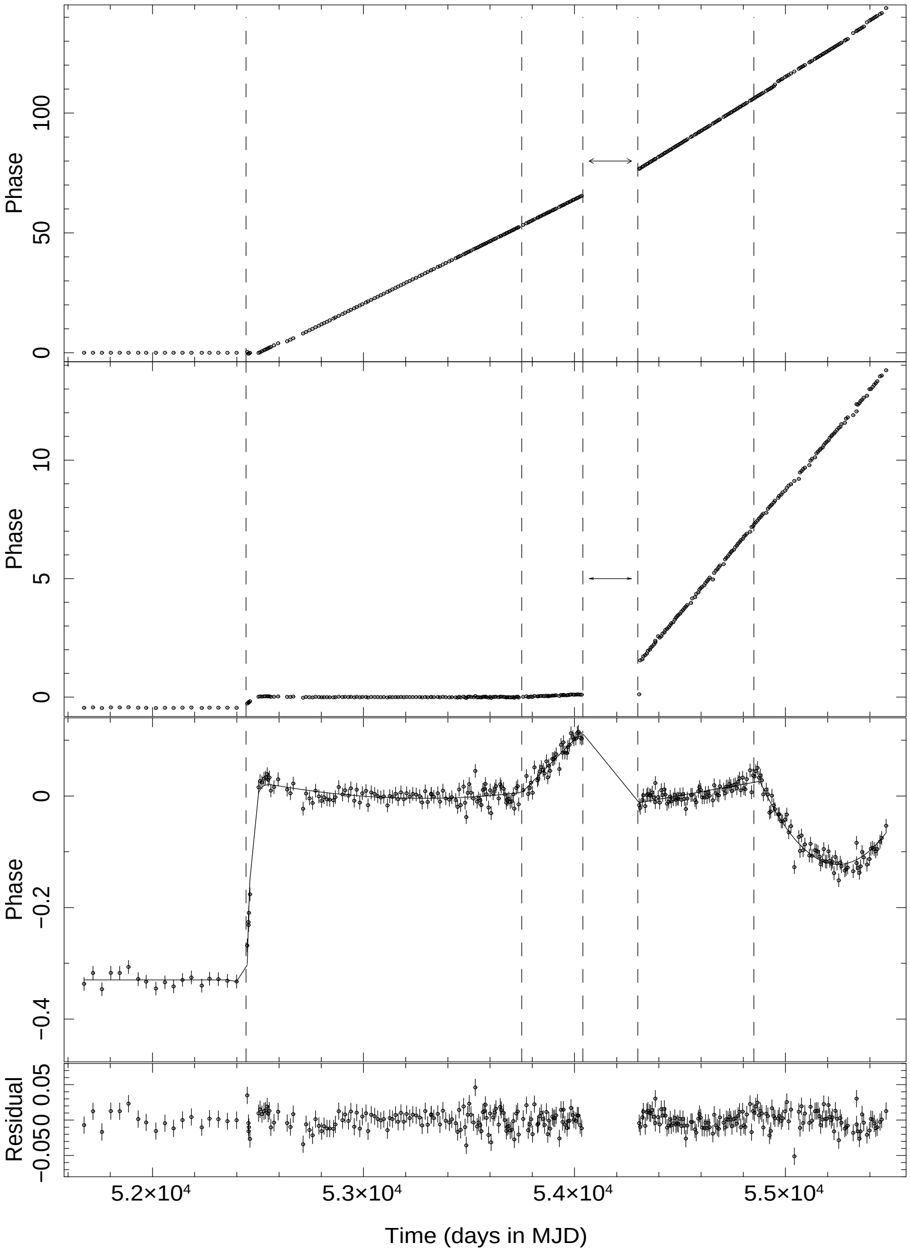

Figure 7.4: ”Phase offset series for AXP 1E 2259+586. Panels are described from top to bottom. *Top panel*: Phase offsets extracted using the spin-down model of the period before 2002-glitch. *Second panel*: Phase offsets using the correction of the pulse frequency after MJD 53443.13. *Third panel*: Arrival times obtained by an additional correction after MJD 54300. The solid curve is the phase offset evolution of the models presented in Tables 7.1 and 7.2. *Bottom panel*: Residuals, after subtracting the best-fitting models given in Tables 7.1 and 7.2. *All panels*: Glitch epochs are indicated with dashed vertical lines. The arrow shows the probable interval for the second glitch.” (Icdem et al., 2011a)

”

Table 7.1: Spin Parameters for 1E 2259+586 Before MJD 53750

Parameter	Value [1]	Value [2]
Spin frequency,ν (Hz)	0.14328703257(21)	0.14328703257(21)
Spin frequency derivative, $\dot{\nu}$ (Hz.s^{-1})	$-9.920(6) \times 10^{-15}$	$-9.920(6) \times 10^{-15}$
Epoch (MJD)	52400	52400
$\Delta\nu$ (Hz)	$5.25(12) \times 10^{-7}$	$6.70(1.14) \times 10^{-7}$
$\Delta\nu_g$ (Hz)	$> 8.7 \times 10^{-7}$	$8.29(78) \times 10^{-7}$
τ_g (days)	14.1(7)	14.1(1.2)
$\Delta\nu_d$ (Hz)	$\Delta\nu_g + (\sim 5 \times 10^{-9})$	$1.06(8) \times 10^{-6}$
τ_d (days)	15.9(6)	15.9(1.1)
$\Delta\dot{\nu}$ (Hz.s^{-1})	$2.18(25) \times 10^{-16}$	$1.268(3) \times 10^{-17}$
t_g (MJD)	52443.13(9)	52443.13(10)
rms timing residual (ms)	44.9	84.7
Start observing epoch (MJD)	51613	52390
End observing epoch (MJD)	52900	53750

Numbers in parentheses give 1σ uncertainties in the least significant digits quoted. [1] Taken from table 4 of Woods et al. (2004). [2] From our analysis. ”

The 2002 glitch of 1E 2259+586 cannot be modelled by the standard post-glitch relaxation models, which are composed of single or multiple exponential relaxation terms (Alpar et al., 984b). The best-fitting model is the one developed for two glitches of Crab pulsar (Lyne et al., 1993; Wong et al., 2001). ”In this model, the increase in the slowdown rate is interpreted as the cumulative of successive glitches; part of the increase is provided by a step and part is in the form of an exponential rise” (Icdem et al., 2011a)

$$\nu = \nu_0 + \dot{\nu}_0(t - t_0) + \Delta\nu + \Delta\nu_g(1 - e^{-(t-t_g)/\tau_g}) - \Delta\nu_d(1 - e^{-(t-t_g)/\tau_d}) + \Delta\dot{\nu}t, \qquad (7.12)$$

where the first two terms represent the frequency evolution before the glitch, t_g is the glitch epoch, $\Delta\nu$ is the frequency jump with the glitch, $\Delta\nu_g$ and $\Delta\nu_d$ are the growth

”

Table 7.2: Spin Parameters for 1E 2259+586 After MJD 53750

Parameter	Microglitch 1	Glitch 2	Microglitch 2
Spin frequency,ν, (Hz)	0.143286381(13)	0.143286138(14)	0.143285760(14)
Spin frequency derivative, $\dot{\nu}$ (Hz.s^{-1})	$-9.920(6) \times 10^{-15}$	$-9.920(6) \times 10^{-15}$	$-9.920(6) \times 10^{-15}$
Epoch (MJD)	53750	54040	54880
$\Delta\nu$ (Hz)	$4.42(46) \times 10^{-9}$	$> 1.6 \times 10^{-6}$	$-2.00(15) \times 10^{-9}$
$\Delta\dot{\nu}$ (Hz.s^{-1})	–	–	$2.91(22) \times 10^{-16}$
t_g (MJD)	$\sim$ 53750	$\sim$ 54040	$\sim$ 54880
rms timing residual (ms)	76.8	66.8	106.7
Start observing epoch (MJD)	53700	53900	54800
End observing epoch (MJD)	54040	54900	55570

Numbers in parentheses give 1σ uncertainties in the least significant digits quoted. ”

and decay amplitudes, respectively, τ_g and τ_d are the growth and decay time- scales. respectively, and $\Delta\dot{\nu}$ is the instantaneous jump in the spin down rate. The corresponding phase evolution equation, which is obtained by integrating the frequency evolution with respect to time, is used to fit the pulse arrival times in the period 52390–53750 MJD (the pulse frequency after the first glitch is corrected using the expression $\delta\nu = \Delta\nu + \Delta\nu_g - \Delta\nu_d$ in order to obtain a phase-connected time-of-arrival series).

The timing parameters of the first glitch for the time coverage from 52390 MJD to 53750 MJD are presented in Table 7.1 together with the those of Woods et al. (2004) which covers a smaller time interval after the glitch. ”Our analysis indicate that $\frac{\Delta\dot{\nu}}{\dot{\nu}}$ has shown a variation from -2.2×10^{-2} to $-1.278(3) \times 10^{-3}$, i.e. there is an order of magnitude reduction in the fraction in a $\sim$ 2.5-year time. It should be noted here that negative sign of the fractional change of derivative of pulse frequencies is quite unusual for large radio pulsar glitches, $\Delta\nu/\nu > 10^{-7}$ and $\Delta\dot{\nu}/\dot{\nu} \sim 10^{-2} - 10^{-3}$ (Alpar and Baykal, 1994, 2006).” (Icdem et al., 2011a)

The sparse sampling of observations between 54040 and 54300 MJD does not enable us to phase connect the pulse arrival times in this 260-day period. There are a total of 35 pulse arrival times in that interval. Hence, if there had been a glitch occurred in that interval, which appears to be the case in fact, the magnitude of that missed glitch could be estimated from cycle count ambiguity. ”Average sample rate of the observations during this time span is 260/35=7.4 days. If there is a missed cycle count, then it implies a frequency shift of $\Delta\nu \sim 1/(7.4 \times 86400) = 1.6 \times 10^{-6}$ which corresponds to unobserved glitch which fraction frequency shift of $\frac{\Delta\nu}{\nu} > 1.1 \times 10^{-5}$.” (Icdem et al., 2011a) This lower limit is close to the largest glitch that have been reported so far, which belongs to the young pulsar PSR B2334+61 and has magnitude $\Delta\nu/\nu \sim 2.05 \times 10^{-5}$ (Yuan et al., 2010).

The small frequency shifts observed at 53750 and 54880 MJD are at the order of microglitches detected in radio pulsars, having the ratios $\frac{\Delta\nu}{\nu} \sim \pm 10^{-8}$. The frequency shift of 53750 MJD did not cause a significant change in the spin down rate; on the other hand, the ratio $\frac{\Delta\dot{\nu}}{\dot{\nu}}$ is determined to be $-0.029(2)$ for the at 54880 MJD. It is interesting again to have a negative fractional change in the pulse frequency for an AXP; however, this is not unusual for the microglitches in radio pulsars. Chukwude and Urama (2010) states that there is no preference of microglitches regarding the sign of the fractional jumps $\Delta\nu/\nu$ and $\Delta\dot{\nu}/\dot{\nu}$. The timing parameters estimated for these small frequency shifts are given in Table 7.2. It should be noted here that this kind of frequency shifts have been observed in other SGRs and AXPs: two examples are SGR 1900+14 observed by Thompson et al. (2000) and AXP 4U 0142+61 observed by Gavriil et al. (2009).

We applied pulse-filtering technique, which is described in Section 7.1 to our pulses and noticed a very slight improvement in the results: in the time interval from 52700 to 53500 MJD, in which the TOAs show a linear trend, we were able to drop the variance from 0.789 to 0.779 after filtering the pulses. We decided that pulse-filtering is not an effective method for analysing our sample of pulses; hence, the findings we report in the rest of this paper were reached without using the pulse-filtering technique.

In Chapter 1, it is mentioned that AXPs have not display any evidence of binary companions. That is, a candidate accretion disc for AXPs most probably does not originate from mass transfer between two objects. Instead, it will be a fallback disc formed by the flow of material from a supernova remnant, as reviewed in Section 2.5. The low frequency power density spectrum of the AXP 1E 2259+586 does not fit to the broken power law model; i.e. no break frequency could be determined (see Fig. 5.4). However, this cannot be interpreted directly as absence of disc around the pulsar since the extension of the disc is probably much larger than those of discs in binary systems, instead some additional analysis methods should be applied to X-ray data of the source. Calculation of the torque noise strength after the pulse timing analysis would be a useful tool to decide whether the pulsar is accretion powered or not.

The effects of accreting material on the spin-down of a pulsar can be studied by examining the residuals of arrival times from a linear secular spin-down. There are different types of noise that can influence the arrival times of the pulses (Lamb et al., 1978), and the root mean square technique is just one of them that can characterize the random walk process (Cordes, 1980; Deeter, 1984; Cordes and Downs, 1985). For rth-order red noise, the scaling law between the noise strength and the root mean square of the residuals is given by

$$(2\pi)^2\langle\delta\phi^2\rangle = S\,T_{\mathrm{observation}}^{(2r-1)} \tag{7.13}$$

where $\langle\delta\phi^2\rangle$ is the normalized variance of the pulse arrival times (Deeter, 1984), r is the order of the red noise of the power density, S is the torque noise strength, and $T_{\mathrm{observation}}$ is the duration of the observation.

We have obtained the final phase offset series by removing second order polynomial from the pulse arrival times; hence, $r = 2$ in our case. Using the expression (7.13) for the time interval between 52500 and 53750 MJD for the AXP 1E 2259+586, the noise strength is calculated as $S \simeq (2\pi)^2(3.42\times10^{-3}/(1250\times86400)^3 \simeq 1.07\times10^{-25}$ rad^2.s^{-3}. This value is far lower than that smallest ever measured for an accreting X-ray pulsar, 4U 1626-67 ($S \sim 3.94\times10^{-21}$ rad^2.s^{-3}., (Chakrabarty et al., 1997))

CHAPTER 8

CONCLUSION

In his thesis, we try to find observational evidence for the standard theory of accretion disc physics, by analysing the power density spectra of 14 selected sources, six of them to be low mass X-ray binaries, seven of them to be high mass X-ray binaries, and an anomalous X-ray pulsar. We got the idea for our work from the 2005 paper of Gilfanov & Arefiev which handles the issue of viscous time scale of accretion discs of low mass X-ray binaries. We extended their work by examining different kinds of X-ray sources in order to understand the possible factors that affect accretion disc mechanism in these classes. The LMXBs we examined are six of Gilfanov & Arefiev's sources and the other sources we investigated were chosen according to the reasoning explained in Chapter 4.

We detected clear breaks in the power spectra of both low and high mass sources. In addition, these breaks appear to be correlated with the orbital frequency of the binaries linearly. Therefore, the most important thing we want to learn is the relationship between the obvious breaks in the power density spectra of these sources with the viscous time-scale, which should give us a clue about the size of the disc since viscosity is the main agent to drive the angular momentum loss that leads to the formation of a disc, of the corresponding accretion discs starting from the well known ”Standard Theory” of accretion discs by Shakura and Sunyaev (1973). Some inconsistencies between this model and the observations leads us to search for some other possible elements of the disc which may play important role in the dynamics of accretion discs.

The most significant propositions for the incompatibility between the theoretical calculations and the observational data are discussed in the previous sections. Among these the coronal flow above and below the disc appears to account for the results of the LMXBs to a great extent. On the other hand, the fact that we noticed similar breaks in HMXB spectra should not lead us to treat them in a similar fashion with the low mass X-ray binaries. There are two main probable mechanisms for accretion in HMXBs, which are discussed in the previous chapters in detail, and the nature of these mechanisms vary from source to source due to the fact that HMXBs can be quite dissimilar regarding their magnetic fields, eccentricities, etc.

Table 5.1 indicates that the value of $f_{\rm break}/f_{\rm orb}$ for LMXBs ranges in $\sim 0.14 - 0.37$, and that range is quite far from the interval predicted by the 'standard theory' given by ((5.16)), but they are all located around the curve corresponding for $H/R \sim 0.1$, as Fig. 5.6 shows. Gilfanov and Arefiev (2005) discuss a promising explanation for the difference between the analysis results and the standard theory regarding the ratio $f_{\rm break}/f_{\rm orb}$ which implies $\gtrsim 10$ shorter viscous time scales in the accretion discs: An additional coronal flow above the standard geometrically thin Shakura-Sunyaev disc so that the total disc thickness may reach up to $H/R \gtrsim 0.1$ as Figure 5.6 implies with average values. Fig. 5.6 demonstrates a separation of LMXBs into two groups . The group with higher $f_{\rm break}/f_{\rm orb}$ ratio mostly contains the small-q systems (i.e. compact binaries) analysed by Gilfanov and Arefiev (2005) and the other group is entirely composed of high-q systems which we work with in this thesis. There is an argument about this ”dichotomy”, as they called, in the $f_{\rm break}/f_{\rm orb}$ between wide and compact systems. Since, the viscous time in compact systems appear to be ~ 10 times shorter than that in the wide binaries, truncation of the disc due to tidal resonances comes forth. The most probable resonance excited in the disc is 3:1 Lindblad resonance in the small-q systems (Gilfanov and Arefiev, 2005).

The graph on the right in Figure 5.8 indicates that GRS 1915+105 should be among compact systems with its low $f_{\rm break}/f_{\rm orb}$ ratio. In fact, it is a microquasar having a small mass ratio, but it is a wide system with a long orbital period. Thus, its surprising result should be related to its large orbital separation. The effect of irradiation of accretion disc by central source is insufficient to expand the disc to its tidal radius and keeps it short around the circularization radius (Therefore, there is no need to talk about the resonances). Consequently, we get a smaller $f_{\rm break}/f_{\rm orb}$ ratio than expected from the system parameters.

In the case of HMXBs, we also distinguished two groups regrading their break frequencies. ”Those with lower normalized break frequencies, which are SS 433, OAO 1657-415, SMC X-1, and LMC X-1, are more likely to have Roche-lobe-overflow accretion discs” (Içdem and Baykal, 2011). On the contrary, Vela X-1, GX 301-2 and 4U 1700-377 have relatively high normalized break frequencies. The accretion process for these sources is the stellar-wind accretion which allows the formation of a smaller disc only. From these results of HMXBs, we deduce that the $f_{\mathrm{break}}/f_{\mathrm{orb}}$ ratios for HMXBs distinguishes Roche-lobe overflow binaries from stellar wind accretors. Hence, ”this method is especially useful for classifying black hole binaries according to their accretion mechanisms, since they cannot be shown on the Corbet diagram where the spin period of the compact object is compared with the orbital period of the system” (Içdem and Baykal, 2011).

Swift J1626.6-5156 show correlation between its spin-up rate and luminosity similar to that expected from accretion powered pulsars, as a result of its timing and spectral analysis presented in Chapter 6. Using this relation, the distance to the source is estimated to be $\simeq$ 15 kpc and the magnetic field of the pulsar is calculated as $\simeq 9\times10^{11}$ G. These values are in accordance with the previous spectral features, cyclotron line and n_{H} values, and the location of the source determined from its coordinates. In addition, the decrease of the power law index as with the increasing flux suggests that mass accretion rate changes without a need of a change in the geometry of accretion. The recent *Chandra* observation reveals the continuation of pulsing of the source, which is another sign of accretion of matter. All these results confirm that Swift J1626.6-5156 is an accretion-powered pulsar.

Our last X-ray source, AXP 1E 2259+586, does not reveal any breaks in its low frequency power density spectrum. Since this is not very promising to conclude that the pulsar does not have a disc, we applied to one another method to search for any evidences for the existence of a disc. From the pulse timing analysis, we calculated the torque noise to be around $S \simeq 1.07 \times 10^{-25}$ rad^2.s^{-3} which is very smaller than that expected in the presence of accretion. That is, AXP 1E 2259+586 does not show any evidence of a fallback disc around the pulsar in our analysis, but we need more to conclude that it does not possess an accretion disc.

Bibliography

(2011a). Observatories. Retrieved May 20, 2011, from `http://heasarc.gsfc.nasa.gov/docs/observatories.html`.

(2011b). X-ray astronomy satellites and missions. Retrieved May 20, 2011, from `http://imagine.gsfc.nasa.gov/docs/sats_n_data/xray_missions.html`.

Allen, C. W. (1973). *Astrophysical quantities*.

Alpar, M. A., Anderson, P. W., Pines, D., and Shaham, J. (1984b). Vortex creep and the internal temperature of neutron stars. II - VELA pulsar. *ApJ*, 278:791–805.

Alpar, M. A. and Baykal, A. (1994). Expectancy of Large Pulsar Glitches - a Comparison of Models with the Observed Glitch Sample. *MNRAS*, 269:849–+.

Alpar, M. A. and Baykal, A. (2006). Pulsar braking indices, glitches and energy dissipation in neutron stars. *MNRAS*, 372:489–496.

Anzer, U., Boerner, G., and Monaghan, J. J. (1987). Numerical studies of wind accretion. *A&A*, 176:235–244.

Araya, R. A. and Harding, A. K. (1999). Cyclotron Line Features from Near-critical Magnetic Fields: The Effect of Optical Depth and Plasma Geometry. *ApJ*, 517:334–354.

Araya-Góchez, R. A. and Harding, A. K. (2000). Cyclotron-Line Features from Near-critical Fields. II. On the Effect of Anisotropic Radiation Fields. *ApJ*, 544:1067–1080.

Arons, J. and Lea, S. M. (1976). Accretion onto magnetized neutron stars - Structure and interchange instability of a model magnetosphere. *ApJ*, 207:914–936.

Balbus, S. A. and Hawley, J. F. (1991). A powerful local shear instability in weakly magnetized disks. I - Linear analysis. II - Nonlinear evolution. *ApJ*, 376:214–233.

Balbus, S. A., Hawley, J. F., and Stone, J. M. (1996). Nonlinear Stability, Hydrodynamical Turbulence, and Transport in Disks. *ApJ*, 467:76–+.

Bandyopadhyay, R. M., Charles, P. A., Shahbaz, T., and Wagner, R. M. (2002). Infrared Photometric Variability of GX 13+1 and GX 17+2. *ApJ*, 570:793–798.

Bandyopadhyay, R. M., Shahbaz, T., Charles, P. A., and Naylor, T. (1999). Infrared spectroscopy of low-mass X-ray binaries - II. *MNRAS*, 306:417–426.

Baykal, A. (1997). The torque and X-ray flux changes of OAO 1657-415. *A&A*, 319:515–524.

Baykal, A. (2000). Short-term pulse frequency fluctuations of OAO 1657-415 from RXTE observations. *MNRAS*, 313:637–640.

Baykal, A., Göğüş, E., Çağdaş İnam, S., and Belloni, T. (2010). The Orbital Period of Swift J1626.6-5156. *ApJ*, 711:1306–1309.

Baykal, A., Inam, S. Ç., Stark, M. J., Heffner, C. M., Erkoca, A. E., and Swank, J. H. (2007). Timing studies on RXTE observations of SAX J2103.5+4545. *MNRAS*, 374:1108–1114.

Baykal, A., Stark, M. J., and Swank, J. H. (2002). X-Ray Spectra and Pulse Frequency Changes in SAX J2103.5+4545. *ApJ*, 569:903–910.

Baykal, A. and Swank, J. (1996). Pulse Frequency Changes of 1E 2259+586 and the Binary Interpretation. *ApJ*, 460:470–+.

Begelman, M. C., King, A. R., and Pringle, J. E. (2006). The nature of SS433 and the ultraluminous X-ray sources. *MNRAS*, 370:399–404.

Bernstein, R., Shectman, S. A., Gunnels, S. M., Mochnacki, S., and Athey, A. E. (2003). MIKE: A Double Echelle Spectrograph for the Magellan Telescopes at Las Campanas Observatory. In M. Iye & A. F. M. Moorwood, editor, *Society of Photo-Optical Instrumentation Engineers (SPIE) Conference Series*, volume 4841 of *Presented at the Society of Photo-Optical Instrumentation Engineers (SPIE) Conference*, pages 1694–1704.

Bildsten, L., Chakrabarty, D., Chiu, J., Finger, M. H., Koh, D. T., Nelson, R. W., Prince, T. A., Rubin, B. C., Scott, D. M., Stollberg, M., Vaughan, B. A., Wilson, C. A., and Wilson, R. B. (1997). Observations of Accreting Pulsars. *ApJS*, 113:367–+.

Blondin, J. M. (2000). Tidally-driven transport in accretion disks in close binary systems. *New A*, 5:53–68.

Blondin, J. M. and Pope, T. C. (2009). Revisiting the ”Flip-Flop” Instability of Hoyle-Lyttleton Accretion. *ApJ*, 700:95–102.

Boutloukos, S., van der Klis, M., Altamirano, D., Klein-Wolt, M., Wijnands, R., Jonker, P. G., and Fender, R. P. (2006). Discovery of Twin kHz QPOs in the Peculiar X-Ray Binary Circinus X-1. *ApJ*, 653:1435–1444.

Boynton, D.and Deeter, J. (1985). X-Ray Pulse Timing Studies, I&II. In F. Nagase & S. Hayakawa, editor, *Proceedings of the Inuyama workshop on timing analysis of X-ray sources*, Inuyama Workshop.

Boynton, P. E., Deeter, J. E., Lamb, F. K., Zylstra, G., Pravdo, S. H., White, N. E., Wood, K. S., and Yentis, D. J. (1984). New evidence on the nature of the neutron star and accretion flow in VELA X-1 from pulse timing observations. *ApJ*, 283:L53–L56.

Brown, G. E., Weingartner, J. C., and Wijers, R. A. M. J. (1996). On the Formation of Low-Mass Black Holes in Massive Binary Stars. *ApJ*, 463:297–+.

Brucato, R. J. and Kristian, J. (1972). Optical Candidates for Two X-Ray Sources. *ApJ*, 173:L105+.

Cannizzo, J. K., Lee, H. M., and Goodman, J. (1990). The disk accretion of a tidally disrupted star onto a massive black hole. *ApJ*, 351:38–46.

Castro-Tirado, A. J., Brandt, S., and Lund, N. (1992). GRS 1915+105. *IAU Circ*, 5590:2–+.

Catura, R. C. (1983). Evidence for X-ray scattering by interstellar dust. *ApJ*, 275:645–651.

Chakrabarty, D., Bildsten, L., Grunsfeld, J. M., Koh, D. T., Prince, T. A., Vaughan, B. A., Finger, M. H., Scott, D. M., and Wilson, R. B. (1997). Torque Reversal and Spin-down of the Accretion-powered Pulsar 4U 1626-67. *ApJ*, 474:414–+.

Chakrabarty, D., Grunsfeld, J. M., Prince, T. A., Bildsten, L., Finger, M. H., Wilson, R. B., Fishman, G. J., Meegan, C. A., and Paciesas, W. S. (1993). Discovery of the Orbit of the X-ray pulsar OAO 1657-415. *ApJ*, 403:L33–L37.

Chakrabarty, D., Wang, Z., Juett, A. M., Lee, J. C., and Roche, P. (2002). The X-Ray Position and Infrared Counterpart of the Eclipsing X-Ray Pulsar OAO 1657-415. *ApJ*, 573:789–793.

Chandrasekhar, S. (1960). The Stability of Non-Dissipative Couette Flow in Hydromagnetics. *Proceedings of the National Academy of Science*, 46:253–257.

Chandrasekhar, S. (1961). *Hydrodynamic and hydromagnetic stability*.

Chatterjee, P., Hernquist, L., and Narayan, R. (2000). An Accretion Model for Anomalous X-Ray Pulsars. *ApJ*, 534:373–379.

Cherepashchuk, A. (2002). Observational Manifestations of Precession of Accretion Disk in the SS 433 Binary System. *Space Sci. Rev.*, 102:23–35.

Cherepashchuk, A. M., Sunyaev, R. A., Fabrika, S. N., Postnov, K. A., Molkov, S. V., Barsukova, E. A., Antokhina, E. A., Irsmambetova, T. R., Panchenko, I. E., Seifina, E. V., Shakura, N. I., Timokhin, A. N., Bikmaev, I. F., Sakhibullin, N. A., Aslan, Z., Khamitov, I., Pramsky, A. G., Sholukhova, O., Gnedin, Y. N., Arkharov, A. A., and Larionov, V. M. (2005). INTEGRAL observations of SS433: Results of a coordinated campaign. *A&A*, 437:561–573.

Cherepashchuk, A. M., Sunyaev, R. A., Seifina, E. V., Panchenko, I. E., Molkov, S. V., and Postnov, K. A. (2003). INTEGRAL observations of SS433, a supercritically accreting microquasar with hard spectrum\thanks. *A&A*, 411:L441–L445.

Chodil, G., Mark, H., Rodrigues, R., Seward, F. D., and Swift, C. D. (1967). X-Ray Intensities and Spectra from Several Cosmic Sources. *ApJ*, 150:57–+.

Chukwude, A. E. and Urama, J. O. (2010). Observations of microglitches in Hartebeesthoek Radio Astronomy Observatory radio pulsars. *MNRAS*, 406:1907–1917.

Clark, J. S., Goodwin, S. P., Crowther, P. A., Kaper, L., Fairbairn, M., Langer, N., and Brocksopp, C. (2002). Physical parameters of the high-mass X-ray binary 4U1700-37. *A&A*, 392:909–920.

Coburn, W., Heindl, W. A., Rothschild, R. E., Gruber, D. E., Kreykenbohm, I., Wilms, J., Kretschmar, P., and Staubert, R. (2002). Magnetic Fields of Accreting X-Ray Pulsars with the Rossi X-Ray Timing Explorer. *ApJ*, 580:394–412.

Coburn, W., Heindl, W. A., Wilms, J., Gruber, D. E., Staubert, R., Rothschild, R. E., Postnov, K. A., Shakura, N., Risse, P., Kreykenbohm, I., and Pelling, M. R. (2000). The 1999 Hercules X-1 Anomalous Low State. *ApJ*, 543:351–358.

Coburn, W., Pottschmidt, K., Rothschild, R., Kretschmar, P., Kreykenbohm, I., Wilms, J., and McBride, V. (2006). Hard X-ray Spectroscopy Of Swift J1626.6-5156 With Rxte. In *AAS/High Energy Astrophysics Division #9*, volume 38 of *Bulletin of the American Astronomical Society*, pages 340–+.

Coe, M. J. (2000). Be stars in X-ray binary systems. In M. A. Smith, H. F. Henrichs, & J. Fabregat, editor, *IAU Colloq. 175: The Be Phenomenon in Early-Type Stars*, volume 214 of *Astronomical Society of the Pacific Conference Series*, pages 656–+.

Collins, G. W. and Scher, R. W. (2002). A revised dynamical model for SS433 and the nature of the system. *MNRAS*, 336:1011–1020.

Conti, P. S. (1978). Stellar parameters of five early type companions of X-ray sources. *A&A*, 63:225–235.

Cooke, B. A. and Ponman, T. J. (1991). A variable radio source in the error box of the bright galactic X-ray source GX 349 + 2. *A&A*, 244:358–362.

Corbet, R. H. D. (1984). Be/neutron star binaries - A relationship between orbital period and neutron star spin period. *A&A*, 141:91–93.

Cordes, J. M. (1980). Pulsar timing. II - Analysis of random walk timing noise - Application to the Crab pulsar. *ApJ*, 237:216–226.

Cordes, J. M. and Downs, G. S. (1985). JPL pulsar timing observations. III - Pulsar rotation fluctuations. *ApJS*, 59:343–382.

Cowley, A. P., Crampton, D., and Hutchings, J. B. (1979). The halo population X-ray source Cygnus X-2. *ApJ*, 231:539–550.

Cowley, A. P., Hutchings, J. B., and Crampton, D. (1978). Transmission grating spectroscopy of X-ray source fields. *AJ*, 83:1619–1621.

Crampton, D. and Cowley, A. P. (1980). Confirmation of a 9.8-day period of Cygnus X-2. *PASP*, 92:147–+.

Cui, W., Feng, Y. X., Zhang, S. N., Bautz, M. W., Garmire, G. P., and Schulz, N. S. (2002). A Chandra Spectroscopic Survey of Persistent Black Hole Candidates. *ApJ*, 576:357–365.

Dai, H.-L. and Li, X.-D. (2006). Accretion torque on magnetized neutron stars. *A&A*, 451:581–585.

Davidson, K. and Ostriker, J. P. (1973). Neutron-Star Accretion in a Stellar Wind: Model for a Pulsed X-Ray Source. *ApJ*, 179:585–598.

Decesar, M. E., Pottschmidt, K., and Wilms, J. (2009). Light curve oscillations and flux decline in the Be/X-ray binary Swift J1626.6-5156. *The Astronomer's Telegram*, 2036:1–+.

Deeter, J. E. (1984). Techniques for the estimation of red power spectra. II Evaluation of alternative methods. *ApJ*, 281:482–491.

Deeter, J. E., Boynton, P. E., Lamb, F. K., and Zylstra, G. (1989). VELA X-1 pulse timing. II - Variations in pulse frequency. *ApJ*, 336:376–393.

Deeter, J. E., Boynton, P. E., Shibazaki, N., Hayakawa, S., Nagase, F., and Sato, N. (1987). Pulse-timing study of VELA X-1 based on Hakucho and TENMA data - 1980-1984. *AJ*, 93:877–889.

den Hartog, P. R., Kuiper, L., Hermsen, W., and Vink, J. (2004). Detection of AXP 4U 0142+614 with INTEGRAL. *The Astronomer's Telegram*, 293:1–+.

Dhawan, V., Mirabel, I. F., and Rodríguez, L. F. (2000). AU-Scale Synchrotron Jets and Superluminal Ejecta in GRS 1915+105. *ApJ*, 543:373–385.

Dib, R., Kaspi, V. M., and Gavriil, F. P. (2008). Glitches in Anomalous X-Ray Pulsars. *ApJ*, 673:1044–1061.

Dickey, J. M. and Lockman, F. J. (1990). H I in the Galaxy. *ARA&A*, 28:215–261.

Ding, G. Q., Qu, J. L., and Li, T. P. (2003). Evolution of Hard X-Ray Spectra along the Branches in Circinus X-1. *ApJ*, 596:L219–L222.

Duncan, R. C. and Thompson, C. (1992). Formation of very strongly magnetized neutron stars - Implications for gamma-ray bursts. *ApJ*, 392:L9–L13.

Edelson, R. A. and Krolik, J. H. (1988). The discrete correlation function - A new method for analyzing unevenly sampled variability data. *ApJ*, 333:646–659.

Eggleton, P. P. (1983). Approximations to the radii of Roche lobes. *ApJ*, 268:368–+.

Eikenberry, S. S., Cameron, P. B., Fierce, B. W., Kull, D. M., Dror, D. H., Houck, J. R., and Margon, B. (2001). Twenty Years of Timing SS 433. *ApJ*, 561:1027–1033.

Ekşı, K. Y. and Alpar, M. A. (2003). Can Thin Disks Produce Anomalous X-Ray Pulsars? *ApJ*, 599:450–456.

Elsner, R. F. and Lamb, F. K. (1977). Accretion by magnetic neutron stars. I - Magnetospheric structure and stability. *ApJ*, 215:897–913.

Ertan, Ü. and Alpar, M. A. (2003). On the Enhanced X-Ray Emission from SGR 1900+14 after the August 27 Giant Flare. *ApJ*, 593:L93–L96.

Ertan, Ü., Göğüş, E., and Alpar, M. A. (2006). X-Ray and Infrared Enhancement of Anomalous X-Ray Pulsar 1E 2259+586. *ApJ*, 640:435–440.

Fabrika, S. (2004). The jets and supercritical accretion disk in SS433. *Astrophys. Sp. Phys. Rev.*, 12:1–152.

Fahlman, G. G. and Gregory, P. C. (1981). An X-ray pulsar in SNR G109.1-1.0. *Nature*, 293:202–204.

Fender, R. P., Gallo, E., and Jonker, P. G. (2003). Jet-dominated states: an alternative to advection across black hole event horizons in 'quiescent' X-ray binaries. *MNRAS*, 343:L99–L103.

Fender, R. P., Garrington, S. T., McKay, D. J., Muxlow, T. W. B., Pooley, G. G., Spencer, R. E., Stirling, A. M., and Waltman, E. B. (1999). MERLIN observations of relativistic ejections from GRS 1915+105. *MNRAS*, 304:865–876.

Finger, M. H., Bildsten, L., Chakrabarty, D., Prince, T. A., Scott, D. M., Wilson, C. A., Wilson, R. B., and Zhang, S. N. (1999). The Outbursts and Orbit of the Accreting Pulsar GS 1843-02=2S 1845-024. *ApJ*, 517:449–459.

Finger, M. H. and Prince, T. A. (1997). Recent results from observations of accreting pulsars. In C. D. Dermer, M. S. Strickman, & J. D. Kurfess, editor, *Proceedings of the Fourth Compton Symposium*, volume 410 of *American Institute of Physics Conference Series*, pages 57–74.

Finger, M. H., Wilson, R. B., and Chakrabarty, D. (1996a). Reappearance of the X-ray binary pulsar 2S 1417-624. *A&AS*, 120:C209+.

Finger, M. H., Wilson, R. B., and Harmon, B. A. (1996b). Quasi-periodic Oscillations during a Giant Outburst of A0535+262. *ApJ*, 459:288–+.

Fleischman, J. R. (1985). Detection of a new X-ray burst source. *A&A*, 153:106–108.

Frank, J., King, A., and Raine, D. J. (2002). *Accretion Power in Astrophysics: Third Edition*.

Galache, J. L., Corbet, R. H. D., Coe, M. J., Laycock, S., Schurch, M. P. E., Markwardt, C., Marshall, F. E., and Lochner, J. (2008). A Long Look at the Be/X-Ray Binaries of the Small Magellanic Cloud. *ApJS*, 177:189–215.

Garmire, G. P., Bautz, M. W., Ford, P. G., Nousek, J. A., and Ricker, Jr., G. R. (2003). Advanced CCD imaging spectrometer (ACIS) instrument on the Chandra X-ray Observatory. In J. E. Truemper & H. D. Tananbaum, editor, *Society of Photo-Optical Instrumentation Engineers (SPIE) Conference Series*, volume 4851 of *Presented at the Society of Photo-Optical Instrumentation Engineers (SPIE) Conference*, pages 28–44.

Gavriil, F. P., Dib, R., and Kaspi, V. M. (2009). The 2006-2007 Active Phase of Anomalous X-ray Pulsar 4U 0142+61: Radiative and Timing Changes, Bursts, and Burst Spectral Features. *ArXiv e-prints*.

Gavriil, F. P., Kaspi, V. M., and Woods, P. M. (2004). A Comprehensive Study of the X-Ray Bursts from the Magnetar Candidate 1E 2259+586. *ApJ*, 607:959–969.

Ghosh, P. (1994). Spin Evolution of Neutron Stars in Accretion Powered Pulsars. In S. Holt & C. S. Day, editor, *The Evolution of X-ray Binariese*, volume 308 of *American Institute of Physics Conference Series*, pages 439–+.

Ghosh, P. (2007). *Rotation and Accretion Powered Pulsars*. World Scientific Publishing Co.

Ghosh, P., Angelini, L., and White, N. E. (1997). The Nature of the “6 Second” and Related X-Ray Pulsars: Evolutionary and Dynamical Considerations. *ApJ*, 478:713–+.

Ghosh, P. and Lamb, F. K. (1979a). Accretion by rotating magnetic neutron stars. II - Radial and vertical structure of the transition zone in disk accretion. *ApJ*, 232:259–276.

Ghosh, P. and Lamb, F. K. (1979b). Accretion by rotating magnetic neutron stars. III - Accretion torques and period changes in pulsating X-ray sources. *ApJ*, 234:296–316.

Ghosh, P. and Lamb, F. K. (1991). Plasma physics of accreting neutron stars. In J. Ventura & D. Pines, editor, *NATO ASIC Proc. 344: Neutron Stars*, pages 363–+.

Ghosh, P., Pethick, C. J., and Lamb, F. K. (1977). Accretion by rotating magnetic neutron stars. I - Flow of matter inside the magnetosphere and its implications for spin-up and spin-down of the star. *ApJ*, 217:578–596.

Giacconi, R., Gursky, H., Paolini, F. R., and Rossi, B. B. (1962). Evidence for x Rays From Sources Outside the Solar System. *Physical Review Letters*, 9:439–443.

Gies, D. R., McSwain, M. V., Riddle, R. L., Wang, Z., Wiita, P. J., and Wingert, D. W. (2002). The Spectral Components of SS 433. *ApJ*, 566:1069–1083.

Gilfanov, M. and Arefiev, V. (2005). X-ray variability, viscous time scale and Lindblad resonances in LMXBs. *astro-ph/0501215*.

Glass, I. S. (1978). Variations of Circinus X-1 in the infrared. *MNRAS*, 183:335–340.

Glass, I. S. (1994). Longterm Infrared Behaviour of CIRCINUS-X-1. *MNRAS*, 268:742–+.

Gottlieb, E. W., Wright, E. L., and Liller, W. (1975). Optical studies of UHURU sources. XI. A probable period for Scorpius X-1 = V818 Scorpii. *ApJ*, 195:L33–L35.

Greiner, J., Cuby, J. G., McCaughrean, M. J., Castro-Tirado, A. J., and Mennickent, R. E. (2001). Identification of the donor in the X-ray binary GRS 1915+105. *A&A*, 373:L37–L40.

Greiner, J., Morgan, E. H., and Remillard, R. A. (1996). Rossi X-Ray Timing Explorer Observations of GRS 1915+105. *ApJl*, 473:L107+.

Haberl, F. and White, N. E. (1990). The X-ray absorption spectrum of VELA X-1. *ApJ*, 361:225–234.

Harding, A. K., Kirk, J. G., Galloway, D. J., and Meszaros, P. (1984). Self-consistent models for Coulomb-heated X-ray pulsar atmospheres. *ApJ*, 278:369–381.

Harlaftis, E. T. and Greiner, J. (2004). The rotational broadening and the mass of the donor star of GRS 1915+105. *A&A*, 414:L13–L16.

Haynes, R. F., Jauncey, D. L., Murdin, P. G., Goss, W. M., Longmore, A. J., Simons, L. W. J., Milne, D. K., and Skellern, D. J. (1978). Simultaneous radio and optical observations of Circinus X-1. *MNRAS*, 185:661–671.

Heyl, J. S. and Hernquist, L. (1997). The Thermal Evolution of Ultramagnetized Neutron Stars. *ApJ*, 491:L95+.

Hillwig, T. C., Gies, D. R., Huang, W., McSwain, M. V., Stark, M. A., van der Meer, A., and Kaper, L. (2004). Identification of the Mass Donor Star's Spectrum in SS 433. *ApJ*, 615:422–431.

Hiltner, W. A., Werner, J., and Osmer, P. (1972). Binary Nature of the B Supergiant in the Error Box of the VELA X-Ray Source. *ApJ*, 175:L19+.

Ho, C. (1988). Angular momentum transfer in non-axisymmetric accretion. *MNRAS*, 232:91–110.

Homan, J., van der Klis, M., Wijnands, R., Vaughan, B., and Kuulkers, E. (1998). Discovery of a 57-69 HZ Quasi-periodic Oscillation in GX 13+1. *ApJ*, 499:L41+.

Homan, J., Wijnands, R., Rupen, M. P., Fender, R., Hjellming, R. M., di Salvo, T., and van der Klis, M. (2004). Simultaneous radio and X-ray observations of the low-mass X-ray binary GX 13+1. *A&A*, 418:255–263.

Hong, J. and Hailey, C. J. (2004). Instability of the 13.8 Day Period in X-Ray Emission from 4U 1700-377. *ApJ*, 600:743–751.

Hutchings, J. B., Crampton, D., and Cowley, A. P. (1983). A spectrographic orbit for LMC X-1 - Another massive X-ray source? *ApJ*, 275:L43–L47.

Hutchings, J. B., Crampton, D., Cowley, A. P., Bianchi, L., and Thompson, I. B. (1987). Optical and UV spectroscopy of the black hole binary candidate LMC X-1. *AJ*, 94:340–344.

Iaria, R., Burderi, L., Di Salvo, T., La Barbera, A., and Robba, N. R. (2001). A Hard Tail in the X-Ray Broadband Spectrum of Circinus X-1 at the Periastron: A Peculiar Z Source. *ApJ*, 547:412–419.

Içdem, B. and Baykal, A. (2011). Viscous timescale in high mass X-ray binaries. *A&A*, 529:A7+.

Icdem, B., Baykal, A., and Cagdas Inam, S. (2011a). \emph{RXTE} Timing Analysis of the AXP 1E 2259+586. *astro-ph/11051630*.

Icdem, B., Inam, S. C., and Baykal, A. (2011b). Timing and X-ray Spectral Features of Swift J1626.6-5156. *astro-ph/11015168*.

Illarionov, A. F. and Sunyaev, R. A. (1975). Why the Number of Galactic X-ray Stars Is so Small? *A&A*, 39:185–+.

İnam, S. Ç., Baykal, A., Matthew Scott, D., Finger, M., and Swank, J. (2004). X-ray flux related timing and spectral features of 2S 1417-62. *MNRAS*, 349:173–180.

Inam, S. Ç., Townsend, L. J., McBride, V. A., Baykal, A., Coe, M. J., and Corbet, R. H. D. (2009). RXTE-PCA observations of XMMU J054134.7-682550. *MNRAS*, 395:1662–1668.

in’t Zand, J. J. M., Corbet, R. H. D., and Marshall, F. E. (2001). Discovery of a 75 Day Orbit in XTE J1543-568. *ApJ*, 553:L165–L168.

Iwasawa, K., Koyama, K., and Halpern, J. P. (1992). Pulse period history and cyclotron resonance feature of the X-ray pulsar 1E 2259+586. *PASJ*, 44:9–14.

Jahoda, K., Swank, J. H., Giles, A. B., Stark, M. J., Strohmayer, T., Zhang, W., and Morgan, E. H. (1996). In-orbit performance and calibration of the Rossi X-ray Timing Explorer (RXTE) Proportional Counter Array (PCA). In O. H. Siegmund & M. A. Gummin, editor, *Society of Photo-Optical Instrumentation Engineers (SPIE) Conference Series*, volume 2808 of *Society of Photo-Optical Instrumentation Engineers (SPIE) Conference Series*, pages 59–70.

Jimenez-Garate, M. A., Raymond, J. C., and Liedahl, D. A. (2002). The Structure and X-Ray Recombination Emission of a Centrally Illuminated Accretion Disk Atmosphere and Corona. *ApJ*, 581:1297–1327.

Johnston, H. M., Fender, R., and Wu, K. (1999). High-resolution optical and infrared spectroscopic observations of CIR X-1. *MNRAS*, 308:415–423.

Jones, C., Forman, W., Tananbaum, H., Schreier, E., Gursky, H., Kellogg, E., and Giacconi, R. (1973). Evidence for the Binary Nature of 2u 1700-37. *ApJ*, 181:L43+.

Jones, C., Giacconi, R., Forman, W., and Tananbaum, H. (1974). Observations of Circinus X-1 from UHURU. *ApJ*, 191:L71+.

Kahn, S. M. and Grindlay, J. E. (1984). Evidence for weak X-ray burst emission from Cygnus X-2 and GX 17 + 2. *ApJ*, 281:826–829.

Kalberla, P. M. W., Burton, W. B., Hartmann, D., Arnal, E. M., Bajaja, E., Morras, R., and Pöppel, W. G. L. (2005). The Leiden/Argentine/Bonn (LAB) Survey of Galactic HI. Final data release of the combined LDS and IAR surveys with improved stray-radiation corrections. *A&A*, 440:775–782.

Kaluzienski, L. J., Holt, S. S., Boldt, E. A., and Serlemitsos, P. J. (1976). Evidence for a 16.6 day period from Circinus X-1. *ApJ*, 208:L71–L75.

Kaper, L., van der Meer, A., and Najarro, F. (2006). VLT/UVES spectroscopy of

Wray 977, the hypergiant companion to the X-ray pulsar ¡ASTROBJ¿GX301-2¡/ASTROBJ¿. *A&A*, 457:595–610.

Kaplan, D. L., Chakrabarty, D., Wang, Z., and Wachter, S. (2009). A Mid-Infrared Counterpart to the Magnetar 1E 2259+586. *ApJ*, 700:149–154.

Kaspi, V. M., Gavriil, F. P., Woods, P. M., Jensen, J. B., Roberts, M. S. E., and Chakrabarty, D. (2003). A Major Soft Gamma Repeater-like Outburst and Rotation Glitch in the No-longer-so-anomalous X-Ray Pulsar 1E 2259+586. *ApJ*, 588:L93–L96.

Kaspi, V. M., Lackey, J. R., and Chakrabarty, D. (2000). A Glitch in an Anomalous X-Ray Pulsar. *ApJ*, 537:L31–L34.

Koh, D. T., Bildsten, L., Chakrabarty, D., Nelson, R. W., Prince, T. A., Vaughan, B. A., Finger, M. H., Wilson, R. B., and Rubin, B. C. (1997). Rapid Spin-up Episodes in the Wind-fed Accreting Pulsar GX 301-2. *ApJ*, 479:933–+.

Kuiper, L., Hermsen, W., and Mendez, M. (2004). Discovery of Hard Nonthermal Pulsed X-Ray Emission from the Anomalous X-Ray Pulsar 1E 1841-045. *ApJ*, 613:1173–1178.

Kumar, P., Narayan, R., and Loeb, A. (1995). On the Interaction of Convection and Rotation in Stars. *ApJ*, 453:480–+.

Kuulkers, E., van der Klis, M., and van Paradijs, J. (1995). Burstlike Events in the Z Source Cygnus X-2. *ApJ*, 450:748–+.

Kuulkers, E., van der Klis, M., and Vaughan, B. A. (1996). Secular variations in the Z source CygnusX-2. *A&A*, 311:197–210.

Kuulkers, E., Wijnands, R., and van der Klis, M. (1999). X-ray timing behaviour of Cygnus X-2 at low intensities. *MNRAS*, 308:485–492.

Lamb, F. K. (1989). Accretion by magnetic neutron stars. In H. Ögelman & E. P. J. van den Heuvel, editor, *Timing Neutron Stars*, pages 649–+.

Lamb, F. K., Pethick, C. J., and Pines, D. (1973). A Model for Compact X-Ray Sources: Accretion by Rotating Magnetic Stars. *ApJ*, 184:271–290.

Lamb, F. K., Shaham, J., and Pines, D. (1978). Period variations in pulsating X-ray sources. I - Accretion flow parameters and neutron star structure from timing observations. *ApJ*, 224:969–987.

Leahy, D. A. (1991). Modelling observed X-ray pulsar profiles. *MNRAS*, 251:203–212.

Leahy, D. A., Darbro, W., Elsner, R. F., Weisskopf, M. C., Kahn, S., Sutherland, P. G., and Grindlay, J. E. (1983). On searches for pulsed emission with application to four globular cluster X-ray sources - NGC 1851, 6441, 6624, and 6712. *ApJ*, 266:160–170.

Levine, A., Rappaport, S., Deeter, J. E., Boynton, P. E., and Nagase, F. (1993). Discovery of orbital decay in SMC X-1. *ApJ*, 410:328–341.

Levine, A. M. and Corbet, R. (2006). Detection of Additional Periodicities in RXTE ASM Light Curves. *ATEL*, 940:1–+.

Li, J. and Wickramasinghe, D. T. (1998). On spin-up/spin-down torque reversals in disc accreting pulsars. *MNRAS*, 300:1015–1022.

Lightman, A. P. and Eardley, D. M. (1974). Black Holes in Binary Systems: Instability of Disk Accretion. *ApJ*, 187:L1+.

Lipunov, V. M., Börner, G., and Wadhwa, R. S. (1992). *Astrophysics of Neutron Stars*.

Liu, Q. Z., van Paradijs, J., and van den Heuvel, E. P. J. (2005). High-mass X-ray binaries in the Magellanic Clouds. *A&A*, 442:1135–1138.

Liu, Q. Z., van Paradijs, J., and van den Heuvel, E. P. J. (2006). Catalogue of high-mass X-ray binaries in the Galaxy (4th edition). *A&A*, 455:1165–1168.

Liu, Q. Z., van Paradijs, J., and van den Heuvel, E. P. J. (2007). A catalogue of low-mass X-ray binaries in the Galaxy, LMC, and SMC (Fourth edition). *A&A*, 469:807–810.

Liutyi, V. M. and Siuniaev, R. A. (1976). Nature of the optical variability of the X-ray binary systems CYG X-2 - V1341 CYG and SCO X-1 - V818 SCO. *Sov. Astronomy Journal*, 53:511–526.

Lovelace, R. V. E., Romanova, M. M., and Bisnovatyi-Kogan, G. S. (1999). Magnetic Propeller Outflows. *ApJ*, 514:368–372.

Lucke, R., Yentis, D., Friedman, H., Fritz, G., and Shulman, S. (1976). Discovery of X-ray pulsations in SMC X-1. *ApJ*, 206:L25–L28.

Lyne, A. G., Pritchard, R. S., and Graham-Smith, F. (1993). Twenty-Three Years of Crab Pulsar Rotational History. *MNRAS*, 265:1003–+.

Lyubarskii, Y. E. (1997). Flicker noise in accretion discs. *MNRAS*, 292:679–+.

Makishima, K., Mihara, T., Nagase, F., and Tanaka, Y. (1999). Cyclotron Resonance Effects in Two Binary X-Ray Pulsars and the Evolution of Neutron Star Magnetic Fields. *ApJ*, 525:978–994.

Margon, B. (1984). Observations of SS 433. *ARA&A*, 22:507–536.

Margon, B., Lampton, M., Bowyer, S., and Cruddace, R. (1971). A Pulsing X-Ray Source in Circinus. *ApJ*, 169:L23+.

Mark, H., Price, R., Rodrigues, R., Seward, F. D., and Swift, C. D. (1969). Detection of X-Rays from the Large Magellanic Cloud. *ApJ*, 155:L143+.

Markwardt, C. B. and Swank, J. H. (2005). RXTE PCA observations of SWIFT J1626.6-5156. *The Astronomer's Telegram*, 679:1–+.

Mathis, J. S., Cohen, D., Finley, J. P., and Krautter, J. (1995). The X-Ray Halo of Nova V1974 Cygni (Nova Cygni 1992) and the Nature of Interstellar Dust. *ApJ*, 449:320–+.

Matsuba, E., Dotani, T., Mitsuda, K., Asai, K., Lewin, W. H. G., van Paradijs, J., and van der Klis, M. (1995). Discovery of X-Ray Bursts from GX 13+1 (4U 1811-17). *PASJ*, 47:575–580.

McClintock, J. E., Rappaport, S., Joss, P. C., Bradt, H., Buff, J., Clark, G. W., Hearn, D., Lewin, W. H. G., Matilsky, T., Mayer, W., and Primini, F. (1976). Discovery of a 283-second periodic variation in the X-ray source 3U 0900-40. *ApJ*, 206:L99–L102.

Mereghetti, S. and Stella, L. (1995). The very low mass X-ray binary pulsars: A new class of sources? *ApJ*, 442:L17–L20.

Meszaros, P. (1992). Book-Review - High-Energy Radiation from Magnetized Neutron Stars. *Science*, 257:1294–+.

Meszaros, P., Harding, A. K., Kirk, J. G., and Galloway, D. J. (1983). Accreting X-ray pulsar atmospheres heated by Coulomb deceleration of protons. *ApJ*, 266:L33–L37.

Meszaros, P. and Nagel, W. (1985a). X-ray pulsar models. I - Angle-dependent cyclotron line formation and comptonization. *ApJ*, 298:147–160.

Meszaros, P. and Nagel, W. (1985b). X-ray pulsar models. II - Comptonized spectra and pulse shapes. *ApJ*, 299:138–153.

Meurs, E. J. A. and van den Heuvel, E. P. J. (1989). The number of evolved early-type close binaries in the Galaxy. *A&A*, 226:88–107.

Meyer, F., Liu, B. F., and Meyer-Hofmeister, E. (2000). Evaporation: The change from accretion via a thin disk to a coronal flow. *A&A*, 361:175–188.

Meyer, F. and Meyer-Hofmeister, E. (1994). Accretion disk evaporation by a coronal siphon flow. *A&A*, 288:175–182.

Mirabel, I. F. and Rodríguez, L. F. (1994). A superluminal source in the Galaxy. *Nature*, 371:46–48.

Miyamoto, S., Kitamoto, S., Iga, S., Negoro, H., and Terada, K. (1992). Canonical time variations of X-rays from black hole candidates in the low-intensity state. *ApJ*, 391:L21–L24.

Moneti, A. (1992). Optical and infrared observations of Circinus X-1. *A&A*, 260:L7–L10.

Morrison, P. (1967). Extrasolar X-Ray Sources. *ARA&A*, 5:325–+.

Murdin, P., Jauncey, D. L., Lerche, I., Nicolson, G. D., Kaluzienski, L. J., Holt, S. S., and Haynes, R. F. (1980). Binary model of Circinus X-1. I - Eccentricity from combined X-ray and radio observations. *A&A*, 87:292–298.

Nagase, F. (1989). Accretion-powered X-ray pulsars. *PASJ*, 41:1–79.

Nagel, W. (1981). Radiative transfer in a strongly magnetized plasma. I - Effects of anisotropy. II - Effects of Comptonization. *ApJ*, 251:278–296.

Negueruela, I. (2007). Be/X-ray Binaries: An Observational Approach. In N. St.-Louis & A. F. J. Moffat, editor, *Massive Stars in Interactive Binaries*, volume 367 of *Astronomical Society of the Pacific Conference Series*, pages 477–+.

Negueruela, I. and Marco, A. (2006). Confirmation of counterpart to SWIFT J1626.6-5156. *The Astronomer's Telegram*, 739:1–+.

Nicolson, G. D., Glass, I. S., and Feast, M. W. (1980). Recent changes in the optical, infrared and radio emission from Circinus X-1. *MNRAS*, 191:293–299.

Oosterbroek, T., van der Klis, M., Kuulkers, E., van Paradijs, J., and Lewin, W. H. G. (1995). Circinus X-1 revisited: Fast-timing properties in relation to spectral state. *A&A*, 297:141–158.

Orosz, J. A. and Kuulkers, E. (1999). The optical light curves of Cygnus X-2 (V1341 Cyg) and the mass of its neutron star. *MNRAS*, 305:132–142.

Orosz, J. A., Steeghs, D., McClintock, J. E., Torres, M. A. P., Bochkov, I., Gou, L., Narayan, R., Blaschak, M., Levine, A. M., Remillard, R. A., Bailyn, C. D., Dwyer, M. M., and Buxton, M. (2009). A New Dynamical Model for the Black Hole Binary LMC X-1. *ApJ*, 697:573–591.

Paczynski, B. (1977). A model of accretion disks in close binaries. *ApJ*, 216:822–826.

Palmer, D., Barthelmy, S., Cummings, J., Gehrels, N., Kennea, J., Krimm, H., Markwardt, C. B., and Tueller, J. (2005). Swift-BAT discovery of a transient pulsar SWIFT J1626.6-5156. *The Astronomer's Telegram*, 678:1–+.

Papaloizou, J. (1979). On the stability of non-synchronous stars in close binary systems. *MNRAS*, 186:791–797.

Parkes, G. E., Culhane, J. L., Mason, K. O., and Murdin, P. G. (1980). A spectral study of Wray 977, the optical counterpart of the binary X-ray pulsar 4U 1223-62. *MNRAS*, 191:547–558.

Parmar, A. N., White, N. E., and Stella, L. (1989). The transient 42 second X-ray pulsar EXO 2030+375. II - The luminosity dependence of the pulse profile. *ApJ*, 338:373–380.

Plavec, M. and Kratochvil, P. (1964). Tables for the Roche model of close binaries. *Bulletin of the Astronomical Institutes of Czechoslovakia*, 15:165–+.

Polidan, R. S., Pollard, G. S. G., Sanford, P. W., and Locke, M. C. (1978). X-ray emission from the companion to V861Sco. *Nature*, 275:296–+.

Ponman, T. J., Cooke, B. A., and Stella, L. (1988). The quasi-periodic oscillations of GX349+2. *MNRAS*, 231:999–1009.

Pringle, J. E. (1996). Self-induced warping of accretion discs. *MNRAS*, 281:357–361.

Pringle, J. E. (1997). Self-induced warping of accretion discs - Non-linear evolution and application to AGN. *MNRAS*, 292:136–+.

Pringle, J. E. and Rees, M. J. (1972). Accretion Disc Models for Compact X-Ray Sources. *A&A*, 21:1–+.

Quaintrell, H., Norton, A. J., Ash, T. D. C., Roche, P., Willems, B., Bedding, T. R., Baldry, I. K., and Fender, R. P. (2003). The mass of the neutron star in Vela X-1 and tidally induced non-radial oscillations in GP Vel. *A&A*, 401:313–323.

Rappaport, S. and McClintock, J. (1975). 3U 0900-40. *IAUC*, 2833:2–+.

Reig, P., Belloni, T., Israel, G. L., Campana, S., Gehrels, N., and Homan, J. (2008). Bright flares from the X-ray pulsar SWIFT J1626.6-5156. *A&A*, 485:797–805.

Revnivtsev, M., Fabrika, S., Abolmasov, P., Postnov, K., Bikmaev, I., Burenin, R., Pavlinsky, M., Sunyaev, R., Khamitov, I., and Sakhibullin, N. (2006). Broad band variability of SS433: accretion disk at work? *A&A*, 447:545–551.

Revnivtsev, M. G., Sunyaev, R. A., Varshalovich, D. A., Zheleznyakov, V. V., Cherepashchuk, A. M., Lutovinov, A. A., Churazov, E. M., Grebenev, S. A., and Gilfanov, M. R. (2004). A Hard X-ray Survey of the Galactic-Center Region with the IBIS Telescope of the INTEGRAL Observatory: A Catalog of Sources. *Astronomy Letters*, 30:382–389.

Reynolds, A. P., Hilditch, R. W., Bell, S. A., and Hill, G. (1993). Optical spectroscopy of the massive X-ray binary SMC X-1/Sk 160. *MNRAS*, 261:337–345.

Roberts, M. S. E., Michelson, P. F., Leahy, D. A., Hall, T. A., Finley, J. P., Cominsky, L. R., and Srinivasan, R. (2001). Phase-dependent Spectral Variability in 4U 1907+09. *ApJ*, 555:967–977.

Ruhlen, L. and Smith, D. M. (2010). LMC X-1: Hybrid Black Hole Accretion? In *Bulletin of the American Astronomical Society*, volume 41 of *Bulletin of the American Astronomical Society*, pages 672–+.

Ryu, D. and Goodman, J. (1992). Convective instability in differentially rotating disks. *ApJ*, 388:438–450.

Sadakane, K., Hirata, R., Jugaku, J., Kondo, Y., Matsuoka, M., Tanaka, Y., and Hammerschlag-Hensberge, G. (1985). Ultraviolet spectroscopic observations of HD 77581(Vela X-1 = 4U 0900-40). *ApJ*, 288:284–291.

Samimi, J., Share, G. H., Wood, K., Yentis, D., Meekins, J., Evans, W. D., Shulman, S., Byram, E. T., Chubb, T. A., and Friedman, H. (1979). GX339-4 - A new black hole candidate. *Nature*, 278:434–436.

Sato, N., Nagase, F., Kawai, N., Kelley, R. L., Rappaport, S., and White, N. E. (1986). Orbital elements of the binary X-ray pulsar GX 301-2. *ApJ*, 304:241–248.

Schulz, N. S., Hasinger, G., and Truemper, J. (1989). Spectral classification of low-mass X-ray binary (LMXB) energy spectra with color-color diagrams. *A&A*, 225:48–68.

Scott, D. M., Finger, M. H., Wilson, R. B., Koh, D. T., Prince, T. A., Vaughan, B. A., and Chakrabarty, D. (1997). Discovery and Orbital Determination of the Transient X-Ray Pulsar GRO J1750-27. *ApJ*, 488:831–+.

Shakura, N. I. and Sunyaev, R. A. (1973). Black holes in binary systems. Observational appearance. *A&A*, 24:337–355.

Smale, A. P. (1998). A Type I Burst with Radius Expansion Observed from Cygnus X-2 with the Rossi X-Ray Timing Explorer. *ApJ*, 498:L141+.

Smale, A. P. and Lochner, J. C. (1992). Long-term variability in low-mass X-ray binaries - A study using data from VELA 5B. *ApJ*, 395:582–591.

Steeghs, D. and Casares, J. (2002). The Mass Donor of Scorpius X-1 Revealed. *ApJ*, 568:273–278.

Stewart, R. T., Caswell, J. L., Haynes, R. F., and Nelson, G. J. (1993). Circinus X-1 - A runaway binary with curved radio jets. *MNRAS*, 261:593–598.

Tennant, A. F., Fabian, A. C., and Shafer, R. A. (1986). The discovery of X-ray bursts from CIR X-1. *MNRAS*, 219:871–881.

Thompson, C. and Duncan, R. C. (1996). The Soft Gamma Repeaters as Very Strongly Magnetized Neutron Stars. II. Quiescent Neutrino, X-Ray, and Alfven Wave Emission. *ApJ*, 473:322–+.

Thompson, C., Duncan, R. C., Woods, P. M., Kouveliotou, C., Finger, M. H., and van Paradijs, J. (2000). Physical Mechanisms for the Variable Spin-down and Light Curve of SGR 1900+14. *ApJ*, 543:340–350.

Tian, W. W., Leahy, D. A., and Li, D. (2010). Distance to the SNR CTB109/AXP1E2259+586 by HI absorption and self-absorption. *MNRAS*, 404:L1–L5.

Torkelsson, U. (1998). Magnetic torques between accretion discs and stars. *MNRAS*, 298:L55–L59.

Trowbridge, S., Nowak, M. A., and Wilms, J. (2007). Tracking the Orbital and Superorbital Periods of SMC X-1. *ApJ*, 670:624–634.

Tudose, V., Fender, R. P., Kaiser, C. R., Tzioumis, A. K., van der Klis, M., and Spencer, R. E. (2006). The large-scale jet-powered radio nebula of Circinus X-1. *MNRAS*, 372:417–424.

Ueda, Y., Asai, K., Yamaoka, K., Dotani, T., and Inoue, H. (2001). Discovery of an Iron K Absorption Line in the Low-Mass X-Ray Binary GX 13+1. *ApJ*, 556:L87–L90.

Ulmer, M. P., Baity, W. A., Wheaton, W. A., and Peterson, L. E. (1972). Observations of the VELA XR-1 by the UCSD X-Ray Telescope on OSO-7. *ApJ*, 178:L121+.

van der Klis, M., Swank, J. H., Zhang, W., Jahoda, K., Morgan, E. H., Lewin, W. H. G., Vaughan, B., and van Paradijs, J. (1996). Discovery of Submillisecond Quasi-periodic Oscillations in the X-Ray Flux of Scorpius X-1. *ApJ*, 469:L1+.

van der Klis, M., Wijnands, R. A. D., Horne, K., and Chen, W. (1997). Kilohertz Quasi-Periodic Oscillation Peak Separation Is Not Constant in Scorpius X-1. *ApJ*, 481:L97+.

van der Meer, A., Kaper, L., van Kerkwijk, M. H., Heemskerk, M. H. M., and van den Heuvel, E. P. J. (2007). Determination of the mass of the neutron star in SMC X-1, LMC X-4, and Cen X-3 with VLT/UVES. *A&A*, 473:523–538.

van Paradijs, J., Taam, R. E., and van den Heuvel, E. P. J. (1995). On the nature of the 'anomalous' 6-s X-ray pulsars. *A&A*, 299:L41+.

Vrtilek, S. D., McClintock, J. E., Seward, F. D., Kahn, S. M., and Wargelin, B. J. (1991). The Einstein objective grating spectrometer survey of galactic binary X-ray sources. *ApJS*, 76:1127–1167.

Wachter, S. and Margon, B. (1996). Photometry of GX 349+2: Evidence for a 22-Hour Period. *AJ*, 112:2684–+.

Wang, J. C. L. (1997). Evidence for Magnetic Field Decay in RX J0720.4-3125. *ApJ*, 486:L119+.

Wang, Y.-M. (1981). Spin-reversed accretion as the cause of intermittent spindown in slow X-ray pulsars. *A&A*, 102:36–44.

Wang, Y.-M. (1987). Disc accretion by magnetized neutron stars - A reassessment of the torque. *A&A*, 183:257–264.

Wang, Y.-M. and Welter, G. L. (1981). An analysis of the pulse profiles of the binary X-ray pulsars. *A&A*, 102:97–108.

Watson, M. G., Warwick, R. S., and Corbet, R. H. D. (1982). The orbital period of 2S 1223-624 /GX301-2/. *MNRAS*, 199:915–924.

Whelan, J. A. J., Mayo, S. K., Wickramasinghe, D. T., Murdin, P. G., Peterson, B. A., Hawarden, T. G., Longmore, A. J., Haynes, R. F., Goss, W. M., Simons, L. W., Caswell, J. L., Little, A. G., and McAdam, W. B. (1977). The optical and radio counterpart of Circinus X-1 /3U 1516-56/. *MNRAS*, 181:259–271.

White, N. E., Mason, K. O., Huckle, H. E., Charles, P. A., and Sanford, P. W. (1976). Periodic modulation of three galactic X-ray sources. *ApJ*, 209:L119–L124.

White, N. E. and Pravdo, S. H. (1979). The discovery of 38.22 second X-ray pulsations from the vicinity of OAO 1653-40. *ApJ*, 233:L121–L124.

White, N. E., Swank, J. H., and Holt, S. S. (1983). Accretion powered X-ray pulsars. *ApJ*, 270:711–734.

Whitehurst, R. and King, A. (1991). Superhumps, resonances and accretion discs. *MNRAS*, 249:25–35.

Wijnands, R., Homan, J., van der Klis, M., Kuulkers, E., van Paradijs, J., Lewin, W. H. G., Lamb, F. K., Psaltis, D., and Vaughan, B. (1998). Discovery of kHz Quasi-periodic Oscillations in the Z Source Cygnus X-2. *ApJ*, 493:L87+.

Wijnands, R. A. D., Kuulkers, E., and Smale, A. P. (1996). Detection of a approximately 78 day Period in the RXTE, VELA 5B, and Ariel 5 All-Sky Monitor Data of Cygnus X-2. *ApJ*, 473:L45+.

Wijnands, R. A. D., van der Klis, M., Kuulkers, E., Asai, K., and Hasinger, G. (1997). GINGA observations of Cygnus X-2. *A&A*, 323:399–414.

Wilms, J., Nowak, M. A., Dove, J. B., Fender, R. P., and Di Matteo, T. (1999). Low-Luminosity States of the Black Hole Candidate GX 339-4. I. ASCA and Simultaneous Radio/RXTE Observations. *ApJ*, 522:460–475.

Wilson, C. A., Finger, M. H., Coe, M. J., Laycock, S., and Fabregat, J. (2002). A Decade in the Life of EXO 2030+375: A Multiwavelength Study of an Accreting X-Ray Pulsar. *ApJ*, 570:287–302.

Witt, A. N., Smith, R. K., and Dwek, E. (2001). X-Ray Halos and Large Grains in the Diffuse Interstellar Medium. *ApJ*, 550:L201–L205.

Wojdowski, P., Clark, G. W., Levine, A. M., Woo, J. W., and Zhang, S. N. (1998). Quasi-periodic Occultation by a Precessing Accretion Disk and Other Variabilities of SMC X-1. *ApJ*, 502:253–+.

Wong, T., Backer, D. C., and Lyne, A. G. (2001). Observations of a Series of Six Recent Glitches in the Crab Pulsar. *ApJ*, 548:447–459.

Woods, P. M., Kaspi, V. M., Thompson, C., Gavriil, F. P., Marshall, H. L., Chakrabarty, D., Flanagan, K., Heyl, J., and Hernquist, L. (2004). Changes in the X-Ray Emission from the Magnetar Candidate 1E 2259+586 during Its 2002 Outburst. *ApJ*, 605:378–399.

Yuan, J. P., Manchester, R. N., Wang, N., Zhou, X., Liu, Z. Y., and Gao, Z. F. (2010). A Very Large Glitch in PSR B2334+61. *ApJL*, 719:L111–L115.

Zhang, F., Li, X.-D., and Wang, Z.-R. (2004). Where Are the Be/Black Hole Binaries? *ApJ*, 603:663–668.

Zhang, W., Strohmayer, T. E., and Swank, J. H. (1998). Discovery of Two Simultaneous Kilohertz QPOs in the Persistent Flux of GX3 49+2. *ApJ*, 500:L167+.

Zuiderwijk, E. J., van den Heuvel, E. P. J., and Hensberge, G. (1974). Orbit, spectrum and H alpha variations of HD 77581 /3 U 0900-40/. *A&A*, 35:353–360.